UNIVERSITY OF CALIFORNIA

Los Angeles

Characterization Studies of Materials and Devices used for Electrochemical Energy Storage

A dissertation submitted in partial satisfaction of the requirements for the degree

Doctor of Philosophy in Materials Science and Engineering

by

Daniel Eduardo Membreno

2014

ABSTRACT OF THE DISSERTATION

Characterization Studies of Materials and Devices used

for Electrochemical Energy Storage

by

Daniel Eduardo Membreno

Doctor of Philosophy in Materials Science and Engineering

University of California, Los Angeles, 2014

Professor Bruce Dunn, Chair

There is a variety of energy storage systems but they all share a need for characterization. The principal motivation of this work is to understand the parameters that affect charge storage in three different systems. Studies were performed on carbon nanotube supercapacitors whose electrolyte was based on an encapsulated 1-butyl-3-methylimidazolium tetrafluoroborate ionic liquid. This electrochemical double layer capacitor is an intrinsically high power device and the challenge was preserving that power with a quasi-solid electrolyte. The device was characterized by a suite of electrochemistry techniques and demonstrated both high power and high energy densities.

The second system investigated is the electrochemical pseudocapacitor orthorhombic Nb_2O_5, a transition metal oxide system with high rate capability. Pseudocapacitors are based on faradaic reactions that allow them high energy densities than traditional electrochemical capacitors. Nb_2O_5 has a high rate capability through its combination of electronic and ionic

conductivities. This study quantified those values as a function of lithiation and shed light on a phase change when heating lithiated samples.

Batteries have greater energy densities than electrochemical capacitors but they have a lower power density due to slow ion kinetics through the electrodes. An approach to minimize the diffusion distance in the electrodes is to design the entire battery into an interpenetrating array. This structure needs a thin conformal solid electrolyte to prevent electrical shorts and maximize energy density. Due to the 3D nature of this structure, common techniques for imaging pinholes do not have the spatial resolution to characterize the film. A technique was adapted from the literature to characterize the pinholes using electron transfer from a metallocene molecule to the surface of the electrode. This technique offers a spatial sensitivity of a few angstroms in which to detect pinholes and can be used to characterize 3D conformal films.

The dissertation of Daniel Eduardo Membreno is approved.

Sarah Tolbert

Chi On Chui

Bruce Dunn, Committee Chair

University of California, Los Angeles

2014

To Alyssa

Table of Contents

LIST OF FIGURES

LIST OF TABLES

ACKNOWLEDGEMENTS

I am thankful for the support of Dunn lab. I have received much guidance along with advice that I will always cherish. I am grateful for the opportunity to work with each member of the lab. I would like to thank Leland and Jimmy for their help with the characterization work. Special thank you to Jon for running almost every scan in chapter 4. Without all of your support I would not be where I am today. Thank you to Dr. Dunn for providing the platform from which we can all improve our skills. Thank you.

I appreciate the support from the FENA Focus Center, one of six research centers funded under the Focus Center Research Program (FCRP), a Semiconductor Research Corporation entity. I also acknowledge the support from the NSF IGERT Materials Creation Training Program; DGE-0654431 as well as support by the Office of Naval Research. A special thank you to Raytheon Vision Systems for hosting me in my NSF sponsored internship.

Thank you to Springer Journal of Sol-gel Science and Technology for allowing the inclusion of our submitted material.

Thank you to the American Chemical Society for allowing a reprint of their figure.

VITA

2009	B.S. Applied Physics, concentration in Materials Science Cum Laude. University of California, Davis
2011	M.S. Materials Science and Engineering University of California, Los Angeles
2009-2013	Graduate Student Researcher Department of Materials Science and Engineering University of California, Los Angeles

Publications and Patents

I.E. Rauda, L.C. Saldarriaga-Lopez, B.A Helms, L.T. Schelhas, D. Membreno, D.J. Milliron, and S.H. Tolbert, Advanced Materials, 25 (2013) 1315–22.

D. Membreno, L. Smith, B. Dunn, "Sol-Gel Chemistry: Creating Materials and Architecture for Energy Generation and Storage" Sol-Gel Science and Technology. Under review (2013)

J. Cho, Y.C. Perng, D. Membreno, N. Cirigliano, B. Dunn, M.F. Toney, J.P. Chang, "Synthesis of ion conducting $Li_xAl_ySi_zO$ thin films by atomic layer deposition" Submitted (2013)

D. Membreno, L. Smith, C. Chui, B. Dunn, “High Energy and Power Carbon Nanotube Quasi-Solid Supercapacitor Made by Sol-Gel Encapsulation of 1-Butyl-3-Methylimidazolium Tetrafluoroborate” In preparation (2013)

N. Cirigliano, G. Sun, D. Membreno, P. Malati, C.J. Kim, B.Dunn, “3D Architectured Anodes for Large Areal Capacity Microbatteries” In preparation (2013)

B. Dunn, C. Chui, A. Jacob, D. Membreno, L. Smith, 61/485,264. Solid-State Supercapacitor, patent pending. (2011)

Chapter 1. Introduction and Objectives

Energy storage is becoming the design limitation for high power mobile electronics. Batteries have been the energy storage of choice for portable electronics because of their large energy densities and moderate power performance [1]. As devices become smaller, the power demands are increasing and the need for durable, efficient and cheap to manufacture energy storage is becoming a necessity [2]. Alternatively, electrochemical capacitors have shown promise in enabling high power energy storage using a variety of systems including metal oxides [3], carbon nanotubes [4], onion like carbon [5] and graphene [6].

This dissertation details the characterization of three different energy storage systems. The first system presented involves the synthesis and characterization of the quasi-solid electrolyte made by encapsulating the ionic liquid 1-butyl-3-methylimidazolium tetrafluoroborate into a silica matrix using the sol gel process. Quasi-solid electrolytes compatible with electrochemistry are advantageous for miniaturizing devices. A full supercapacitor with carbon nanotube electrodes deposited by electrophoretic deposition and the quasi-solid electrolyte were used to study the effect of the encapsulation on the rate capability and energy storage.

The second system to characterize is the transition metal oxide Nb_2O_5, a lithium pseudocapacitor with a high rate capability. The interest in pseudocapacitors stems from their high power but the quantification of their properties is challenging since electronic conductivity varies with the state of lithiation. To characterize the conductivity, dense films of crystalline orthorhombic Nb_2O_5 were made by spin coating and then annealing in air. The conductivity as a

function of lithiation and temperature were measured by in-situ impedance in combination with galvanostatic cycling.

The third system involves characterizing conformal solid electrolytes for three-dimensional (3D) microbatteries. 3D microbatteries have very high power because they minimize the diffusion distance of ions by distributing the electrode mass to bring the electrodes closer together. These architectures depend on pinhole free conformal coatings to prevent electrical shorts. The characterization used here to test for pinholes was an electrochemical process based on the oxidation and reduction of metallocenes. The following solid electrolyte films deposited from the gas phase were tested: lithium aluminosilicate was prepared by atomic layer deposition (ALD) while 1,3,5,7- Tetravinyltetramethylcyclotetrasiloxane and poly(trivinyltrimethylcyclotrisiloxane) were prepared by initiated chemical vapor deposition (iCVD). The ionic conductivity of the solid electrolytes was characterized by hanging mercury drop impedance.

Chapter 2. Carbon Nanotube Supercapacitor with Sol-Gel Encapsulated1-Butyl-3-Methylimidazolium Tetrafluoroborate electrolyte

Chapter 2.1. Introduction

Electrochemical capacitors share the same device configuration as batteries with both having two electrodes immersed in an electrolyte. But the devices differ in the mechanism and speed of their energy storage. Electrochemical capacitors store charge on the surface of their electrodes in what is known as the electrochemical double layer [7]. The electrolyte ions, under an applied electric field, move in the electrolyte to form layers of opposite charge with both charged electrodes, which results in two series capacitors with atomic level separation [8]. Batteries store energy by bulk chemical reactions, which are slower than electrochemical capacitors, due to ion diffusion through the electrolyte and then through the bulk of the electrode.

Even though supercapacitors have higher power than thin film batteries, it is advantageous to minimize the device structure to micron dimensions in what is known as a micro supercapacitor. Micro supercapacitors minimize the inactive electrolyte volume, which improves the power of the device and maximizes the energy storage as shown in figure 2.1. As the spacing between the electrodes in figure 2.1 decreases, there is more difficulty in preventing electrical shorts. Another difficulty with this design is that variations in the thickness of the electrode will limit the energy storage.

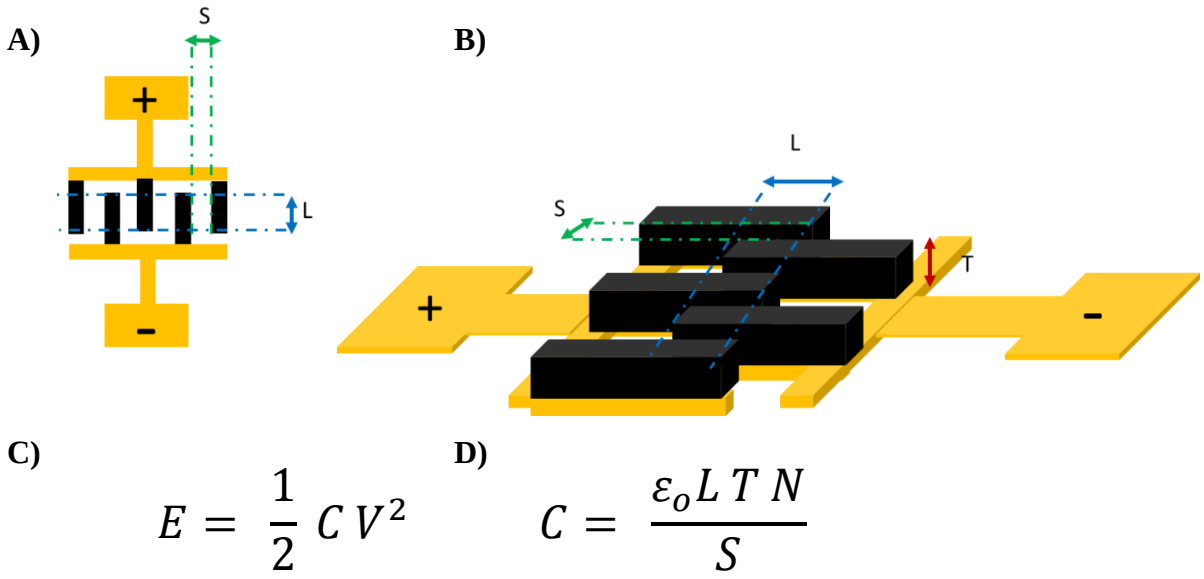

Figure 2.1 Schematic of micro supercapacitor A) top down view B) side profile along. C) Equation for the energy storage E from a capacitor with capacitance C and voltage V. D) Equation for capacitance of a micro supercapacitor with permittivity of free space ε_o, electrode active length L, electrode thickness T, electrode spacing S and number of electrode spacing's S for the device N (4 for this device)

Previous studies have demonstrated various methods for fabricating micro supercapacitor devices including micro contact printing [9], laser scribing [6], and electrophoretic deposition [5] (EPD). For these three studies, standard photolithography was used to fabricate the gold current collectors shown schematically in figure 2.1. In micro contact printing, a slurry of carbon black and polymer binder is physically deposited onto the gold electrodes in a raster process. Rastering is a slow process and this approach has an additional disadvantage that when the spacing between electrodes is decreased there is more danger of the wet slurry coalescing to short the electrodes. An alternative raster process is laser scribing, where graphene oxide is spin coated over the device area and then heat from a laser selectively transforms graphene oxide into graphene. The advantage of this approach is the spatial control of where the electronically insulating graphene oxide transforms into the electronically conductive graphene. The downside

of this approach is controlling the electrode thickness. Thick electrodes require more heat than thin electrodes so increasing the laser dwell time is needed to fully convert a thick electrode. The disadvantage of increased dwell time is that graphene is a good thermal conductor so longer laser dwell time will convert the graphene isotropically and limit the spatial resolution of the electrodes.

EPD is of interest because it can be used to selectively deposit carbon nanotubes (CNT) onto charged conducting surfaces without requiring a binder or rastering. Binderless depositions are ideal for improving both energy and power densities since binders are inactive for energy storage and they disrupt electrical contact between the more conductive materials in the electrode. EPD apparatus is simple to construct; two electrodes are placed in a stable suspension and the active material deposits electrostatically onto the surface of the deposition electrode when voltage is applied. EPD fabrication can also be scaled to industrial dimensions and throughputs [10].

The ideal electrode for a high energy and high power device is compatible with EPD, has high electrical conductivity and high specific capacitance. Electrochemical capacitors are based on double layer formation on the surface of the electrodes so conductive materials with high surface area have high specific capacitance and are promising electrode materials. Carbon black is often used in commercial supercapacitors because it is abundant, electrically conductive and a specific capacitance of 100-160 F/g. The material is compatible with EPD [11, 12]. Carbon aerogels 70-150 F/g [13] have similar specific capacitance to carbon black but they have a much lower energy per volume [14], which limits their usefulness for commercial applications. The more conductive allotropes of carbon, carbon nanotubes (68-160 F/g [4]) and graphene (135 F/g [15]) are of interest as capacitor electrodes due to having a higher electronic conductivity than

carbon black. CNT are of great interest because they can be made into electrodes of tunable thickness [16] and there are reports of good performance with functionalized CNT supercapacitors deposited by EPD [17].

Capacitors store energy proportional to voltage squared as indicated in figure 2.1, thus, a combination of wide voltage window electrolytes and high specific capacitance electrodes are necessary to raise the energy density of electrochemical capacitors. Defect free single walled CNT can have a voltage window of 4 V [4] but the choice of electrolyte has a tradeoff between ionic conductivity and voltage window. For electrolytes, the voltage window is determined by electrolyte degradation so chemically stable electrolytes offer wider windows. Ionic conductivity is necessary to preserve the power of the electrochemical capacitor. Aqueous electrolytes, such as sulfuric acid, are commonly used for their high conductivity 730 mS/cm but even with platinum electrodes, their voltage is limited by electrolysis of water at 1.2 V [18]. Organic electrolytes, such as propylene carbonate (PC) with tetraethylammonium tetrafluoroborate, have a wider voltage windows of 4.5 V but a lower conductivity 60 mS/cm [19, 20]. Organic electrolytes can yield large energy densities when used with CNT but they are highly flammable and often toxic [4, 21]. Room temperature ionic liquids represent an alternative to organic electrolytes that offer similar voltage windows and conductivity with fewer chemical hazards.

Room temperature ionic liquids are solvent free molten salts that exhibit moderate ionic conductivities 0.1-10 mS/cm, wide voltage windows 2-5 V and high temperature stability from below room temperature to 200 - 400°C depending on their chemistry [20]. This thermal stability combined with ionic liquid's very low vapor pressure make them suitable as electrolytes for micro supercapacitors integrated into circuits since most circuits produce excess heat. Ionic liquids have been successfully incorporated in supercapacitors to increase the energy density to

levels comparable to commercial battery systems [6, 22] . They have the additional advantage of being non-flammable, which makes them safer in the event of an electrical short [23].

Devices made with CNT and ionic liquid electrolytes have high energy density but this system is still limited by the large amount of packaging necessary with a liquid electrolyte. For capacitors, about 30% of the weight is active material while the rest is a combination of current collectors, electrolyte, binder, separator and packaging [24]. To prevent electrolyte seepage and reduce the packaging necessary for these devices, gelation or encapsulation methods can be used. While both methods can conduct ions, they have different synthesis routes, mechanisms and limitations.

Gel electrolytes are formed by increasing the viscosity of an electrolyte until it no longer flows. Two approaches to increase the viscosity are the addition of long chained polymers or the addition of nanoparticles to the electrolyte [25]. Compared to the neat electrolyte, the conductivity of gel electrolytes is greatly reduced since conductivity is inversely related to viscosity [26]. Supercapacitors have been successfully made with CNT electrodes and ionic liquids gelled with polyvinylidene fluoride (PVDF) [26, 27] but these devices will have limited thermal stability since viscosity decreases with increasing temperature. For this particular system, the ionic conductivity was preserved in the gel at 2 mS/cm compared to the 3.6 mS/cm for the neat 1-ethyl-3-methylimidazolium (EMIM) tris(pentafluoroethyl)trifluorophosphate (FAP) ionic liquid. However, the voltage window is reduced to ~ 2V from the ~ 4V of the neat ionic liquid [28] which suggests the presence of water [29]. The presence of water can increase the conductivity of the ionic liquid which could explain the lower voltage window and high conductivity [30].

The second method of gelation is the addition of nanometer diameter powders, such as fumed silica, to ionic liquids. In two recent papers, fumed silica ~10nm was added to ionic liquid to make all solid state flexible supercapacitors out of CNT [31] and graphene [32]. Even though the neat ionic liquids were very similar, EMIM bis(trifluoromethylsulfonyl)imide (TFSI) and 1-butyl-3-methylimidazolium (BMIM) TFSI respectively, both groups reported a reduction in voltage of the gel from ~ 4V for the neat liquid to ~3V and 2.5V respectively. While these voltages are reduced from the neat ionic liquid, they are still greater than the ~1V for aqueous electrolytes based on the gelation of sulfuric acid [33].

An alternative approach to gelation is the method of using sol-gel to encapsulate an ionic liquid. In the sol-gel encapsulation approach, the ionic liquid is mixed with silica precursors that are first hydrolyzed by acid and then condense into an interconnected mesoporous matrix. The mesopores of the silica encapsulate the ionic liquid, preventing seepage without reducing the viscosity of the ionic liquid. A non-aqueous sol gel route [34] can be used to minimize the water content of the encapsulated ionic liquids and the resulting ionogels can be made with a variety of ionic liquids [35].

We recently characterized the ionogel made from BMIM tetrafluoroborate (BF_4) and demonstrated that the conductivity was preserved in the ionogel [Appendix 1]. The ionic liquid BMIM BF_4 was selected for experiments because it is widely studied, commercially available, offers a 4.2V voltage window and has an ionic conductivity of 1.2 mS/cm [20]. As a continuation of our work, CNT electrodes made by EPD have been combined with BMIM BF_4 ionogel to demonstrate a prototype device with both high energy and power densities.

Chapter 2.2. Experimental

Chapter 2.2.1. Carbon Nanotube Electrodes

EPD is a versatile technique that can be used to deposit a variety of materials onto a conducting surface. EPD has been thoroughly reviewed in the literature and one of the most important features is that of having a stable suspension, which greatly improves the quality of the films [36]. CNT suspensions can be stabilized by charged functional groups, such as carboxyl groups, which can be added by exposure to nitric acid. Multiwalled CNT (30 – 70 concentric tubes, 0.5 – 200 μm in length) were purchased from Sigma Aldrich and were functionalized by heating in 12.6 M nitric acid at 60 °C for 72 hours and subsequently dispersed in common protic solvents, including water and ethanol.

The EPD apparatus consists of two parallel 304 stainless steel (SS) current collectors (McMaster Carr). The total electrode area is 2 cm^2 but only 1 cm^2 is immersed in a suspension of 1 mg CNT in 15 mL of deionized water. The deposition distance was set to 1 cm at a voltage of 14.5 VDC with 3 VAC at 0.3 MHz for 20 minutes. The AC voltage was inspired from work with dielectrophoresis of CNT to align the CNT while the DC voltage deposits them [37, 38]. This modified AC EPD has also been reviewed and has been shown to suppress bubble formation [39]. The deposition electrode assembly was designed such that the electrodes could be pulled out of the solution before turning off the deposition voltage to minimize loss of CNT. A post deposition heat treatment was performed at 200°C under 5% Hydrogen, 95% Nitrogen atmosphere for 2 hours to remove adsorbed oxygen created by electrolysis during the CNT deposition [17]. The heat treatment was performed in a tube furnace (Applied Test Systems 3210) controlled by a controller purchased from Omega (CN8240).

The CNT electrodes physical properties were characterized using scanning electron microscopy (SEM). Surface roughness and thickness was qualitatively assessed using electron micrographs taken with the Nova 230 SEM at the UCLA Laboratory of Molecular and Nano Archaeology. The mass of CNTs deposited by EPD was measured by a microbalance.

Electrochemical studies were performed following procedures from the literature to characterize the charge storage on the CNT electrodes [40]. The heat-treated electrodes were heated at 100°C under vacuum prior to being transferred into an argon filled glovebox. Cyclic voltammetry tests (VMP3 from Biologic) were performed on the CNT electrodes in a 3 neck cell. Platinum foil served as the counter and pseudo reference electrode. The electrolyte, BMIM BF_4 (BASF) was used as-received.

FTIR pellets were prepared by milling 150 μg of carbon nanotubes in 80 mg of potassium bromide. The powders were heated for 8 hours at 100^{o}C at 0.1 torr to remove volatile impurities. After pressing, the pellets were stored in a vacuum desiccator to minimize air exposure. FTIR spectra were obtained in ambient conditions using a Jasco FTIR 6100 using 4 cm^{-1} resolution and averaged over 64 scans. The data was processed using Jasco spectrum analysis with the automatic baseline function and 11-point adaptive smoothing were applied.

Chapter 2.2.2. Ionogel Electrolyte

Ionogel was formed by a non-aqueous sol-gel route using formic acid (FA) and two silanes vinyltriethoxysilane (VTEOS), tetramethylorthosilicate (TMOS) purchased from Sigma-Aldrich [Appendix 1]. The sol for the ionogel is made by mixing 2:2:5 volume ratios of VTEOS:TMOS:FA in a borosilicate glass vial heated to 39°C by a silicon oil bath in a fume hood. After 19 minutes of magnetic stirring, the sol was pipetted into a polyethylene vial

(McMaster-Carr) at room temperature. BMIM BF_4 which was stored in an argon box to minimize water absorption, is added to the sol so that 72% of the liquid in the vial is ionic liquid. The ionogel viscosity rapidly increases after mixing until the ionogel is fully condensed, typically within an hour after adding the ionic liquid to the sol.

Chapter 2.2.3. Carbon Nanotube Supercapacitors

Supercapacitor devices with parallel plate geometry were made by combining the CNT electrodes with the ionogel. EPD was used to deposit 190 µg of CNTs onto 1 cm^2 SS electrodes masked by layers of teflon tape. The teflon mask exposed 0.36 cm^2 base wells that are 120µm tall (all energy storage test values are normalized to the full 1 cm^2 area). Devices were formed by drop casting 20 µL of ionogel into the teflon well 1 minute after the addition of the $BMIMBF_4$ to the sol. The top electrode was placed CNT side inward to complete the device fabrication. The device is then dried in ambient conditions for 30 minutes prior to a second heat treatment and testing.

Devices were heated at 50°C for 3 hours then at 100°C for 2 days. Nickel wires were added with silver epoxy (Epotek H20E) to the two stainless steel current collectors. Devices were transferred hot into a polycarbonate measurement apparatus (NEMA 4 enclosure with added electrical and gas connections) shown in figure 2.2. The air in the enclosure was exchanged by flowing argon during device testing to provide a dry environment.

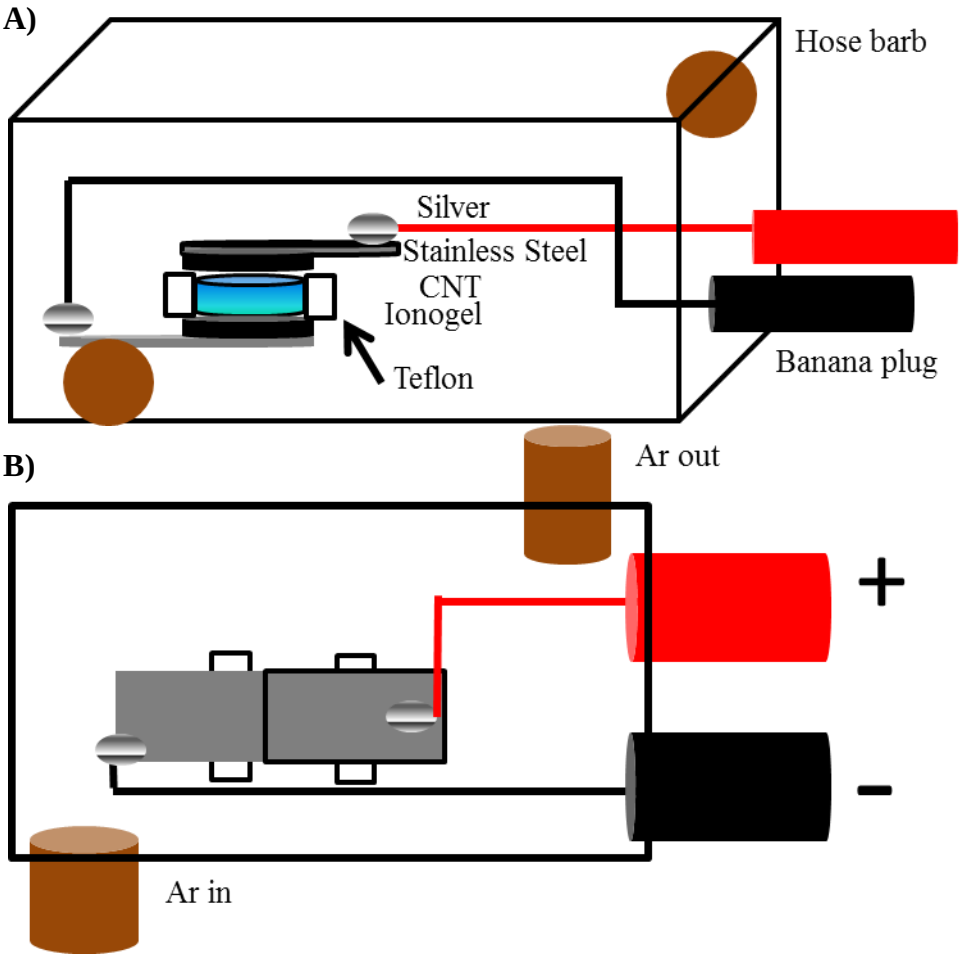

Figure 2.2 Diagram of the supercapacitor device testing apparatus A) Side profile B) Top view

The impedance of the supercapacitors was measured by a Solartron 1287 and 1252a potentiostat and function generator respectively. Impedance measurements were performed with 13 mV AC amplitude, 0 V DC bias at 10 steps per decade of frequency in the range of 10^{-2} to 10^{5} Hz. Impedance hysteresis testing was performed with a 13 mV AC amplitude at 1 frequency step per decade in the range of 10^{0} to 10^{5} Hz, while cycling the DC bias voltage from -2.5 V to 2.5V at 1000 points per sweep. Electrochemical measurements included cyclic voltammetry and galvanostatic cycling. Cyclic voltammetry was performed at 100 mV/s from 2-3.75V in a two electrode configuration. Galvanostatic cycling is the accepted measurement technique for device

performance since it emulates the mode of operation for an energy storage device [41]. 10 galvanostatic cycles were performed from 0.5 to 20 mA/s. Leakage measurements were performed by applying a staircase voltage from 0-3.75 V at 5 minutes per step. The steady state current after 5 minutes was used as the leakage current for that voltage.

Chapter 2.3. Results and Discussion

Chapter 2.3.1. CNT Electrode

The CNT electrodes used in this experiment were deposited into dense interwoven mats shown in figure 2.3 A and figure 2.3 B. From the glovebox testing of the CNT electrodes, the cyclic voltammetry plot in figure 2.3 C shows that the deposited CNTs have a wide electrochemical window of 3.8 V and an ideal box shape response. This voltage window is nearly the full value of 4 V for pristine CNTs [4]. There are small oxidation and reduction peaks likely belonging to functional groups, which occur after hydrogen treatment and have also been observed in literature [40]. The existence of these small peaks prompted further characterization by spectroscopy.

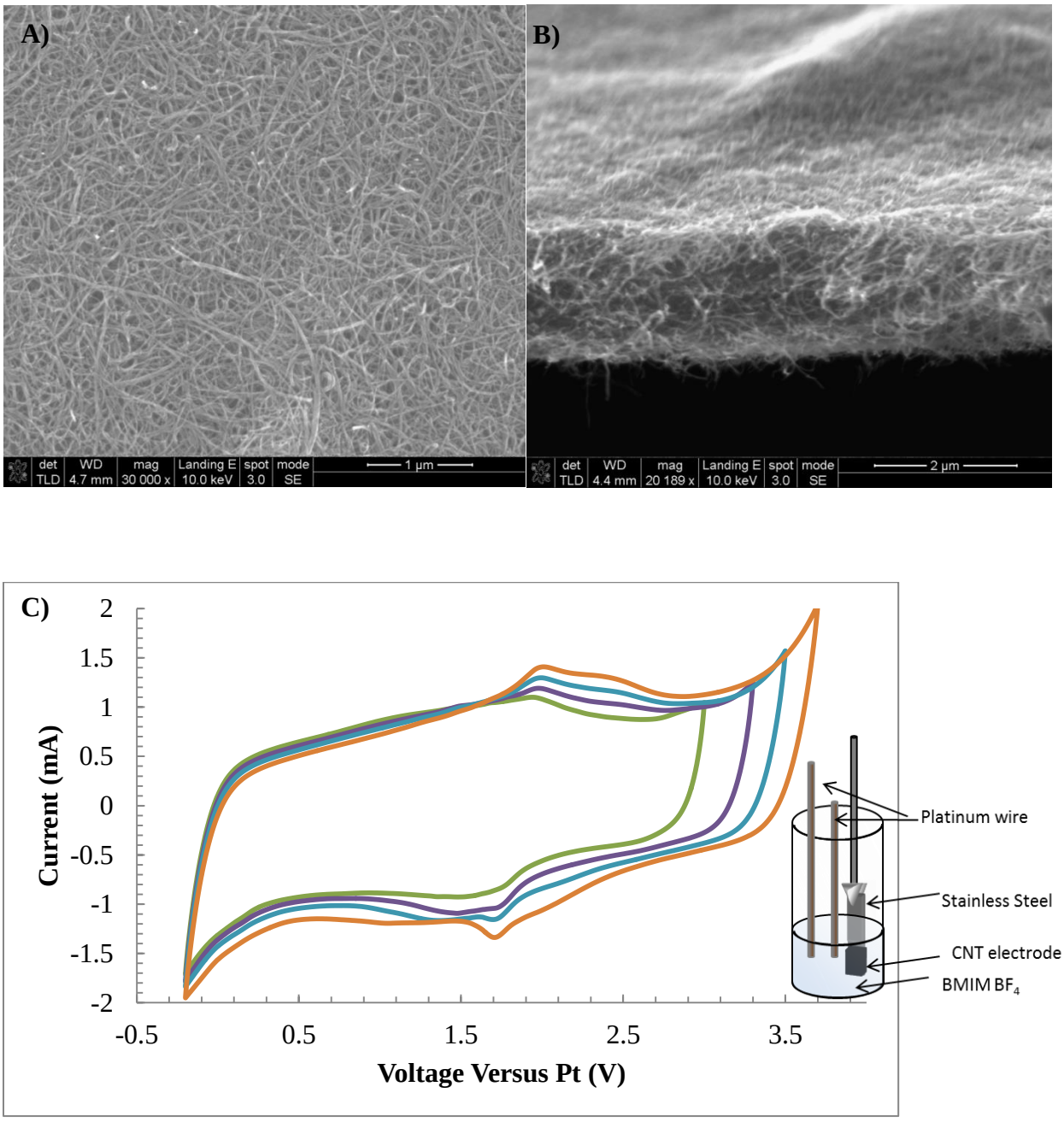

Figure 2.3 SEM of CNT electrodes from A) Top down view and B) a cross section view showing the film thickness to be 3 µm C) Three electrode cyclic voltammetry at 100 mV/s (platinum foil counter, platinum wire reference) of CNT electrode deposited by EPD after hydrogen treatment (SEM by Leland Smith)

Fourier transform infrared spectroscopy (FTIR) was used to identify the chemical functional groups present on the CNT. It is well known that oxidizing agents such as nitric acid

can produce a wide variety of oxygen-containing functional groups such as aldehyde, ether, ester, carbonyl, phenol, carboxylic acid and carboxylic anhydride, on carbon nanotubes [42]. One simple way of classifying these groups is whether they contain single or double-bonded oxygen. The region of the FTIR spectrum from around 1250 to 1850 cm^{-1} is particularly useful because therein lie three peaks at 1720, 1560 and 1390 cm^{-1} which correspond to C=O stretching, C=C stretching and CO-H bending, respectively [43]. As shown in figure 2.4, the as received nanotubes have a relatively flat signal with a small peak associated with C=C. After oxidation, the C=C peak increases in amplitude and a C=O peak appears as well as a CO-H peak. After EPD there is chemical change in the nanotubes supported by the decrease in the C=O peak and the increase in the CO-H peak.

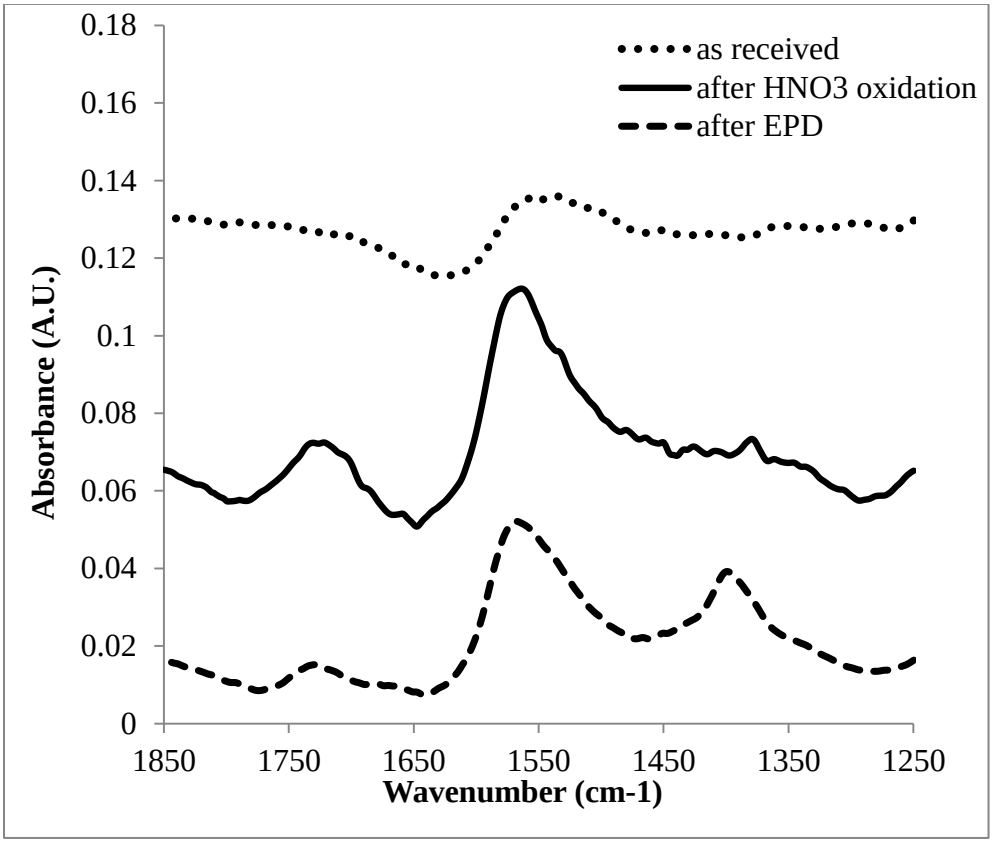

Figure 2.4 FTIR spectra for the CNTs at different stages of the electrode preparation (FTIR by Leland Smith)

Chapter 2.3.2. Supercapacitors

The electrochemical properties of fully assembled supercapacitors were determined using cyclic voltammetry. The results are shown in figure 2.5. The supercapacitor retains its box shape and the small peaks from the individual electrode in figure 2.3 are no longer visible in figure 2.5. The scans show a steady reversibility of 88% up to 3.75 V, which is a very large window for an encapsulated electrolyte. The upward slope at the high voltages reduces after each cycle and is likely moisture leftover from exposing the ionogel to air during synthesis.

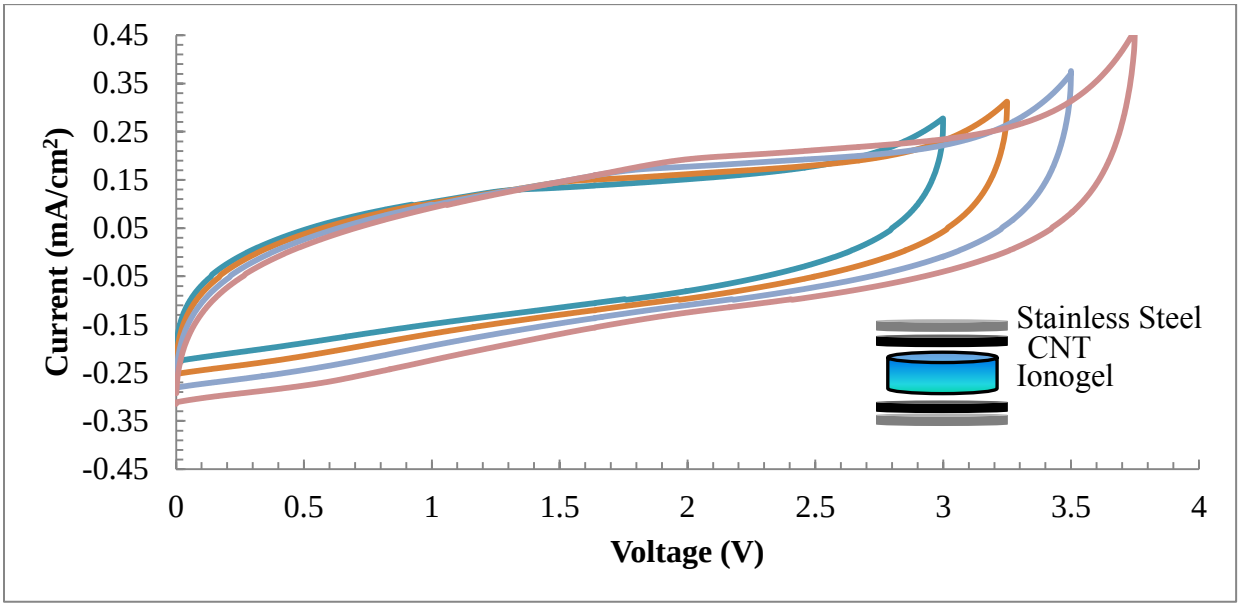

Figure 2.5 Cyclic voltammetry of the CNT device at 100 mV/s in a two electrode configuration showing box like scans up to 3.75 V

Following the cyclic voltammetry scans, galvanostatic cycling was performed to study charge storage characteristics under conditions representative of applications. The current levels were chosen to give discharge times slower and faster than the typical commercial capacitor, which is discharged in a few seconds [41]. In figure 2.6, the galvanostatic cycling becomes slightly more triangular at faster scan rates, which is consistent with other reported CNT

supercapacitors [27]. From the galvanostatic cycling, the rate capability was determined and is shown in figure 2.7. Areal capacitance was used instead of gravimetric performance since the energy stored over a given footprint area is more important for a micro supercapacitor than the mass of the electrodes. The capacitance as a function of current demonstrates similar trends to other CNT devices in the literature with the stored energy falling off at higher current densities [44].

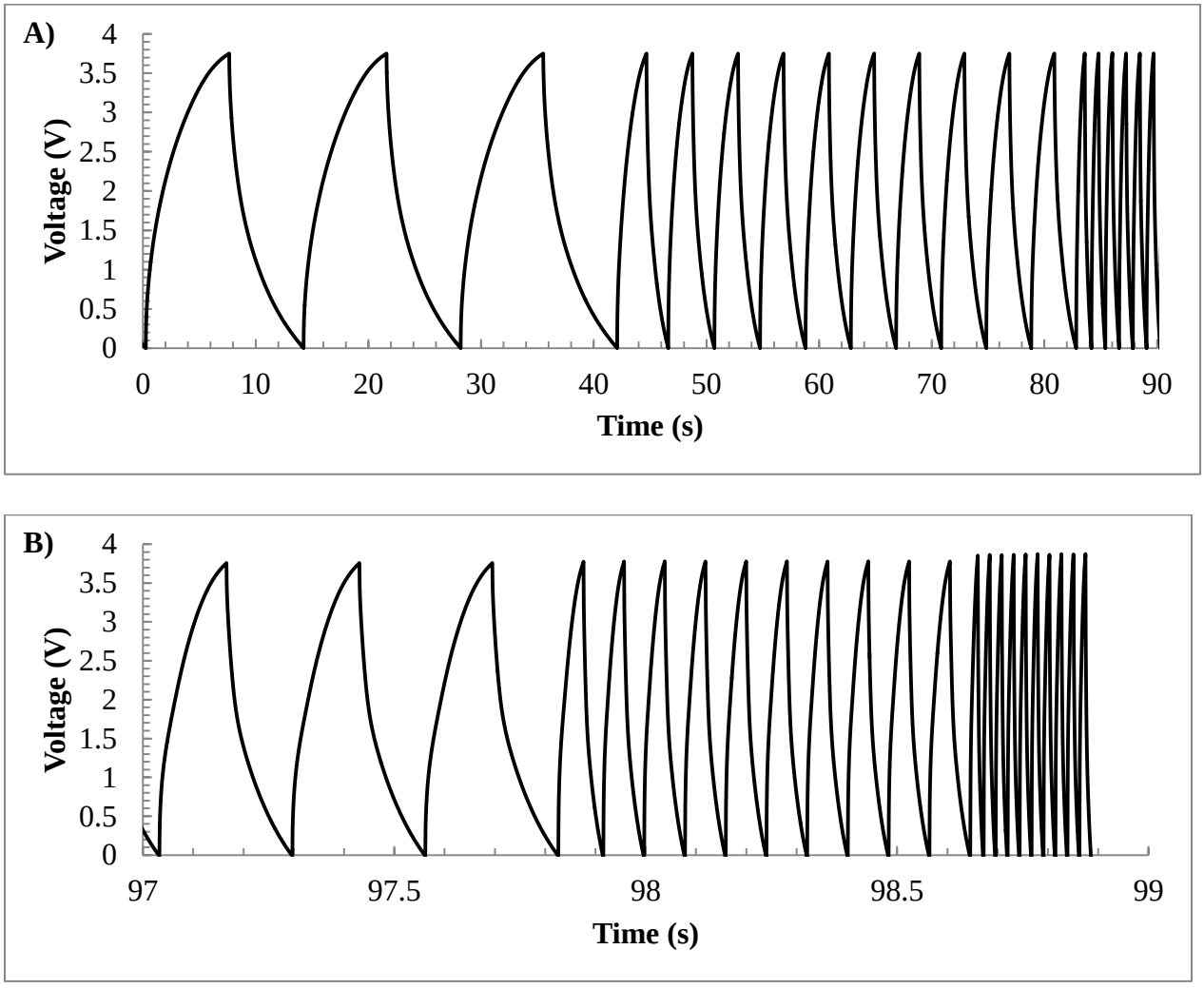

Figure 2.6 Subset of galvanostatic cycling of CNT devices at A) Current densities of 0.5 mA to 2 mA and B) 5 mA to 20 mA showing slightly sharper curves at higher scan rates

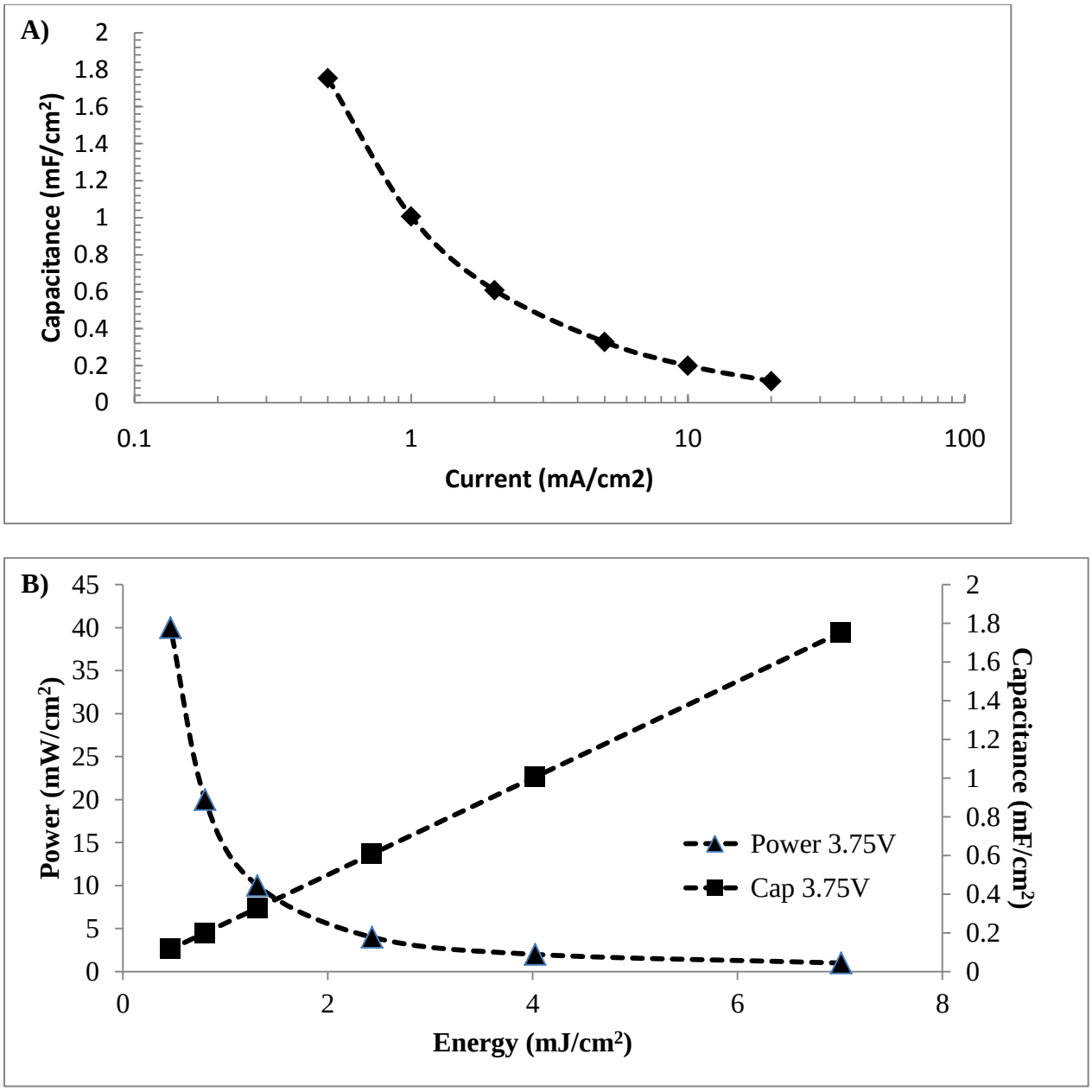

Figure 2.7 A) Areal capacitance as a function of galvanostatic charging and discharging rate for the CNT ionogel devices B) Power versus energy for the same date. In both plots, the current is normalized to the device footprint area of 1cm^2

Galvanostatic cycling is useful for measuring the stored energy but electrochemical impedance spectroscopy gives more details about device properties such as equivalent series resistance (ESR) and hysteresis. The nyquist plots in figure 2.8 A and figure 2.8 B show the

characteristic semicircle associated with ion transport and a diffusion tail due to the porous nature of the CNT electrodes [7]. The impedance was modeled using the standard randles circuit [8] shown in figure 2.8 E. From the modeling, the ESR was found to be 8 Ω and by attributing the ESR to the ionogel and accounting for device geometry, the conductivity of the ionogel is 1.4 mS/cm, which matches previous reports [Appendix 1]. Using the ESR and the modeled capacitance of 0.5 mF, the characteristic RC time constant is 4 mS. While this device has a good response time, it is similar to other reported micro supercapacitors with leakage currents evident from the phase angle not reaching -90° [9] shown in figure 2.8 C.

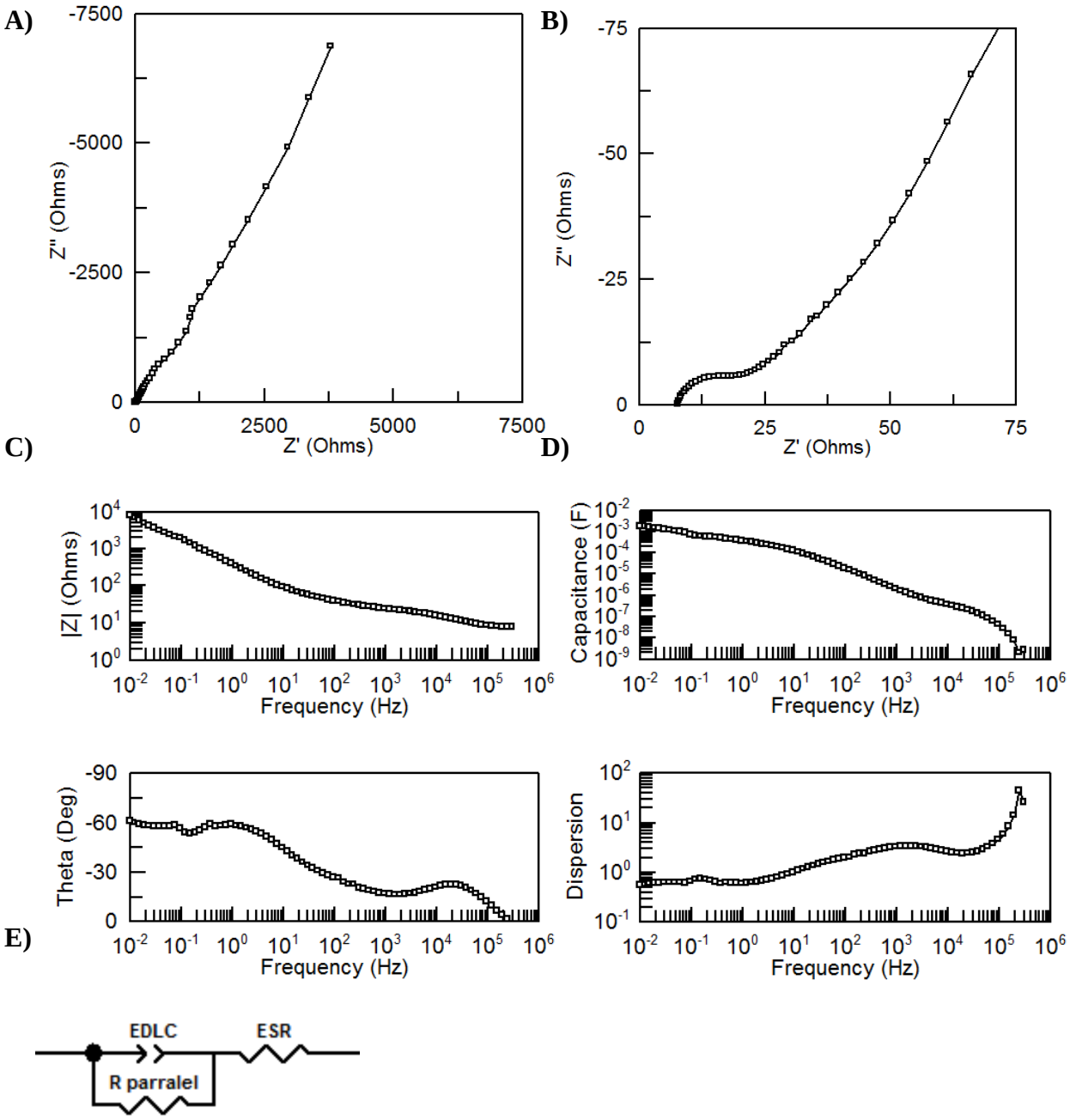

Figure 2.8 Impedance of the CNT ionogel capacitors in A) Nyquist plot with B) Zoom in near the axis C) Bode plot and D) Capacitance and dispersion measured in the parallel configuration E) Equivalent circuit used for modeling containing two resistors and a constant phase element (CPE)

Leakage current is of greater concern in smaller devices where even low rates of leakage can quickly drain the energy stored in the device. For this device, the leakage current increases

non-linearly with voltage as shown in figure 2.9. Leakage current is a common problem for supercapacitors and using higher purity materials can reduce the rate of self discharge [45]. This leakage current is the source of the dispersion as seen in figure 2.8 D. More aggressive heat treatments or a more open device architecture could further remove impurities from the system and minimize the leakage current.

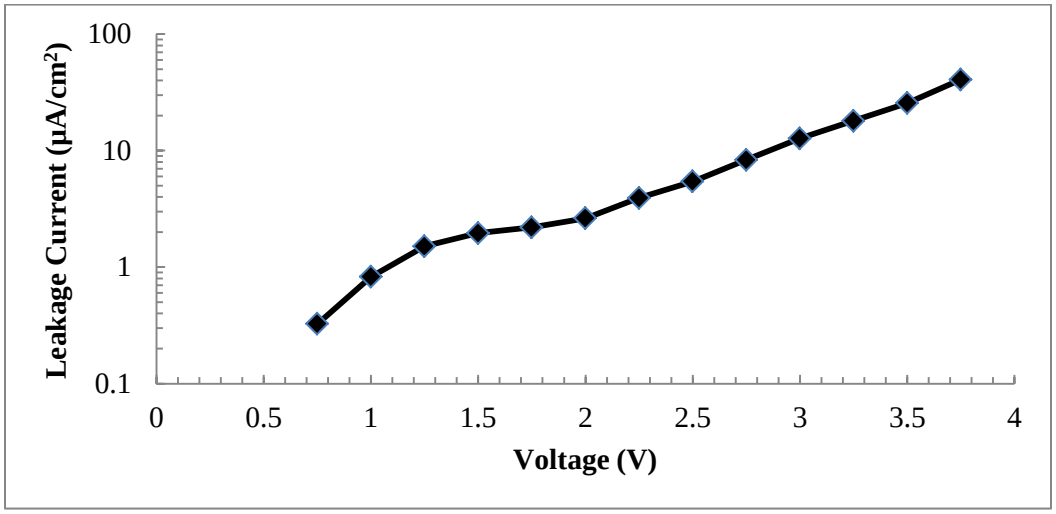

Figure 2.9 Device leakage current as a function of voltage showing a non-linear dependence

When considering the quality of the device, capacitance hysteresis is a significant concern because it changes the current delivered at a given voltage. Hysteresis commonly occurs with ionic liquids due to counter ion absorption and over screening as a result of the high ion concentration [46]. In the device, hysteresis is evident at frequencies lower than the characteristic time constant ~10^3 Hz shown in figure 2.10 A-C. This behavior is consistent with literature [47]. For frequencies greater than the characteristic time, > ~10^3 Hz, the hysteresis is negligible as shown in figure 2.10 D.

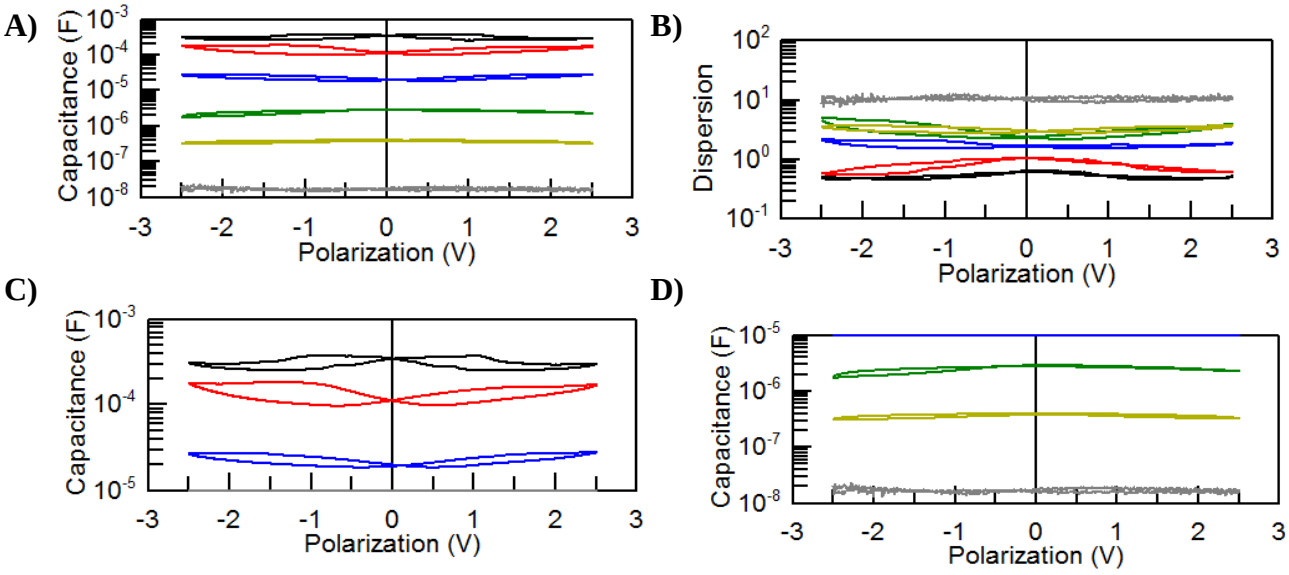

Figure 2.10 Polarization plots displaying A) Capacitance and B) Dispersion for the device. C) Zoom in of the capacitance at high frequency, 10^3- 10^5 Hz D) for low frequency 10^0-10^2 Hz

There are many options for fabricating micro-supercapacitors as well as choices for electrodes and electrolytes. A subset of the literature on micro supercapacitors, those with carbon electrodes, liquid electrolytes and active area electrode thicknesses less than 100 µm, were used to make table 2.1. The energy storage properties were scaled by the active electrode footprint area and the devices are compared at similar powers. From table 2.1, the CNT ionogel supercapacitor offers one of the highest areal energy density per device thickness even when compared to devices that use higher ionic conductivity neat electrolytes such as PC with dissolved salts like tetrabutylammonium tetrafluoroborate (TBAF).

Table 2.1 Comparison of literature of micro supercapacitor devices with their energy storage performance scaled to the footprint of the active material.

Device	Structure	Electrolyte	Voltage	Capacitance (mF/cm^2)	Power (mW/cm^2)	Thickness (μm)
AC [9]	Interdigitated (20)	TBAF PC	2.5	0.4	10	2
C Onion [5]	Interdigitated (16)	TBAF PC	3	3.6	1.7	7
LSG [6]	Planar	EMIM BF_4	4	3.2	13.3	7.6
AC [48]	Interdigitated (16)	$NaNO_3$ Aqueous	1	90.7	51.5	50
CNT [49]	Interdigitated (30)	BMIM BF_4	1	0.428	0.28	80
CNT	Planar	BMIM BF_4 ionogel	3.75	1.5	15	3

Chapter 2.4. Conclusions

In the field of micro supercapacitors, there are many different choices for materials and techniques, but there is a common goal of achieving high power and high energy devices. Electrophoretic deposition has advantages in its selectivity, simplicity and binder free process over other electrode deposition techniques. These CNT electrodes show volumetric energy density comparable to the highest reported values in literature. Combining these electrodes with the platform of the ionogel, we have shown a prototype quasi solid-state supercapacitor that preserves the majority of the properties of the neat components. The encapsulation of the ionic liquids provides benefits in packaging without negatively affecting the ionic conductivity of the ionic liquid. Combining these advances leads to a robust capacitor suitable for miniaturization into a micro supercapacitor.

Chapter 3. Characterization of Orthorhombic Nb_2O_5 by In-Situ Impedance Spectroscopy

Chapter 3.1. Introduction

Electrochemical energy storage is an exciting research topic that is driven by the discovery of new materials that store more energy with higher rate capability. Within the category of electrochemical capacitors are the traditional non-faradaic electric double layer capacitor (EDLC) and the high energy density faradaic pseudocapacitors. EDLCs store energy in the electric double layer that forms between the charged electrodes and the ions in the electrolyte. A high performance EDLC is a material with high electronic conductivity and high surface area but for pseudocapacitors, these metrics are more complex.

Pseudocapacitors are materials that display fast faradaic reactions that result in high capacitance independent of surface area. Many transition metals display pseudocapacitance with numerous studies performed on oxides of ruthenium, manganese, niobium and vanadium. The bulk of the research on pseudocapacitors is driven by the search for a replacement for hydrous ruthenium oxide, a metallic conductor with a theoretical specific capacitance of 1358 F/g [3] shown in table 3.1. Ruthenium oxide sets the standard for pseudocapacitors with its combination of high conductivity and large capacitance, but its high material cost prohibits it from practical applications [50].

Table 3.1 Specific capacitance of pseudocapacitors and their electronic conductivities

Material	Capacitance (F/g)	Electronic Conductivity (S/cm)
Hydrous RuO_2	750 [51]	$3 * 10^{2}$ [51]
V_2O_5	350 [51]	10^{-6} [52]
MnO_2	800 [3]	10^{-5} to 10^{-6} [53]
MoO_3	300 [54]	10^{-7} to 10^{-9} [55]
Nb_2O_5	450 [56]	$8* 10^{-11}$ [57]

When considering pseudocapacitor materials for high energy storage applications, there are a few parameters to consider including: electronic conductivity, specific capacitance, material cost and material toxicity. High electrical conductivity allows for thicker electrodes and can be either intrinsic to the material, as in the case of RuO_2, or achieved with the addition of conductive additives as in the case of V_2O_5 [52]. V_2O_5 offers high specific capacitance with a lower material cost than RuO_2 but V_2O_5 is unfortunately, a highly toxic material [58]. An alternative earth abundant material that does not have the toxicity of V_2O_5 and has good performance as a pseudocapacitor is Nb_2O_5.

Nb_2O_5 is of interest because certain crystal phases display large energy storage and high rate capability in lithium systems [59]. The orthorhombic T and pseudohexagonal TT phases, demonstrate large capacitance of 450 and 350 F/g respectively with a charging time of 250 seconds [56]. Previous work in the literature identified the charge storage for T Nb_2O_5 as being from the bulk of the material instead of just the surface. Sodium electrolyte was substituted for lithium electrolyte and the resulting decrease in measured specific capacitance confirmed that the lithium intercalates into the bulk of the Nb_2O_5 [56]. This intercalation into the bulk is facilitated by the layered structure of the T-phase, which allows for easy insertion of lithium. The current

study is on understanding how semiconducting Nb_2O_5 with a 3.3 eV band gap [60] can have high rate capability, which is characteristic of materials with high electrical conductivity.

Understanding the mechanism for the high rate capability of Nb_2O_5 is beneficial in considering new approaches for electrochemical capacitors with thicker electrodes. One explanation for the high rate capability of Nb_2O_5 is increased electrical conductivity after lithiation by up to four orders of magnitude [57]. The proposed mechanism for the increased conductivity is that lithium intercalation into the Nb_2O_5 creates oxygen vacancies which are known to be much more conductive than stoichiometric Nb_2O_5 [61]. These oxygen vacancies result in delocalized $4d^1$ electrons, which improves the electrical conductivity from 10^{-5} S/cm to greater than 10 S/cm depending on the concentration of Nb^{4+}. It has been shown by x-ray absorption near edge spectroscopy that the concentration of Nb^{4+} increases during lithiation [59]. The limitation in the previous work is that the conductivity was only measured at discreet levels. This study focuses on determining how the electrical conductivity of the Nb_2O_5 changes as a function of lithiation and temperature to provide insight regarding this material's high rate capability.

Electrochemical impedance spectroscopy is a common technique for measuring the conductivity of a material because it can be combined with modeling to determine what parts of the system are contributing to the material's response. There have been reports of ex-situ lithiation of MoO_3 in which measurements on individual α -MoO_3 nanobelts show an increase in conductivity from 10^{-4} S/cm to 10^{-2} S/cm after lithiation [62]. While ex-situ experiments are useful, it is ideal to test the material during lithiation to minimize sample handling and better monitor the sample's state of charge. Following work on in-situ measurements of amorphous silicon, at least one of the contacts for the impedance needs to be completely isolated from the

electrolyte [63]. By isolating one of the impedance electrodes, the material can be tested while immersed in electrolyte, which allows for in-situ testing during galvanostatic cycling. Dense films of material allow for accurate measurements of the material geometry as well as minimizing the current collector's interaction with the electrolyte. Sol-gel chemistry combined with spin coating is a very useful route for fabricating dense films of Nb_2O_5.

Sol-gel chemistry is a versatile route to synthesizing metal oxides without the need for high temperature reactions such as those found in solvothermal or hydrothermal synthesis. Sol-gel is a two part reaction where a precursor is hydrolyzed, often by an acid, and terminates with hydroxyl groups [64]. The second reaction is between hydroxyls in the presence of a base where water is produced and the precursors link in a process known as condensation [65]. There are many routes to forming Nb_2O_5 mainly using $NbCl_5$ precursors with the addition of an alcohol, often ethanol, and then adding an acid from the following: HCl [66], H_2SO_4 [67] or acetic acid [68]. $NbCl_5$, ethanol and water is a simple system to use for investigating Nb_2O_5 [69] with reports that the final oxide is not heavily dependent on the chemistry used to form the Nb_2O_5 [70]. The precursor solution can be spin coated than heated between depositions to build µm thick layers of Nb_2O_5 [69, 70].

The ability to make thick layers of amorphous Nb_2O_5 by spin coating is promising for impedance spectroscopy but the focus of this study is on the crystalline material. Reports in the literature for Nb_2O_5 as an electrochromic [71] state that heating to 600 °C in air will crystalize amorphous Nb_2O_5 into the orthorhombic T phase. Using a current collector such as indium doped tin oxide (ITO) or fluorine doped tin oxide (FTO) deposited on glass is advantageous since these substrates are only conductive on one side, which minimizes the current collector's

interaction with the electrolyte. FTO is a better choice of substrate for this experiment since it has a higher thermal stability than ITO and is stable to 600 °C [70].

Producing dense films of orthorhombic Nb_2O_5 films on FTO allows for in-situ testing of the electrical conductivity of Nb_2O_5 during the lithiation of the film. Along with conductivity, activation energies are useful in characterizing material performance at elevated temperature and can be measured by using a testing fixture that can be slightly heated. Activation energy can be measured using the Arrhenius relation [72] shown in equation 3.1. This measurement setup also allows for the study of phase changes which can occur at lower temperature for lithiated structures [73]. Phase changes can be observed by changes in the x-ray diffraction spectra (XRD).

$$\sigma = \sigma_o \, e^{\frac{-E}{\kappa T}}$$

Equation 3.1 Arrhenius relation showing the exponential dependence of conductivity σ on activation energy E, Boltzmann's constant κ and temperature T

Chapter 3.2. Experimental

Dense crystalline Nb_2O_5 films for impedance testing were synthesized using a sol-gel reaction. The sol was formed by 0.96 g of $NbCl_5$, (Sigma Aldrich) combined with 10 ml ethanol and 0.6 ml of deionized water. The mixture was reacted for one day and ultrasonicated prior to spin coating. 150 µL of sol was drop cast onto 2 cm^2 of FTO masked by mylar tape. The samples were first spun at 1500 rpm for 60 seconds followed by 6000 rpm spin for 60 seconds with a ramp rate of 500 rpm per second. After spincoating, the tape was removed and the samples were annealed at 300 °C for 12 hours followed by heat treatment at 600 °C for 2 hours at a heating rate of 3 °C per minute in air to crystallize the film.

To measure the impedance of the films an insulated top electrode needed to be added to the film. Copper tape was chosen for its high conductivity and ease of addition. The copper tape was first affixed to a clean glass slide and then scored to 1 cm in length with a width of 1.5 mm and 2 mm for samples A and B, respectively. These copper strips were pressed onto the film then covered by 2.5 mm wide kapton tape. The kapton tape is an electrochemically inert material that serves as physical insulation between the copper tape and the electrolyte. The electrode configuration is shown in figure 3.1

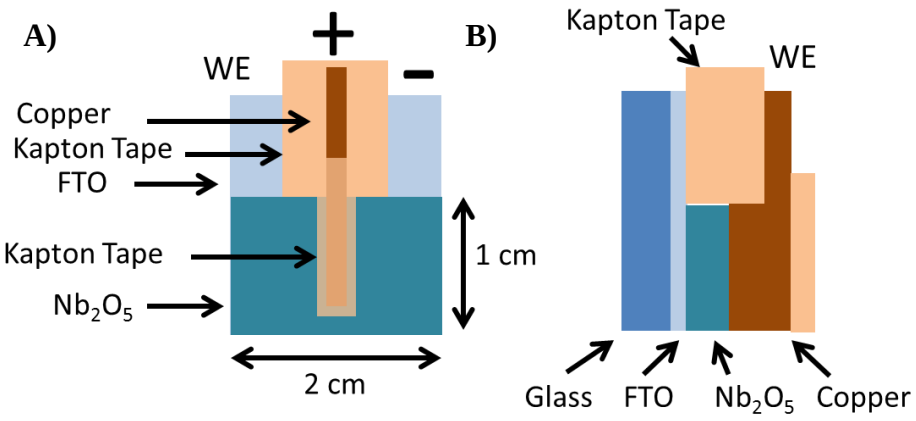

Figure 3.1 Impedance test geometry for conductivity testing A) Front profile B) Side Profile

The impedance measurements were conducted using a VMP3 from Biologic with a 13 mV AC amplitude at 6 points per decade from 10 to 10^6 Hz. As a complementary conductivity test, DC measurements were performed by sweeping the voltage from the positive and negative connections shown in figure 3.1 between -5 and 5 mV at a sweep rate of 1 mV/s. The measured current was then related back to resistance using ohm's law.

Sample thickness and uniformity was measured by scanning electron microscopy (Nova 230 SEM at the UCLA Laboratory of Molecular and Nano Archaeology) of a sample cross sectioned

by a diamond saw. Gold sputtering was used to coat a few nanometers of gold onto the sample to prevent charging by the electron beam and improve the image quality.

The Nb_2O_5 films were electrochemically lithiated using a 3 electrode cell with lithium foil as the counter and reference electrodes. 1M $LiClO_4$ in propylene carbonate was used as the electrolyte. Electrochemical lithiation was performed in an argon filled glovebox (VAC) using the VMP3. A control experiment was performed with cyclic voltammetry at scan rates from 0.1 to 10 mV/s that ended at 2.99 V versus lithium and were followed by 30 seconds of open circuit voltage (OCV) periods to measure the polarization of the film at high sweep rates without the top electrode. Galvanostatic cycling was performed from C/4.3 to 2C rates to study the charge storage of the material. A 30 second OCV period followed each change in current density.

The testing of the Nb_2O_5 with copper electrodes used two synchronized channels to measure the impedance and the OCV simultaneously. The first channel alternated between galvanostatic cycling at a 2C rate and the OCV setting. During the OCV, the second channel measured the impedance through the film as well as the DC conductivity sweep within 30 seconds as shown in table 3.2.

Table 3.2 Testing parameters for the synchronized channels during the in-situ conductivity testing

Time (s)	**200**	**29**	
Channel 1	Galvanostatic cycling	OCV	Loop
Channel 2	OCV	Impedance DC Sweep	Loop

Temperature dependence measurements from room temperature to 46 °C were carried out using a hot plate in the glove box to minimize electrolyte evaporation. The temperature was

monitored by an immersion thermocouple and the temperature was held for 45 minutes prior to the start of testing.

Samples for XRD were prepared by drop casting the sol onto FTO and then annealing with the same conditions as the samples for impedance testing. Two samples were prepared, one of the heat treated Nb_2O_5 before cycling and the other after cycling at 37 °C. These thicker films were then scraped from the FTO substrate and the powder was loaded into Rigaku Miniflex II diffractometer equipped with a Cu Kα radiation source for XRD testing.

Chapter 3.3. Results and Discussion

Chapter 3.3.1. Physical Characterization

The first experiments verified that the desired phases of Nb_2O_5 were being prepared. The XRD spectra of the heat treated Nb_2O_5 is shown in figure 3.2 along with the reference spectra for the orthorhombic phase. The peaks match the orthorhombic phase, which agrees with the literature reference for a 600 °C anneal producing the orthorhombic phase [71].

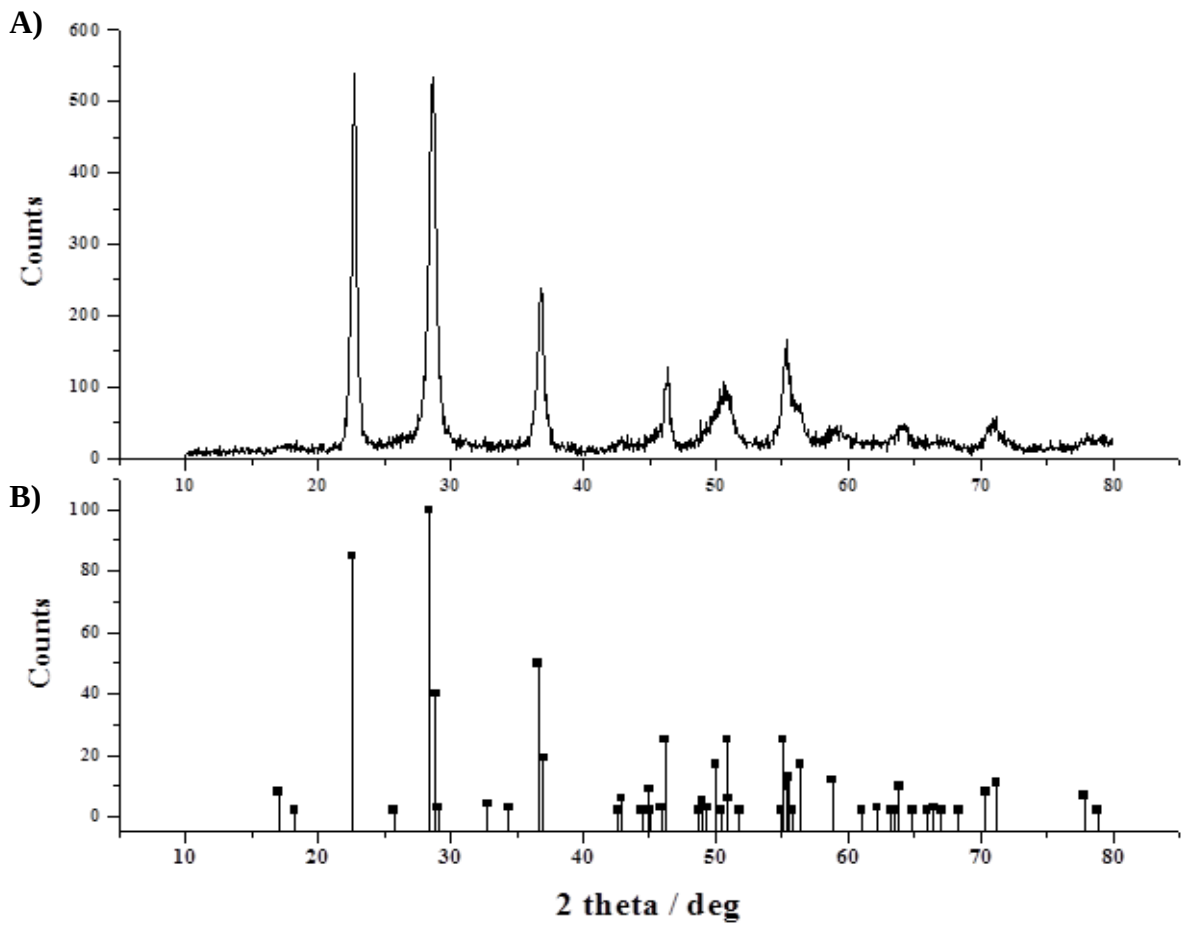

Figure 3.2 Powder XRD of Nb_2O_5 A) After heat treatment B) JCPDS (30-873) for the orthorhombic phase (XRD by Hyungseok (Jimmy) Kim)

The density and uniformity of the film are important parameters when considering the device geometry for conductivity measurements. The cross section shown in figure 3.3 displays the spin coated Nb_2O_5 with minimal roughness and a thickness of about 100 nm. The film appears fully dense which verifies the usefulness of spincoating.

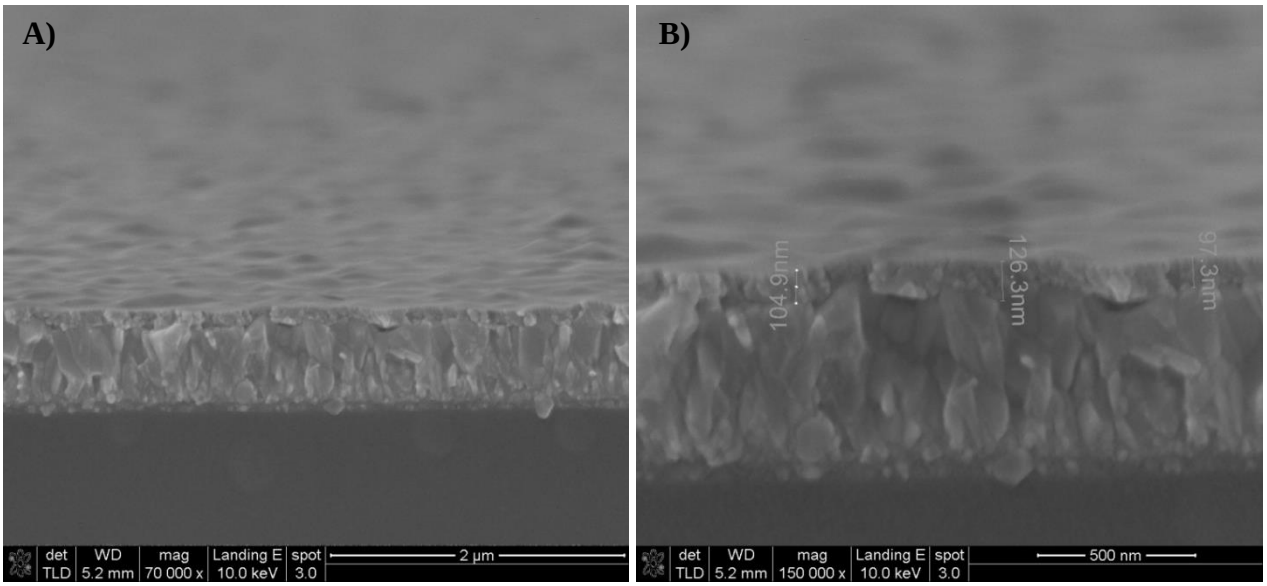

Figure 3.3 A) SEM cross section of annealed T phase Nb_2O_5 on FTO B) Increased magnification with scale bars (SEM by Hyungseok (Jimmy) Kim)

Chapter 3.3.2. Room Temperature Electrochemical Testing

Cyclic voltammetry was used determine the energy storage of the Nb_2O_5 films as well as study the material polarization . Cyclic voltammetry from figure 3.4 A shows that the different sweep rates have the same shape, which is expected for a material with good rate capability, and this shape matches the T phase Nb_2O_5 from literature [56]. There is evidence of the material being far from equilibrium since in each OCV period following the cyclic voltammetry, the voltage steadily falls from 2.99 V to the values shown in figure 3.4. This voltage drop during OCV becomes larger after the faster cyclic voltammetry sweeps and suggests material polarization.

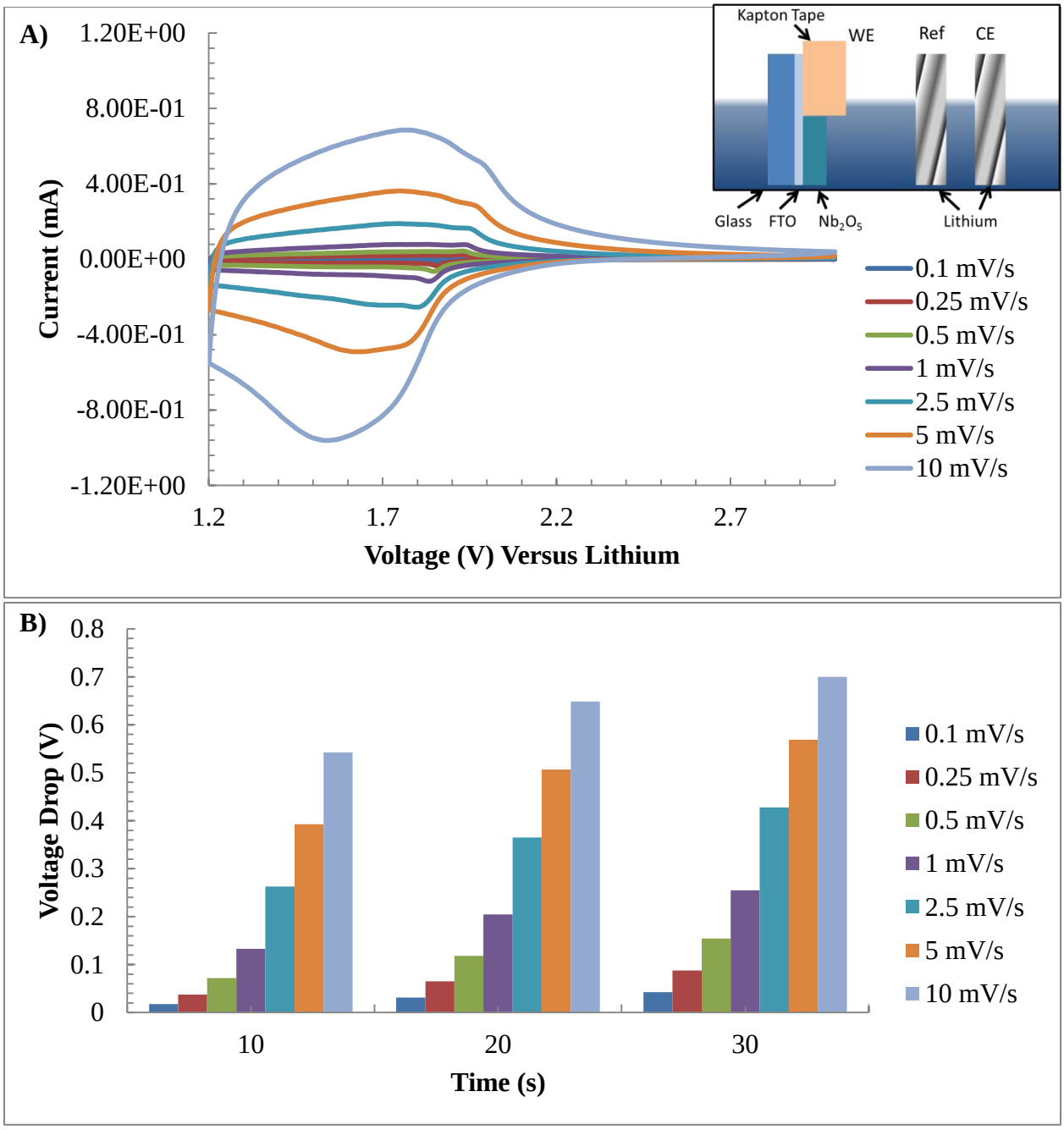

Figure 3.4 A) Cyclic voltammetry of T phase Nb_2O_5 films in a 3 electrode cell with lithium as the counter and reference electrodes. B) Difference in OCV from 2.99 V after cyclic voltammetry at different sweep rates

After cyclic voltammetry, galvanostatic cycling was used to quantify the amount of charge necessary to change the voltage of the Nb_2O_5 by the amount observed in figure 3.4 B. The galvanostatic cycling is shown in figure 3.5 and it is clear that very little energy is stored from

2.4 to 3 V. The linear shape of the galvanostatic cycling is typical of a capacitor and the total energy stored during galvanostatic cycling matches well with the cyclic voltammetry experiments.

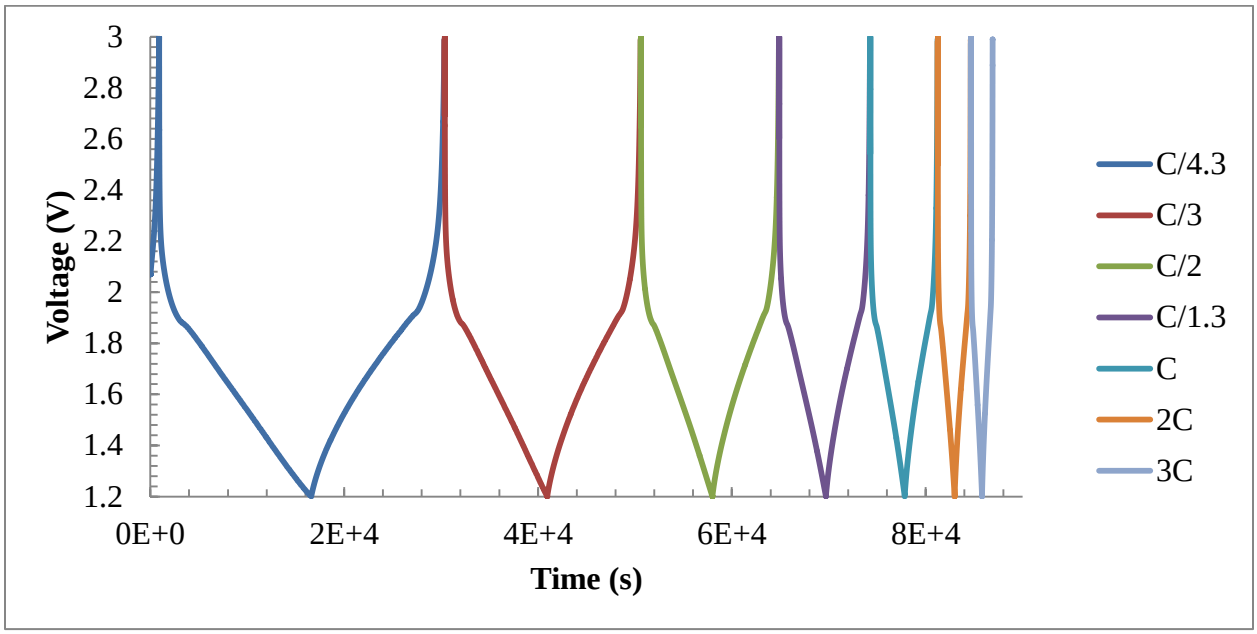

Figure 3.5 Galvanostatic cycling of Nb_2O_5 working electrode in a 3 electrode cell with lithium as the counter and reference electrodes

Each galvanostatic current density was followed by an OCV that was then followed by charging back up to 2.99 V versus lithium. This galvanostatic charging period was integrated to give a quantitative measure of the charge necessary to compensate for the polarization of the electrode. Dividing the polarization charge by the total charge stored by the material, results in values less than 1% as shown in table 3.3. This minimal loss in charge due to polarization allows for testing at a 2C rate. The advantage of testing at this high rate is that when the 5 electrode cell is heated at high temperature, the rate of electrolyte evaporation will not greatly change the amount of film submerged in electrolyte.

Table 3.3 Voltage drops during OCV between galvanostatic cycling experiments

Rate	Lithiating (mAs)	Polarization (mAs)	Percentage Loss	Voltage Drop (V)
C/4.3	68.085	0.08	0.12%	0.308
C/3	65.567	0.103	0.16%	0.352
C/2	63.99	0.125	0.20%	0.397
C/1.3	62.57	0.177	0.28%	0.457
C	61.51	0.177	0.29%	0.500
2C	60.147	0.321	0.53%	0.609

With the initial conditions determined, the testing on the copper electrode samples could begin. Sample A was tested in argon using the DC sweeps prior to any contact with lithium or electrolyte. The electronic conductivity was measured at $1.8 * 10^{-11}$ S/cm, which is in line with literature values [57]. After this initial test, Sample A was submerged in electrolyte in the cell depicted in figure 3.6 and tested by alternating cycles of galvanostatic cycling and OCV periods. Evidence of polarization occurs during the voltage drops during the OCV periods as shown by the voltage as a function of time in figure 3.6. Both the lithium insertion and removal show similar behavior.

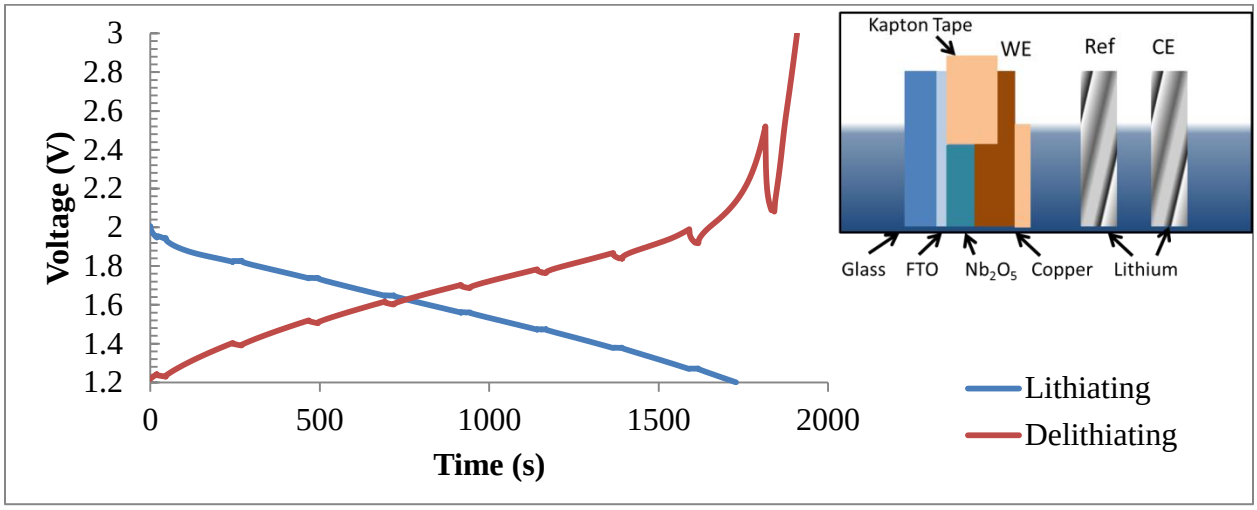

Figure 3.6 Galvanostatic cycling at 2C for the in-situ impedance testing using a 5 electrode cell

During the OCV period, the conductivity was measured by two complementary methods. The first method is by impedance shown in figure 3.7, which displays a depressed semicircle that decreases in size with increasing lithium intercalation. This semicircle was fitted to the circuit in figure 3.7 A that has a constant phase element (CPE) defined by the equation in figure 3.7 C. The CPE allows for a better fit to the data and can be related to the capacitance of the film by the equation in figure 3.8 D [74]. This circuit corresponds to samples with mixed ionic and electronic conduction [75].

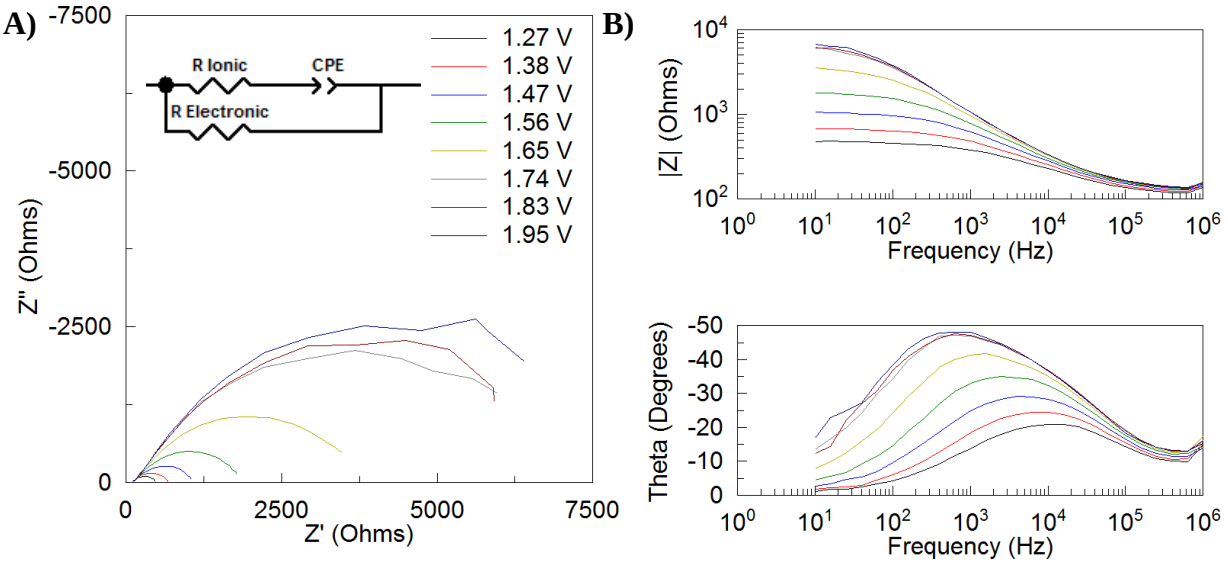

$$Z_{CPE} = \frac{1}{T\,(i2\pi F)^P} \qquad C = T^P R^{\frac{1-P}{P}} \qquad C = \varepsilon_r \varepsilon_0 \frac{A}{D}$$

Figure 3.7 In-situ impedance testing at room temperature A) Nyquist plot B) Bode plot C) CPE equation with magnitude T, phase P, imaginary i and frequency F. D) capacitance for a CPE E) Capacitance equation for a dielectric capacitor with permittivity of free space ε_0, dielectric constant ε_r, cross sectional area A and thickness D

The measured conductivity looks like a mixed type since the lithiated electrodes can be removed from the electrolyte and measured in air but they still have a depressed semi-circle nyquist plot such as the ones shown in figure 3.7. The equations governing the response for a mixed conductor relates the two intercepts of the semicircle to the ionic and electronic resistance as depicted in equation 3.2.

$$Left\ intercept = \frac{R_{Ionic}\, R_{Electronic}}{R_{Ionic} + R_{Electronic}}$$

$$Right\ intercept = R_{Electronic}$$

Equation 3.2 Equations describing the relation for impedance the intercepts with the real axis for a mixed conductor

The values from the modeling including the effective dielectric constant at each voltage step are shown in table 3.4. From table 3.4 the ionic resistance slightly changes with lithiation which results in a change of ionic conductivity with increasing lithiation from 3.6 * 10^{-7} S/cm to 3.9 * 10^{-7} S/cm.

Table 3.4 Data from the modeling to the circuit in figure 3.7 A with the magnitude of the CPE T, Phase parameter of the CPE P, Capacitance of the CPE and effective dielectric constant ε_r

Sample	Mol Li	R Ionic	T	P	R Electronic	Capacitance (F)	ε_r
1.95 V	0.025	128.8	3.42E-06	6.37E-01	9.40E+03	4.81E-07	272
1.83 V	0.287	129.6	3.21E-06	6.43E-01	8.09E+03	4.21E-07	238
1.74 V	0.548	127.6	3.29E-06	6.39E-01	7.75E+03	4.14E-07	234
1.65 V	0.810	128.9	3.74E-06	6.27E-01	4.00E+03	3.09E-07	174
1.56 V	1.071	130.3	4.19E-06	6.17E-01	1.94E+03	2.11E-07	119
1.47 V	1.333	131.6	4.78E-06	6.03E-01	1.11E+03	1.52E-07	86
1.38 V	1.594	136.0	4.91E-06	5.98E-01	7.00E+02	1.08E-07	61
1.27 V	1.856	140.5	4.84E-06	5.93E-01	4.92E+02	7.70E-08	43

Using the equation in figure 3.7 E, the effective dielectric constant of the film at 1 Hz was measured during lithiation. The measured dielectric constant decreases with increasing lithium insertion to a minimum of 43, shown in table 3.4, which is lower than the direction averaged dielectric constant of 77 for orthorhombic Nb_2O_5 [76]. This decrease in dielectric constant suggests that the lithium is slightly distorting the Nb_2O_5 crystal structure.

The larger intercept of the semicircle with the real axis in figure 3.7 correspond with the DC conductivity data shown in figure 3.8. The DC voltage sweeps are ohmic but they are shifted from the origin by the electrode polarization. The curves were shifted back to the origin in figure 3.8 B and the conductivity was calculated by ohm's law. The DC measurements were used for in-situ testing instead of the impedance intercepts because it is easier to compensate for the polarization using the DC measurements.

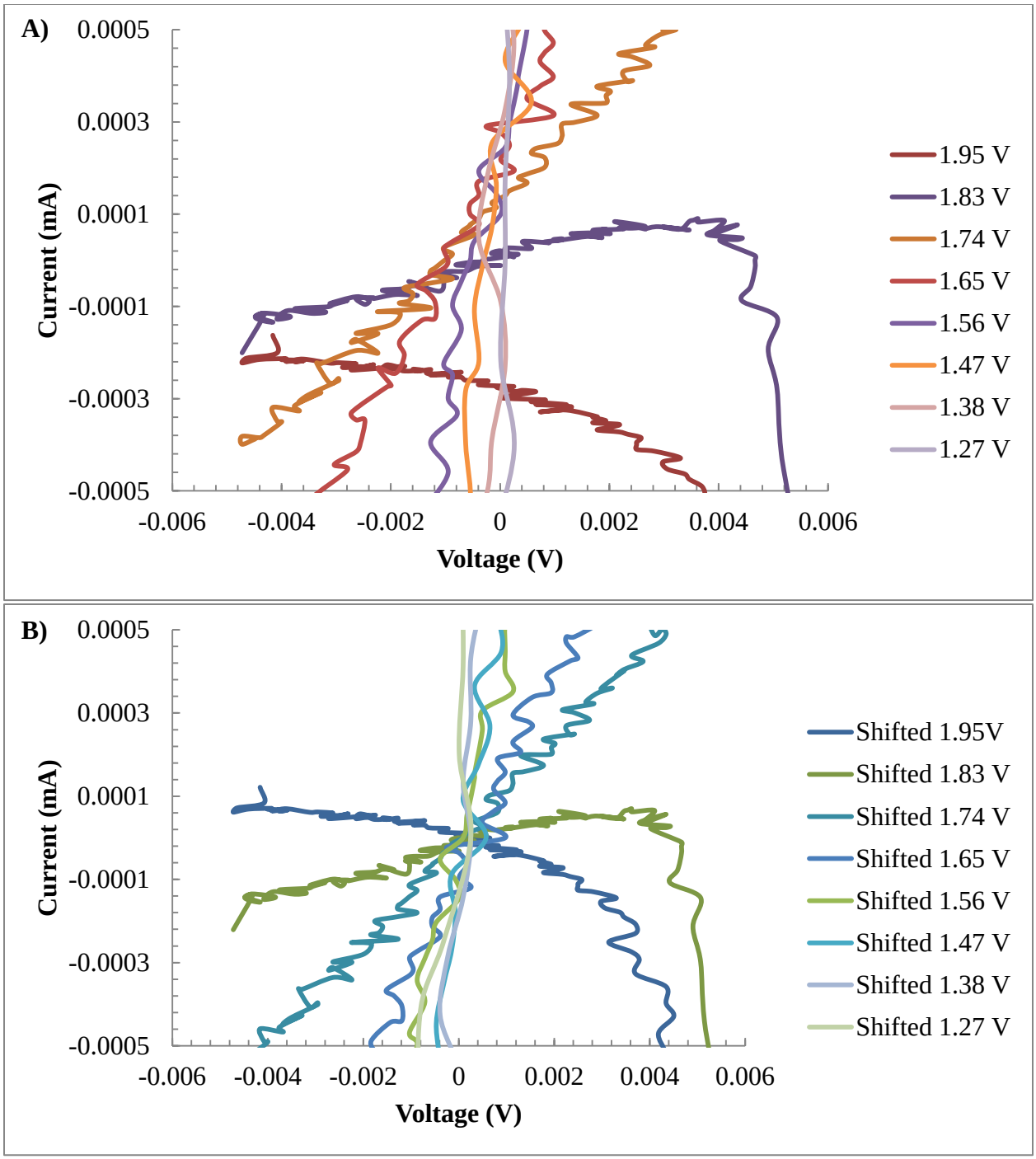

Figure 3.8 In-situ impedance testing at room temperature DC voltage sweeps A) As measured D) After shifting the origin of the DC sweeps

Figure 3.9 shows the change in conductivity for Nb_2O_5 as a function of lithiation at room temperature using the DC sweeps. The conductivity smoothly increases 2 orders of magnitude

with lithium intercalation and the process is reversible with minimal hysteresis. The as prepared sample had a conductivity of $1 * 10^{-11}$ S/cm so even a small addition of lithium greatly improves the sample's electronic conductivity. The electronic conductivity of the fully lithiated Nb_2O_5 is $2.4 * 10^{-7}$ S/cm and this value is consistent with those reported in literature [57]. When considering figure 3.10 and figure 3.5, a capacitor cycled between 1.2 and 1.6 V would have an order of magnitude higher conductivity than a capacitor cycled from 1.6 to 2 V with roughly the same amount of energy being stored in both cases.

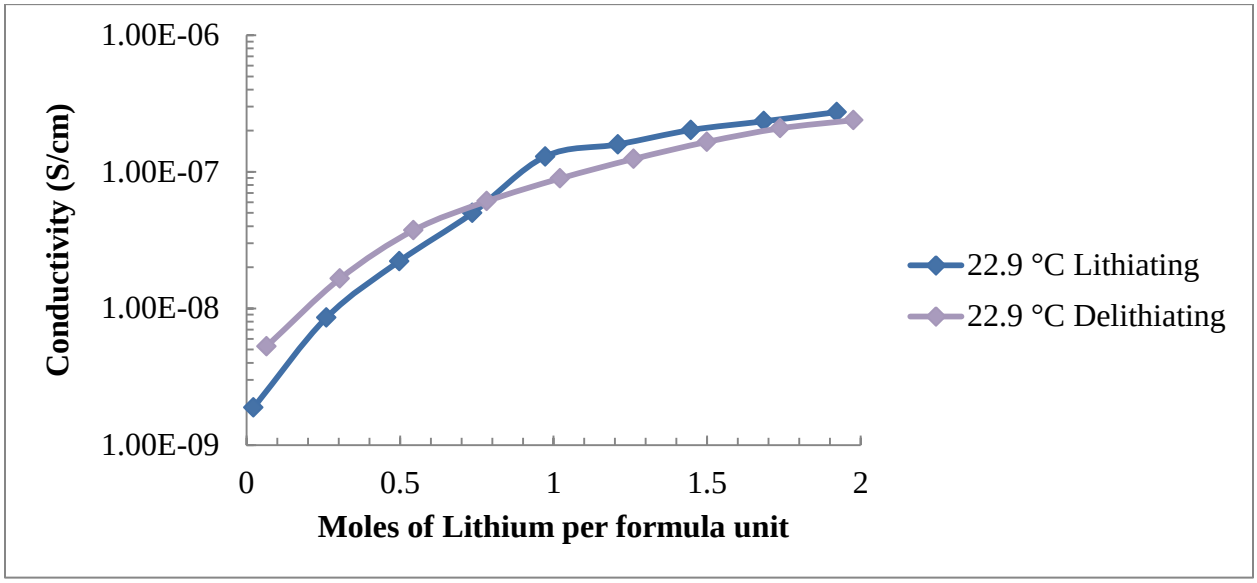

Figure 3.9 Electronic conductivity as a function of lithiation measured by in-situ DC conductivity for sample A at room temperature

Chapter 3.3.3. Elevated Temperature Electrochemical Testing

Measuring the conductivity of sample A at elevated temperatures changed the sample in an irreversible way. As sample A was heated, the conductivity only rises about one order of magnitude during lithiation as shown in figure 3.10. As the temperature increases, the conductivity decreases slightly but this decrease in conductivity remains after allowing the

sample to cool to room temperature. Comparing the two measurements at 22.9 °C, the difference in conductivity suggests that the Nb_2O_5 has undergone a phase change.

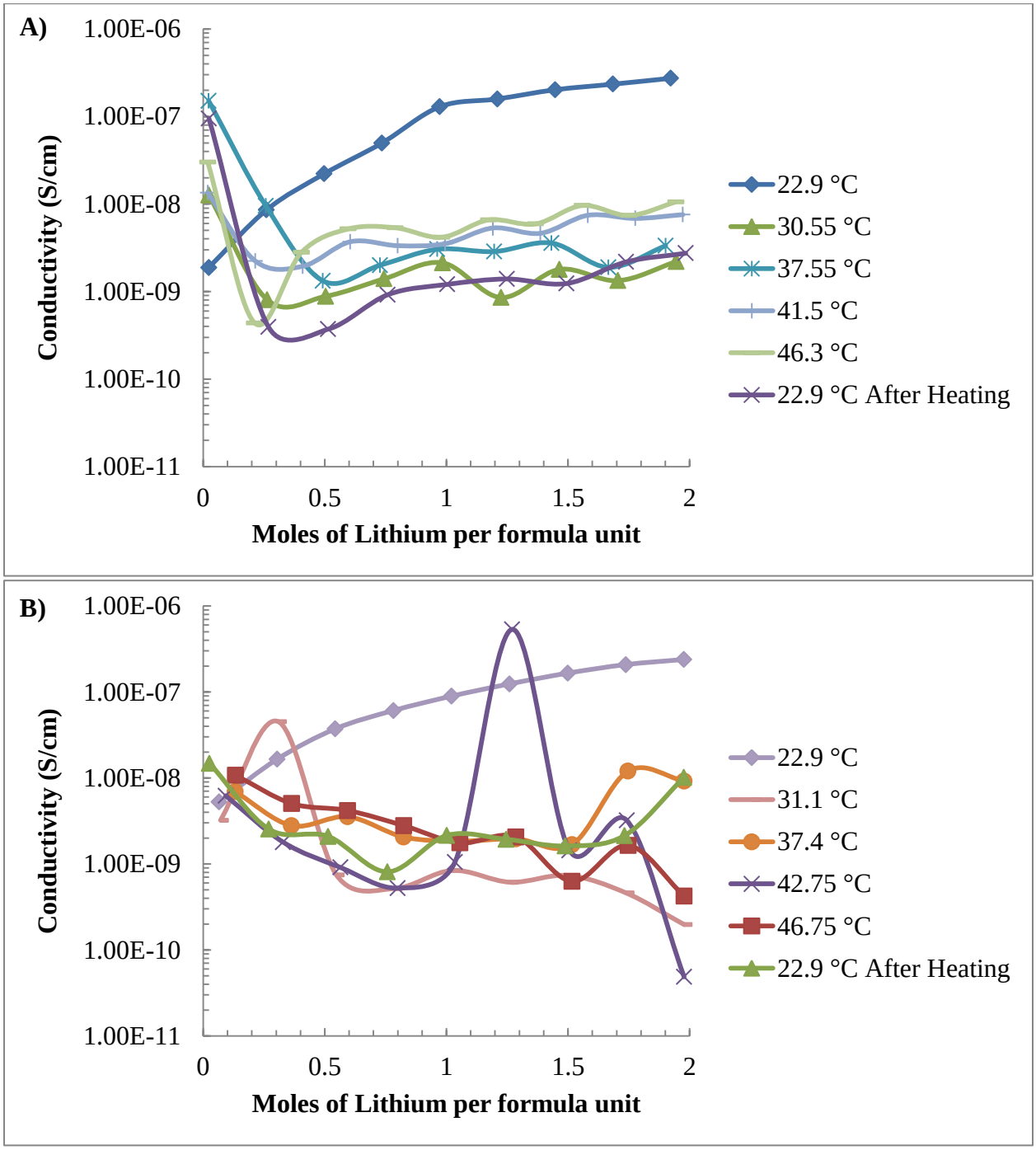

Figure 3.10 In-situ conductivity for sample A measured by DC sweeps during lithium A) Insertion and B) Removal

To determine if the observations from sample A are representative of the material, sample B was tested under the same conditions. It can be seen in figure 3.11 that the conductivity of sample B is also reduced at elevated temperature. There is an order of magnitude increase in conductivity during lithiation, which is consistent with sample A. The initial scan with sample B at 29.2 °C has a discontinuity that could have been caused by the material undergoing a phase change. The scan at 29.2 °C had a slight ramp in temperature from the initial measurement of 28.2 °C at 0.02 moles lithium, to the final measurement at 30.2 °C. Considering the subsequent scans show similar shapes, the phase change likely requires low temperature to occur. After allowing the sample to cool, the conductivity remains low.

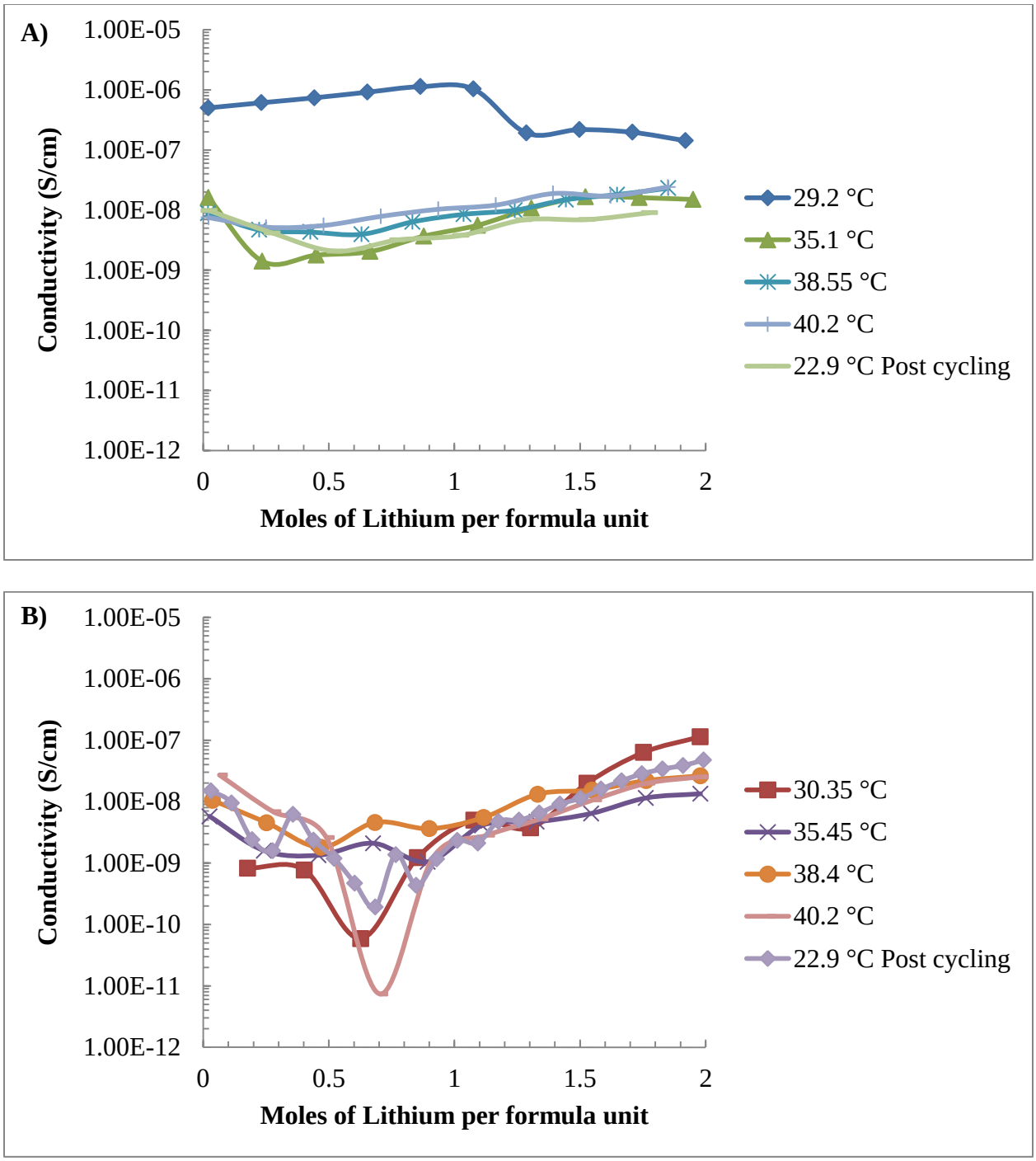

Figure 3.11 In situ conductivity for sample B measured by DC sweeps during lithium A) insertion and B) Removal

After electrochemical cycling, XRD was used to determine if a phase change was occurring after heating the sample to elevated temperature. The spin coated samples are too thin

for XRD so witness pieces with thicker electrodes were tested instead. The results from the XRD are shown in figure 3.12 and the Nb_2O_5 is no longer orthorhombic. Matching with the JCPDS spectra, the sample appears to be a mix of the orthorhombic and tetragonal phases. This phase change supports the observations from cyclic voltammetry and explains why the conductivity changed after heating.

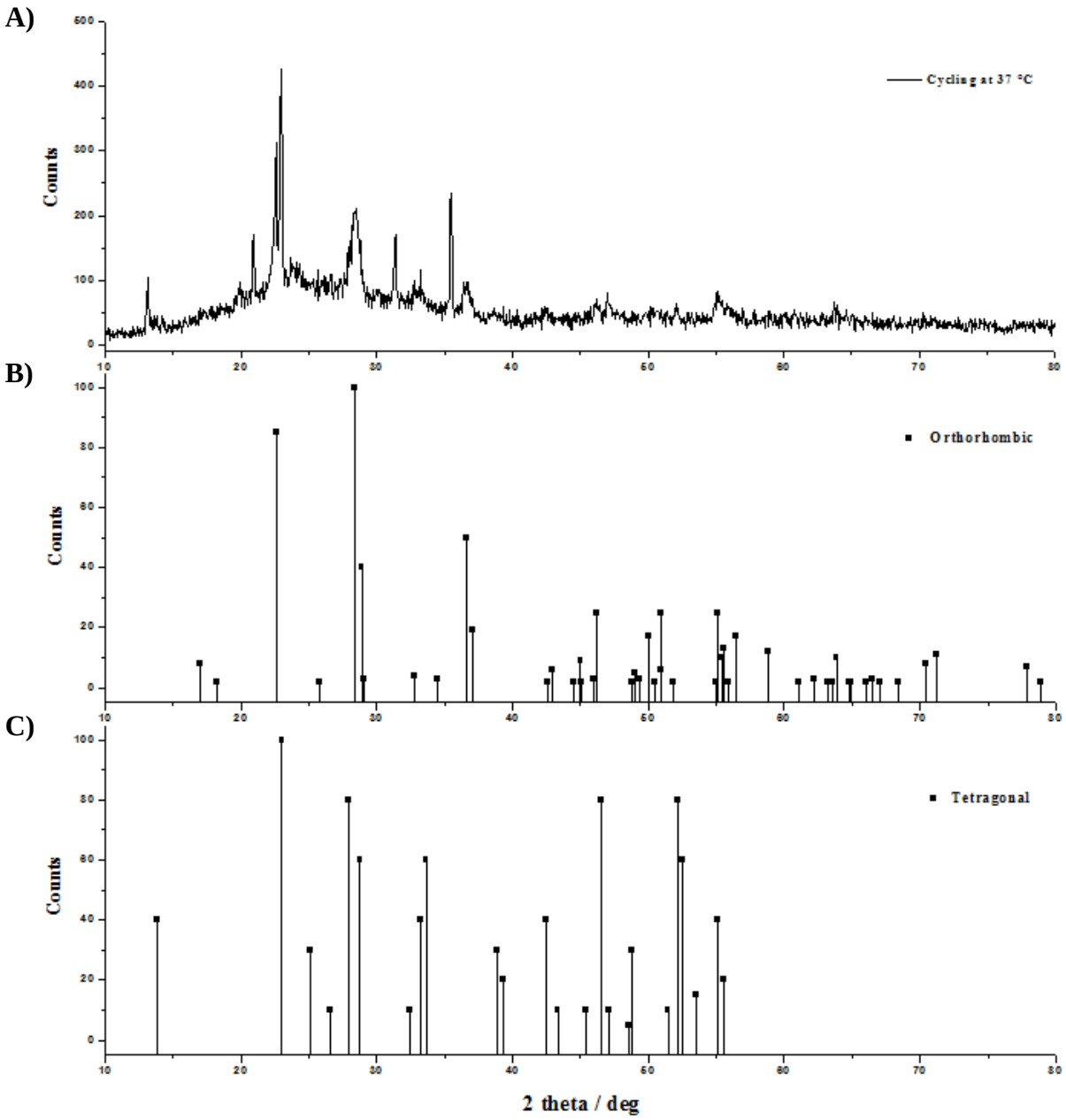

Figure 3.12 A) Powder XRD after cycling and heating B) Orthorhombic phase JCPDS-30-0873 C) Tetragonal phase JCPDS-18-0911 (XRD by Hyungseok (Jimmy) Kim)

Now that the electronic portion of the conductivity has been describe, the focus can be shifted to the ionic contribution. Table 3.5 shows the values of the ionic conductivity at the

extremes of lithiation at different temperatures. From table 3.5, it is apparent that the lithium content does not greatly affect the ionic conductivity. Temperature does seem to have an effect on ionic conductivity but more points would be needed to determine an activation energy.

Table 3.5 Results from modeling for Samples A and B at different states of lithiation and temperature

Sample A	R Ionic	T	P	R Electronic	Ionic Conductivity
Lithiated					
22.9 °C After Heating	440.8	4.11E-06	0.5115	27149	1.13E-07
31.1 °C	109.3	9.70E-06	0.5334	15376	4.57E-07
37.4 °C	298	6.89E-06	0.4364	26796	1.68E-07
42.75 °C	240.1	9.59E-06	0.4089	27661	2.08E-07
46.75 °C	200.4	1.74E-05	0.3714	22462	2.50E-07
Delithiated					
22.9 °C After Heating	441.9	3.49E-06	0.5263	31354	1.13E-07
31.1 °C	112.6	6.15E-06	0.5772	23530	4.44E-07
37.4 °C	249.6	8.25E-06	0.4179	36896	2.00E-07
42.75 °C	229.5	9.90E-06	0.4077	40795	2.18E-07
46.75 °C	194	1.61E-05	0.3795	26850	2.58E-07
Sample B	R Ionic	T	P	R Electronic	Ionic Conductivity
Lithiated					
22.9 °C Post Cycling	125.5	7.78E-06	0.536	1404	5.31E-07
30.35 °C	76.28	7.97E-06	0.5424	638.6	8.74E-07
35.45 °C	67.93	1.00E-05	0.5297	4034	9.81E-07
38.4 °C	68.92	1.10E-05	0.5323	1902	9.67E-07
40.2 °C	68.42	1.23E-05	0.5288	1881	9.74E-07
Delithiated					
22.9 °C Post Cycling	159.9	5.67E-06	0.567	28273	4.17E-07
30.35 °C	69.04	4.90E-06	0.5769	31259	9.66E-07
35.45 °C	64.05	6.34E-06	0.5689	15250	1.04E-06
38.4 °C	62.8	8.31E-06	0.5638	11282	1.06E-06
40.2 °C	62.41	1.09E-05	0.5423	9471	1.07E-06

Chapter 3.4. Conclusion

In-situ impedance studies of Nb_2O_5 have demonstrated that orthorhombic Nb_2O_5 increases two order of magnitude with the slightest addition of lithium and then two additional orders when fully lithiated. Heating T-Nb_2O_5 in the presence of lithium is a new route to a mixed orthorhombic and tetragonal phase. These increases in conductivity explain why the semiconducting Nb_2O_5 can display high rate capability and define the regions of maximum conductivity for the material. This impedance study demonstrates an approach for characterizing transition metal oxide pseudocapacitors and bringing an understanding into their electrochemical performance.

Chapter 4. Electrochemical Characterization of Sub Nanometer Pinholes in Thin Film Solid Electrolytes

Chapter 4.1. Introduction

Batteries are the cornerstone of modern technology. They are ubiquitous in electrical devices and as electronics become smaller, the demands on their power capability continue to increase. Batteries store energy by electrochemical reactions occurring within the cathode and anode, which are immersed in electrolyte and in most commercial devices separated by a porous membrane, often called a separator. Batteries with thick electrodes are often limited in their charge storage by the rate of ion diffusion through the bulk of the electrodes. Minimizing the diffusion distance of the ions improves the power of the battery, which is why thin film batteries exhibit high power. Historically, the tradeoff to high power has been thin electrodes and therefore low energy densities for batteries that operate in small dimensions, such as a microbattery.

An engineering approach to develop microbatteries with both high power and high energy is to use electrodes with three dimensional (3D) architecture. A recent review documents a few of the approaches [77] which typically involve redistributing the mass of the electrodes into networks to increase the surface area of the electrodes while maintaining high mass loadings. Figure 4.1 shows an example architecture and the result from 3D architectures is improved rate capability [78–80]. A limitation with some of the proposed designs is that the cathode and anode are greatly separated by electrolyte, which lowers the volumetric energy density. More volume efficient designs reduce the distance between the cathode and anode but as this distance shrinks, the need for a conformal solid electrolyte to prevent electrical shorts increases. This solid

electrolyte needs to be ionically conducting, electronically insulating and conformal over the rough battery electrodes materials. With these conditions, there is need for a method to detect and characterize pinholes in conformal solid electrolyte as a prelude to assembling a full 3D microbattery.

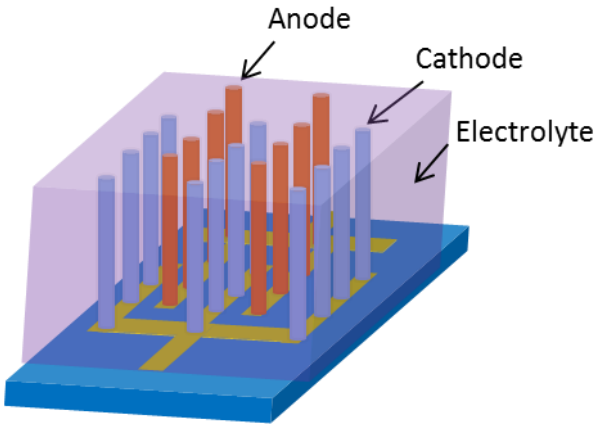

Figure 4.1 Simple fabrication electrode configuration for 3D microbattery

Solid electrolytes are ideal for preventing electrical shorts because they are often made from oxides or polymers with intrinsically low electronic conductivities. While their properties make them ideal for reducing leakage current, solid electrolytes also have much low ionic conductivities, many in the range of ~ 10^{-6} S/cm [25]. In contrast, the common lithium ion battery electrolytes such as 1 M $LiPF_6$ in 1:1 volume ratio of ethylene carbonate to 1,2-dimethoxyethane is 1.6 * 10^{-2} S/cm [20]. In order to maintain the rate capability of the microbattery the thickness of the solid electrolyte needs to be minimized.

There are many routes to deposit solid electrolytes but only a few methods are conformal on high aspect ratio structures. Common methods of depositing solid electrolytes include magnetron sputtering [81], and pulse laser deposition [82] but these routes are line of sight techniques so they will not evenly coat 3D structures. To deposit conformal coatings, the growth

mechanism must be self-limiting. Two promising gas phase methods that can coat high aspect ratio structures are initiated chemical vapor deposition (iCVD) [83] and atomic layer deposition (ALD) [84].

ALD and iCVD allow for control of both the composition and growth conditions of the deposited film. ALD is performed in a vacuum chamber equipped with multiple precursor gas lines. Each precursor cycle is followed by an oxidant cycle, typically water or ozone, and this process is repeated to control the composition and thickness of the depositing film.

ALD is often used to deposit oxides such as Al_2O_3, ZrO_2 and HfO_2 whose low electronic conductivities are suitable for solid electrolytes [85]. However these oxides also have low ionic conductivities. It is necessary, therefore, to identify systems which can provide high ionic conductivity because of fast ion transport through crystallographic features. One such system is the lithium aluminosilicate beta eucryptite phase (LASO) whose open channels enable Li^+ ion transport [86]. LASO has a large ionic conductivity of 10^{-5} S/cm at room temperature [87] which makes it an appropriate choice for a solid electrolyte. The amorphous lithium aluminosilicate can be crystalized into LASO by rapid thermal annealing (RTA) to minimize atomic diffusion in the film.

An alternate approach to the inorganic ALD films are organic polymer films made by iCVD. Traditional polymer films offer the advantages of low cost and convenient fabrication but they are often made using solution phase chemistry. Solutions are problematic when coating small structures because the drying solvent can de-wet the surface leaving gaps in the film.

ICVD combines chemical vapor phase deposition with the high growth rates of polymer techniques. The first step in iCVD is for monomer and initiator vapor to be released into a vacuum chamber. The monomer adsorbs onto the surface of the samples and the initiator is

thermally cleaved into free radicals that then polymerize with the surface adsorbed monomer [83]. This approach allows for conformal coatings on high aspect ratio surfaces [88] and impressive growth rates 10-100 nanometers per minute. The polymers are not intrinsically ion conductors but ionically conducting salts, such as lithium, can be absorbed into polymer films by soaking the films in electrolyte salt solutions [89].

Gas phase techniques still have the possibility of pinholes, nanometer sized pores, where electrical shorts can occur. There are methods for detecting and characterizing pinholes in 2D films such as using spectroscopic ellipsometry [90, 91] and the decay of positronium [92]. Ellipsometry focuses on the change in film thickness as chemical vapors are absorbed by pores in the film. Since ellipsometry uses a laser, the film has to be flat for an accurate measurement. Positronium decay monitors the decay of the triplet state of positronium. The triplet state's decay rate is slowed by the local dielectric constant, so larger pores decay faster than smaller pores. The advantage of the technique is that through and blind pores can be measured. While positronium decay might be useful for measuring 3D structures, the technique would not be surface sensitive, which is necessary for characterizing the solid electrolyte and not the pores in the coated battery electrode.

Electrochemical techniques are an alternative to spectroscopic techniques for detecting and characterizing pinholes. There have been reports of using the electrochemistry of redox molecules to probe for pinholes in self-assembled monolayers (SAM) [93]. When redox molecules such as ferrocene are in contact with an electrically conducting surface, they can be electrochemically oxidized and reduced at specific potentials, which appear as peaks in the current during cyclic voltammetry. These peak currents are proportional to the area of the electronically conducting surface as indicated by the Randles-Sevcik equation shown in figure

4.2 A. As the surface is coated, the peak current will decrease and this reduction in current can be used to quantitatively determine the coverage of the solid electrolyte on the electrode.

A) **B)**

$$\text{Peak Current} = 0.4463nF\left(\frac{nFD}{RT}\right)^{0.5} AC_0 v^{0.5} \qquad D = \frac{k_B T}{6 \pi \eta r}$$

Figure 4.2 A) Randles-Sevcik equation used to relate the peak current in the cyclic voltammetry to the diffusivity of the redox molecule. B) Stokes-Einstein equation that relates the diffusivity to the redox molecule radius

The material parameters in figure 4.2 are the following: the number of electrons in the redox process n, Faraday's constant F, diffusivity D, ideal gas constant R, temperature T, submerged electrode area A, redox molecule concentration C_0, sweep rate υ. Boltzmann's constant K_b, viscosity of the electrolyte η and radius of the redox molecule r.

Crooks et al developed the methodology for probing SAMs with redox molecules in aqueous systems. A library of redox molecules was characterized and their relevant parameters such as diameter were measured. Molecules of different sizes were then used to probe the surface with the assumption that molecules larger than the pinhole diameter do not interact with the exposed surface. By comparing the results from the different sized molecules, a distribution of pinholes in the SAM can be inferred.

This procedure can be adapted for non-aqueous systems such as propylene carbonate (PC) and acetonitrile (ACN), by measuring the size of the redox molecule in liquid electrolytes compatible with the solid electrolyte deposited by ALD and iCVD. The diameter of the redox molecule can be measured by performing cyclic voltammetry on an electrode of known area then

using the Stokes-Einstein equation from figure 4.2 B along with the Randles-Sevcik equation. The peak current in the Randles-Sevcik equation refers to the peak oxidation current during cyclic voltammetry. Metallocene redox molecules including ferrocene [94], ferrocenium [95], cobaltocene [96], cobaltocenium [97] and decamethyl ferrocene [98] are of interest since they are well studied in literature and are soluble in ACN and PC.

Along with the selection of the redox couples, the electrode kinetics should be considered for these experiments. The literature approach is to use microelectrodes made of a noble metal or glassy carbon to determine the diffusivity of the redox molecule. The stability of noble metals in many electrolytes minimizes chemical reactions other than the metallocenes. Microelectrodes are made by encasing a noble metal wire into an insulating medium, such as glass, to produce a working electrode with dimensions of a few square microns. These electrodes have many advantages over macro sized centimeter squared electrodes including responding faster to changes in voltage and having less distortion due to double layer capacitance and ohmic drop [99].

While microelectrodes are useful for kinetic studies they are not analogous to the electrodes for the microbatteries. Since the current will drop as the electrodes are coated, it is advantageous to coat larger electrodes to improve measurement signal. Larger electrodes also offer better statistics of the coating coverage as well as meaningful kinetic data due to work by Nicholson [100]. . Large electrodes are prone to slower kinetics and larger overpotentials, the voltage in excess of the voltage determined by thermodynamics for a reaction to occur. A way to quantify the difficulty for the electrons to transfer from the redox molecule to the current collector is the heterogeneous rate constant shown in figure 4.3. Pioneering work done by

Nicholson relates the rate constant to the voltage separation by using the Psi parameter shown in figure 4.3 C [100].

A)

$$\psi = \gamma^{a} k_s \Big/ \sqrt{n\pi F v D_o / RT}$$

B)

$$\gamma = (D_o / D_R)^{1/2}$$

C)

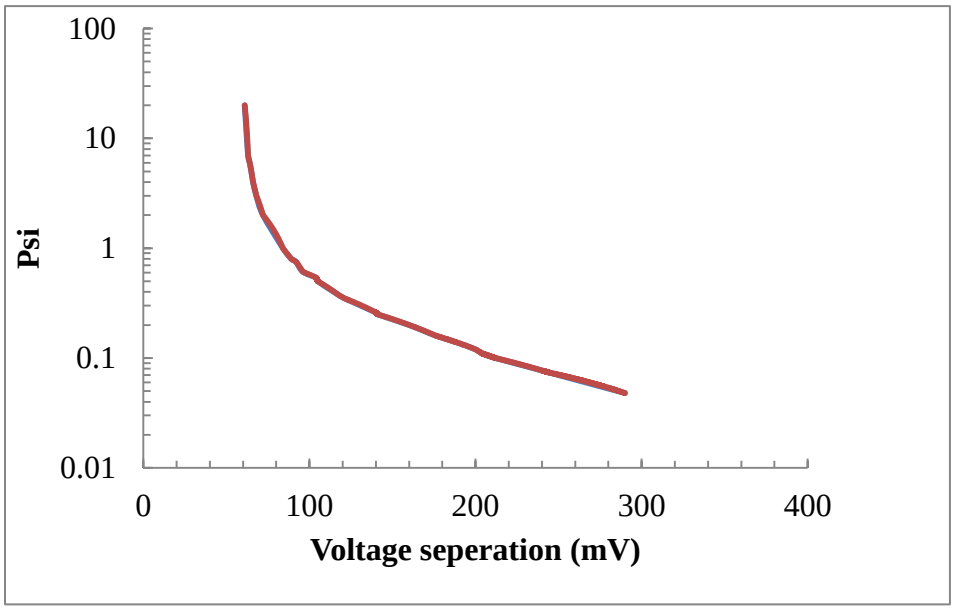

Figure 4.3 A) Heterogeneous rate constant K_s related to the diffusivities for the oxidation and reduction reactions. The variables have their same meaning from figure 4.2 with the addition of Charge transfer coefficient α B) Gamma parameter for the oxidation diffusivity D_o and reduction diffusivities D_R C) Psi parameter correlated to voltage separation [101]

Along with characterization of the pinholes by the redox molecules, impedance spectroscopy can be used to measure the conductivity of the films. For films with sub micron thickness, hanging mercury drop electrodes are a useful technique for making contact to the film. Mercury provides an electrical contact and is less likely to damage the films than deposited metal contacts or pressing on a probe tip [102]. Impedance spectroscopy is a powerful technique that probes the electrical properties with small voltage perturbation, which allows for the distinction between ionic and electronic transport.

Combining the redox molecule analysis with impedance spectroscopy allows for the characterization of ALD and iCVD solid electrolytes for 3D microbatteries. The criteria for characterization are coverage of the surface, pinhole size distribution, heterogeneous electron transfer coefficient and ionic conductivity of the solid electrolyte.

Chapter 4.2. Experimental

To fabricate a carbon electrode for the 3D battery, an aqueous carbon slurry was made by a combination of magnetic stirring and vortex mixing. The slurry composition is the following in weight percent: 83% mesocarbon micro beads (MCMB) 8% KS-4 natural graphite 2% Ketjen black 7% carboxymethyl cellulose (CMC). Once the slurry was mixed, it was drop cast onto stainless steel that had been cleaned by oxygen plasma and allowed to dry overnight. The plasma cleaning was performed for 5 minutes at 1 torr of oxygen. The mass of the deposited slurry was measured using a microbalance and the surface area of the slurry is approximately 25 m^2/g active material based on the constituent components data sheets and literature values [103].

Chapter 4.2.1. Film Fabrication

The $Li_xAl_ySi_zO$ thin films are grown by thermal ALD in a hot wall reactor at 290°C in the Jane Chang lab at UCLA. The organometallic precursors used as the source for Li, Al and Si respectively are the following: lithium t-butoxide, trimethylaluminum, and tetraethyl orthosilane. Deionized water is used as the oxidant. The LASO films are synthesized with a sequence of a(Li-O)- b(Al-O)-c(Si-O) where a, b, c represent the number of local ALD cycles for each constituent oxide. Quantitative elemental analysis was performed at the synchrotron photoelectron spectroscopy (PES) at the Stanford Synchrotron Radiation Lightsource (SSRL) with a photon

energy of 140 eV to check the crystal phase of the film deposited with a=6, b=10, c=4 after post-deposition RTA in N_2 at 500–900°C for 90 seconds. The LASO is grown to thicknesses from 5 to 12 nm on the carbon films as well as on indium doped tin oxide (ITO) thermally sputtered on quartz.

The iCVD is deposited in a custom built chamber equipped with gas inlets for the initiator, tert-butyl peroxide and the monomers, 1,3,5,7- Tetravinyltetramethylcyclotetrasiloxane (V4D4) and (trivinyltrimethylcyclotrisiloxane) (V3D3) in the Karen Gleason lab at MIT. The monomer is heated in a partially evacuated chamber and a monolayer adsorbs onto the substrate that is maintained at room temperature by a cooler. The films grow when the heated initiator breaks into free radicals that then polymerize with the monomer to form PV4D4 and PV3D3 from the monomers V4D4 and V3D3 respectively. Film growth is measured by in-situ interferometer measurements and the substrate ITO is the same as for the LASO films.

The PV4D4 and PV3D3 films were deposited at 20, 40 and 100 nm on ITO and carbon films. The iCVD films are lithiated by soaking the films for 3 days in 1M solution of lithium perchlorate in PC. After the soak, the films were rinsed in neat PC to remove excess salt then dried with an air gun. The samples were then heated at 130°C under vacuum for 14 hours before being shipped across country for testing.

Chapter 4.2.2. Pinhole Testing

All of the chemicals for the redox molecules used in pinhole testing(ferrocene, ferrocenium, cobaltocene, cobaltocenium and decamethyl ferrocene) were purchased from Sigma Aldrich. The redox molecules are heat sensitive so they were vacuum dried before bringing them into an argon filled VAC glovebox. Solutions containing 0.9259 mM redox molecule and 100

mM tetrabutylammonium tetrafluoroborate (TBATFB) were mixed by magnetic stirring overnight in anhydrous ACN and PC.

Platinum foil from Alfa Aesar was used as the counter and pseudo reference electrodes for all electrochemical experiments. The initial tests to determine the diffusivity were conducted using teflon tape masked platinum foil electrodes with 2 cm^2 submerged in electrolyte. ITO samples were also masked with teflon tape and used as a working electrode with 1 cm^2 exposed to the solution.

Cyclic voltammetry was performed using a BioLogic VMP3 potentiostat connected to a 3 electrode cell at scan rates of 1-1000 mV/s. The platinum foils were cleaned by ultrasonication in acetone and isopropanol after each scan. Fresh solution was used to test each redox system with each working electrode.

Chapter 4.2.3. Impedance Testing

The ionic conductivity of the films was measured in the glovebox using electrochemical impedance spectroscopy with hanging mercury drop electrodes. Mercury is suspended from plastic syringes to dispense small hanging drops of electronic grade mercury purchased from Alfa Aesar. The drops are lowered onto the surface using a vernier drive allowing for repeatable contact to the film and the substrate shown schematically in figure 4.4. The mercury drop contact area to the film is 0.5 cm^2. The impedance measurements were taken using a Solartron 1287 and 1252a potentiostat and function generator respectively. Each sample is measured multiple times and the average values are used in the calculation of conductivity to improve accuracy.

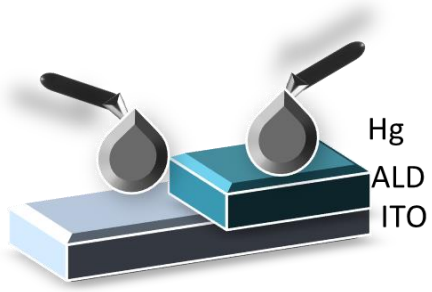

Figure 4.4 Diagram of hanging mercury drop electrode for measuring the impedance of the solid electrolytes

Chapter 4.3. Results and Discussion

Chapter 4.3.1. Redox library

The redox molecules were tested using platinum working electrodes to facilitate comparison with literature values. Initially, slower sweep rates for cyclic voltammetry were applied when testing ferrocene in ACN, however, a film was found to be depositing on the electrodes [Appendix 2]. This presence of the film shifted the voltage at which the peak currents occurred by over 300 mVs between the first cycle and the subsequent cycles. The film also changed the magnitude of the peak currents by slightly diminishing the oxidation current (positive peak) and greatly reducing the reduction current (negative peak). Based on the voltage where the peak in current occurred during the cyclic voltammetry and comparing to literature sources, the film was determined to be ferrocenium [104]. By scanning a fresh electrode at higher rates the shifts in voltage were not observed and no film growth was present as determined by a microbalance. Figure 4.5 shows an example of the cyclic voltammetry at multiple sweep rates and the details of peak position and peak current from each scan rate can be found in appendix 2. Figure 4.5 represents a good measurement since the peak in current only

slightly shifts in voltage with increasing sweep rate. Fresh solutions were used for each electrode since the redox molecules were observed to settle over the course of a day.

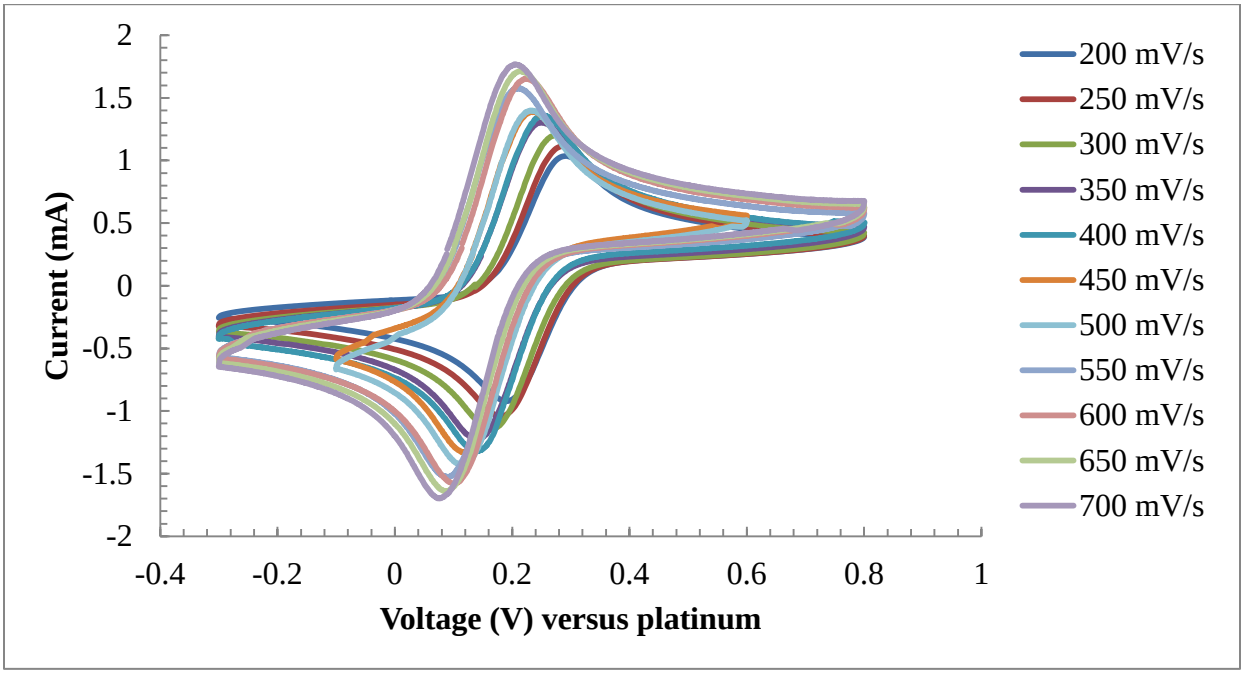

Figure 4.5 Cyclic voltammetry of decamethyl ferrocene on platinum electrode in ACN from 200-700 mV/s

Each redox system was tested and there are trends for the measured diffusivities, rate constants and diameters depending on the solvent and the electrode. The testing with platinum electrodes showed higher diffusivity than with ITO electrodes due to the faster electron transfer rate constant for platinum than ITO. The testing in ACN had higher diffusivities than in PC due to the difference in viscosity. The following paragraphs focus on the differences in size of the redox molecules in the tested systems.

As a verification of the procedure, the first tests were performed on platinum electrodes in ACN and the data is shown in table 4.1 along with reference values from literature. Oxidation diffusivity (D_o) and Reduction diffusivity (D_R) refer to the diffusivities calculated from the equations in figure 4.2 using the oxidation and reduction currents respectively. Diameters are

calculated from the oxidation diffusivity and the Stokes-Einstein equation in figure 4.2 following the literature approach [105]. There is good agreement between the measured and reported values from literature even though most were measured using microelectrodes. This good agreement with literature verifies the procedure. Of the tested molecules, ferrocene is the smallest redox couple and decamethyl ferrocene is the largest.

Table 4.1 Redox systems with ACN electrolyte and platinum working electrode

Redox Couple	K_s (cm/s)	D_O (m2/s)	Diameter (m)	D_R (m2/s)
Ferrocene	1.59E-2	2.77E-09	4.50E-10	2.53E-09
	(2.31E-2) [101]	(2.4E-9) [106]		
Cobaltocenium	7.91E-3	2.38E-09	5.25E-10	2.26E-09
		(1.8E-9) [97]		
Cobaltocene	9.74E-3	1.98E-09	6.31E-10	1.68E-09
		(2.3 E -9) [97]		
Ferrocenium	1.22E-2	1.86E-09	6.70E-10	2.16E-09
		(2.36 E-9) [95]		
Decamethyl F.	1.07E-2	1.45E-09	8.64E-10	1.60E-09
		(1.8E-9) [98]		

Table 4.2 shows the results from ACN electrolytes with ITO electrodes. Comparing table 4.2 to table 4.1, the relative sizes of the redox molecule are different when testing on ITO than on platinum. This observation is consistent with the literature that the composition of the electrode surface influences the measured currents [107]. Platinum is the accepted method for calculating redox molecule size and ITO is an ideal substrate for testing the solid electrolyte ability to coat flat films.

Table 4.2 Redox system with ACN electrolyte and ITO working electrodes

Redox Couple	K_s (cm/s)	D_O (m2/s)	Diameter (m)	D_R (m2/s)
Ferrocene	5.47E-3	2.35E-09	5.31E-10	2.50E-09
Ferrocenium	1.41E-3	5.71E-10	2.19E-09	1.20E-09
Decamethyl F.	8.14E-4	5.56E-10	2.25E-09	5.00E-10
Cobaltocenium	1.46E-3	5.55E-10	2.25E-09	6.41E-10
Cobaltocene	7.08E-4	4.40E-10	2.84E-09	3.68E-10

Tables 4.3 and 4.4 show the results from the testing in PC with platinum and ITO electrodes respectively. Decamethyl ferrocene is again the largest redox molecule and ferrocenium is now the smallest on the platinum electrodes in table 4.3. There are fewer reference values to compare the results in PC with but the trend in redox molecule size is reasonable considering the chemical formulas.

Table 4.3 Redox system with PC electrolyte and platinum working electrodes

Redox Couple	K_s (cm/s)	D_O (m2/s)	Diameter (m)	D_R (m2/s)
Ferrocenium	4.67E-3	2.74E-10	6.24E-10	3.00E-10
Cobaltocene	2.11E-3	2.38E-10	7.18E-10	2.11E-10
Ferrocene	1.95E-3	2.36E-10 (4.4E-10) [106]	7.27-10	2.51E-10
Cobaltocenium	2.29E-3	2.21E-10	7.75E-10	2.20E-10
Decamethyl F.	1.66E-3	1.85E-10	9.27E-10	1.67E-10

When considering each electrode material, there is a trend that the diffusivity is one order of magnitude higher in ACN than in PC. This trend can be seen when comparing table 4.1 to table 4.2 and then again in table 4.3 and table 4.4. The diffusivities are lower in PC because of its higher viscosity than ACN. The values are 2.5 cP and 0.343 cP respectively [96]. Another trend from tables 4.1 through table 4.4 is that the heterogeneous rate constant is higher for the platinum than the ITO electrodes. Rate constants greater than 0.02 cm/s are considered quasi reversible [108] and the measured values in tables 4.1 and, to a lesser extent, table 4.3 are close to that value.

Table 4.4 Redox system with PC electrolyte and ITO working electrodes

Redox Couple	K_s (cm/s)	D_O (m2/s)	Diameter (m)	D_R (m2/s)
Cobaltocene	2.66E-4	6.90E-11	2.48E-09	4.66E-11
Ferrocene	1.34E-4	5.60E-11	3.06E-09	5.42E-11
Cobaltocenium	2.66E-4	4.93E-11	3.48E-09	4.98E-11
Ferrocenium	2.93E-4	5.11E-11	3.35E-09	9.38E-11
Decamethyl F.	2.21E-4	3.80E-11	4.51E-09	4.05E-11

Chapter 4.3.2. Pinhole Testing on LASO coated ITO and carbon

Data from cyclic voltammetry of the LASO coated samples were used with the diffusivities from table 4.2 and the equations in figure 4.2 to characterize the coated samples. The uncoated area was determined by using the peak currents from cyclic voltammetry testing and the Randles-Sevcik equation with the measured diffusivity from table 4.2 for each of the tested redox molecules. Cobaltocenium and decamethyl ferrocene were used to test the pinhole distribution because of their difference in size as seen in table 4.2. Figure 4.6 shows the samples

coated with LASO have lower peak currents than the uncoated sample, which implies that most of the surface is coated. The coverage is nearly complete for sample without RTA, but the crystalline LASO films show a large increase in pinhole concentration. These results suggest that the RTA may be creating cracks in the coating or causing island growth during crystallization that is increasing the pinhole density.

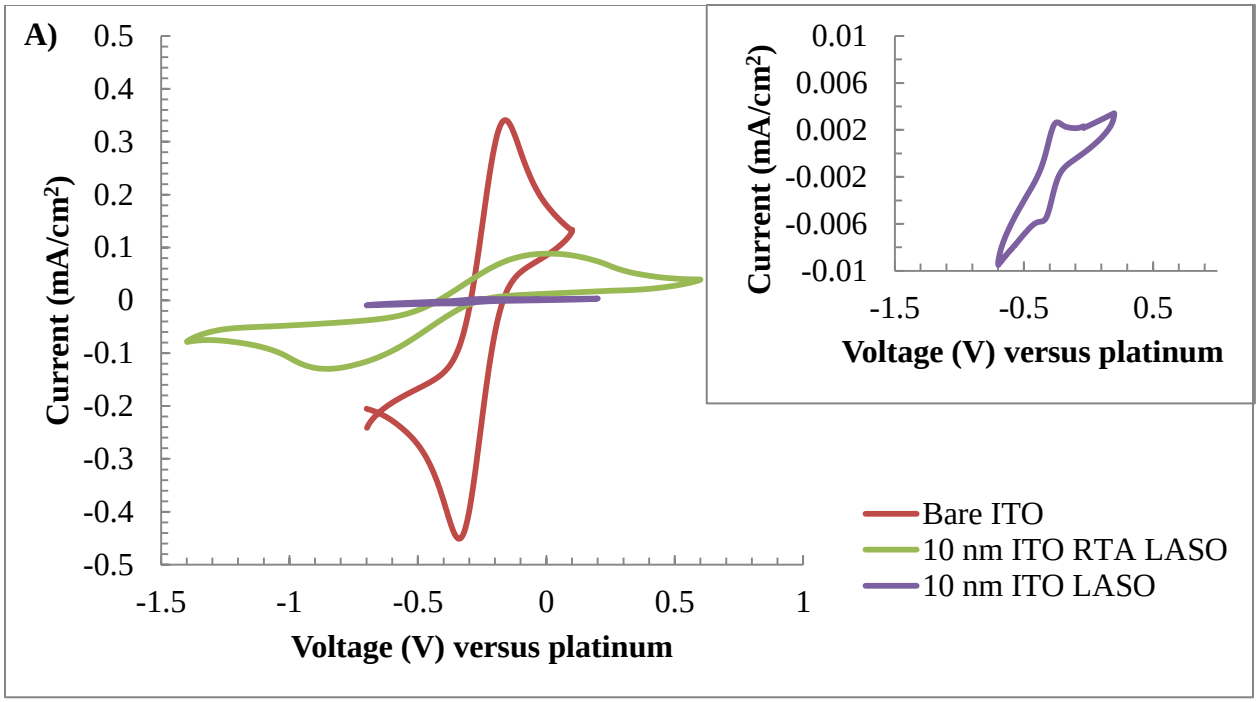

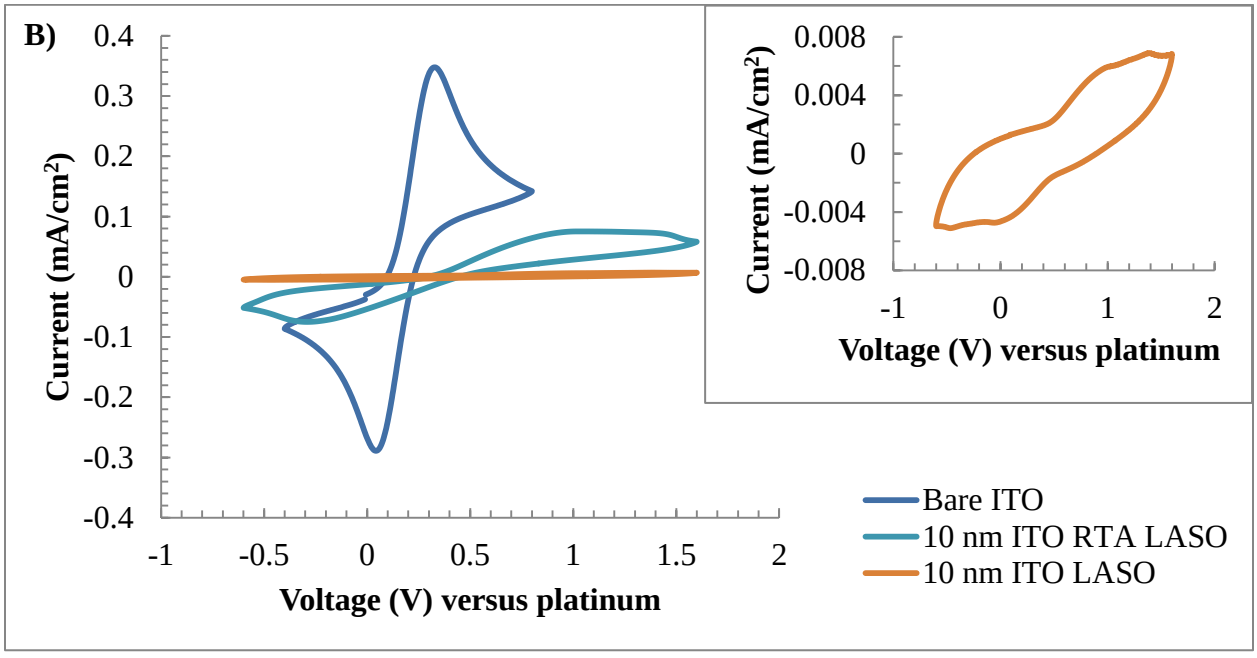

Figure 4.6 Pinhole testing using cyclic voltammetry at 200 mV/s in ACN with A) Cobaltocenium and B) Decamethyl Ferrocene, for coated and uncoated ITO with and without RTA. The insets show the LASO coated ITO films in more detail

The testing on carbon films is of considerable interest because carbon is an electrode for lithium ion microbatteries. Carbon films are much rougher than ITO so they are more difficult to coat. Figure 4.7 shows the large reduction in current for the coated samples compared to the uncoated samples. The currents in figure 4.7 are normalized to the mass of the carbon films, which are 0.447 mg and 3.142 mg for the uncoated and coated sample respectively.

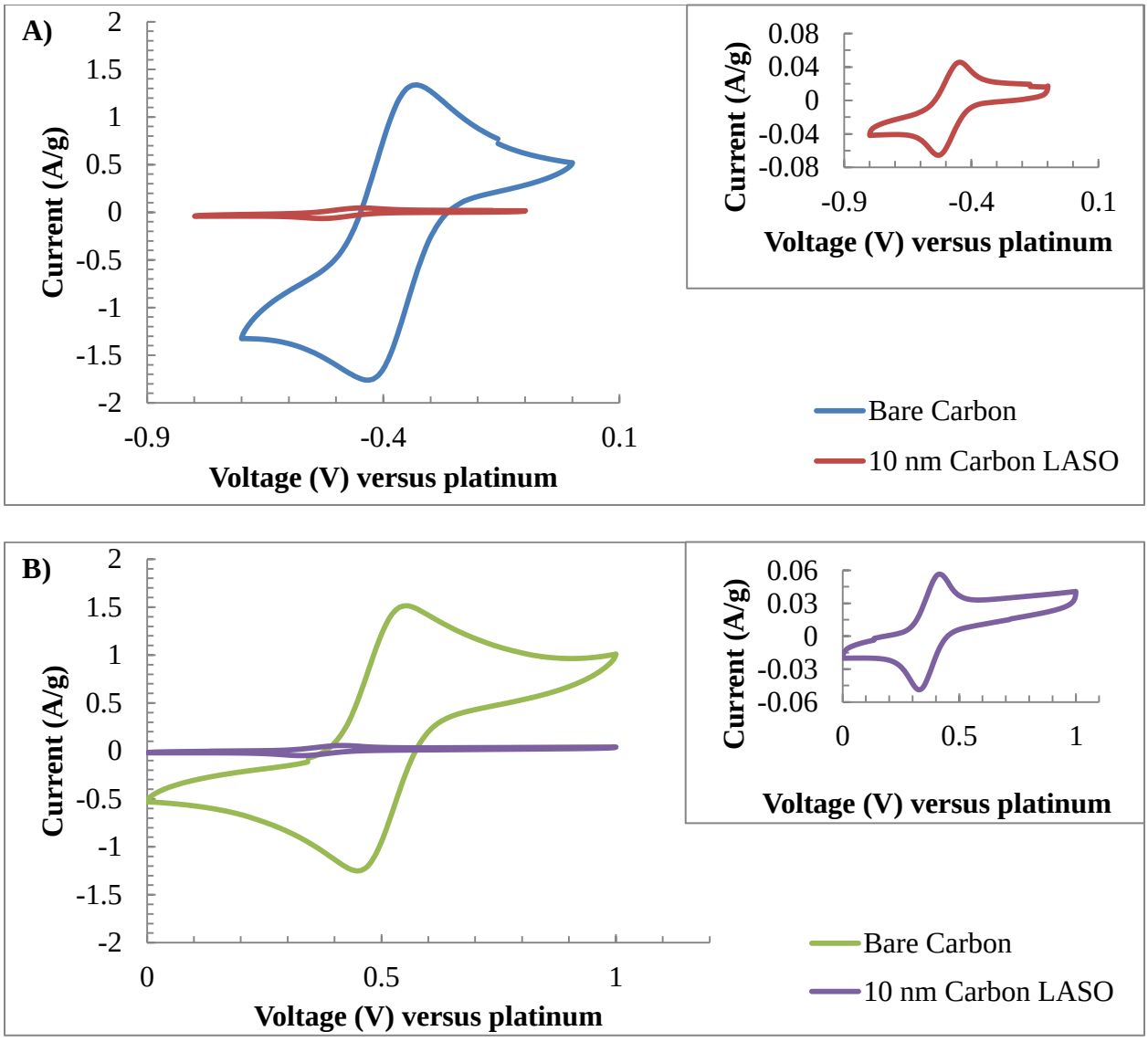

Figure 4.7 LASO coated and uncoated carbon films measured in ACN at 200 mV/s with A) Cobaltocenium and B) Decamethyl Ferrocene redox molecules

Table 4.5 presents a summary of the LASO coated samples using the data from figure 4.6 and figure 4.7 as well as the equations from figure 4.2 and figure 4.3. The parameters for Pinhole Ox is calculated in a two part procedure. First the slope of the oxidation peak current from the cyclic voltammetry as a function of sweep rate was determined for the coated and uncoated samples. Next, the slope from the coated sample was divided by the slope from the control sample to give the percentage shown in table 4.5. Pinhole Red is calculated in a similar manner but with the reduction currents. One trend for the LASO coated films is the reduction of the heterogeneous rate constant, which is beneficial for coated films since fast electron transport leads to higher leakage current. The coverage of LASO on ITO and Carbon is very similar for both redox molecules, which implies that the pinholes are larger than both redox molecules.

Table 4.5 Summary of ALD coatings of substrates and the associated heterogeneous rate constant from testing in ACN

Substrate	Redox	Coating	Pinhole Ox	Pinhole Red	K_s (cm/s)
ITO	Cobaltocenium	10 nm LASO	0.06%	0.04%	1.50E-4
ITO	Decamethyl F.	10 nm LASO	0.08%	0.07%	1.91E-5
RTA ITO	Cobaltocenium	10 nm LASO	4.42%	8.05%	2.10E-4
RTA ITO	Decamethyl F.	10 nm LASO	2.03%	2.14%	1.20E-4
Carbon	Cobaltocenium	10 nm LASO	0.21%	0.34%	9.86E-6
Carbon	Decamethyl F.	10 nm LASO	0.83%	0.39%	7.31E-6
ITO	Cobaltocenium	None			1.46E-3
ITO	Decamethyl F.	None			8.14E-4
Carbon	Cobaltocenium	None			1.20E-4
Carbon	Decamethyl F.	None			8.77E-5

Chapter 4.3.3. Pinhole testing on PV3D3 and PV4D4 coated ITO and carbon

The PV3D3 and PV4D4 coated samples were tested using the same procedure as the LASO samples. Initial tests with the PV3D3 films were done with the same ACN electrolytes used with the LASO films but every successive tests showed an increase in pinhole density. This suggests that the iCVD films are incompatible with ACN, so cobaltocenium and decamethyl ferrocene in PC were used instead. The results from the pinhole testing with 20 to 100 nm thick films of PV3D3 on ITO are shown in figure 4.8. As the coating thickness increases the pinhole density decreases as expected.

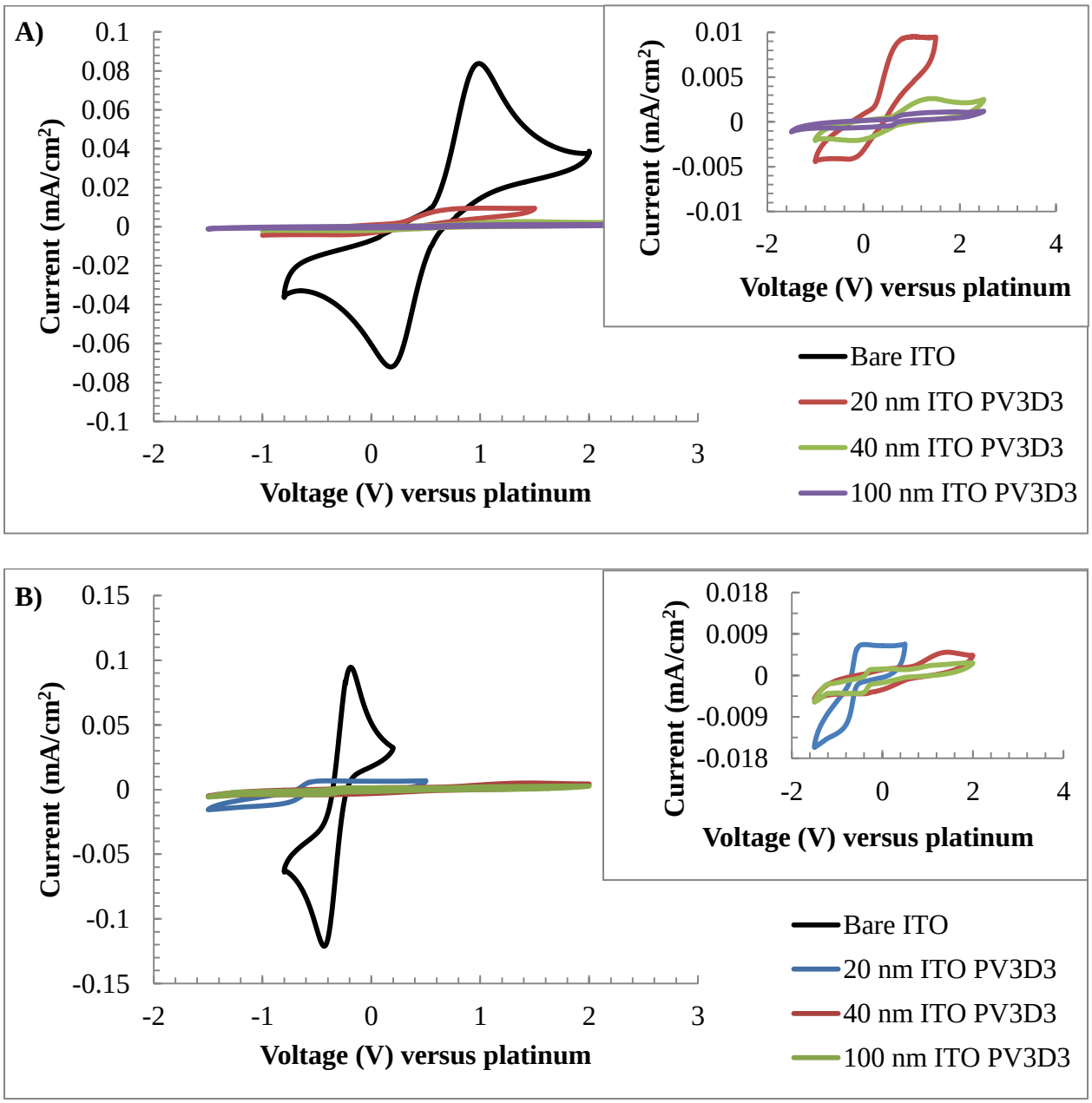

Figure 4.8 Pinhole testing of PV3D3 films on ITO at 200 mV/s in PC using A) Decamethyl Ferrocene and B) Cobaltocenium

The PV3D3 films show minimal pinhole density on ITO but there is a concern that the lithiation process will damage the film. Comparing figure 4.9 to figure 4.8, the lithiation of

PV3D3 decreases the observed current implying a lower pinhole density. These results are consistent with the hypothesis that the lithium sits in the ring of the PV3D3. The addition of the lithium fills the ring, which prevents the redox molecule from accessing the surface.

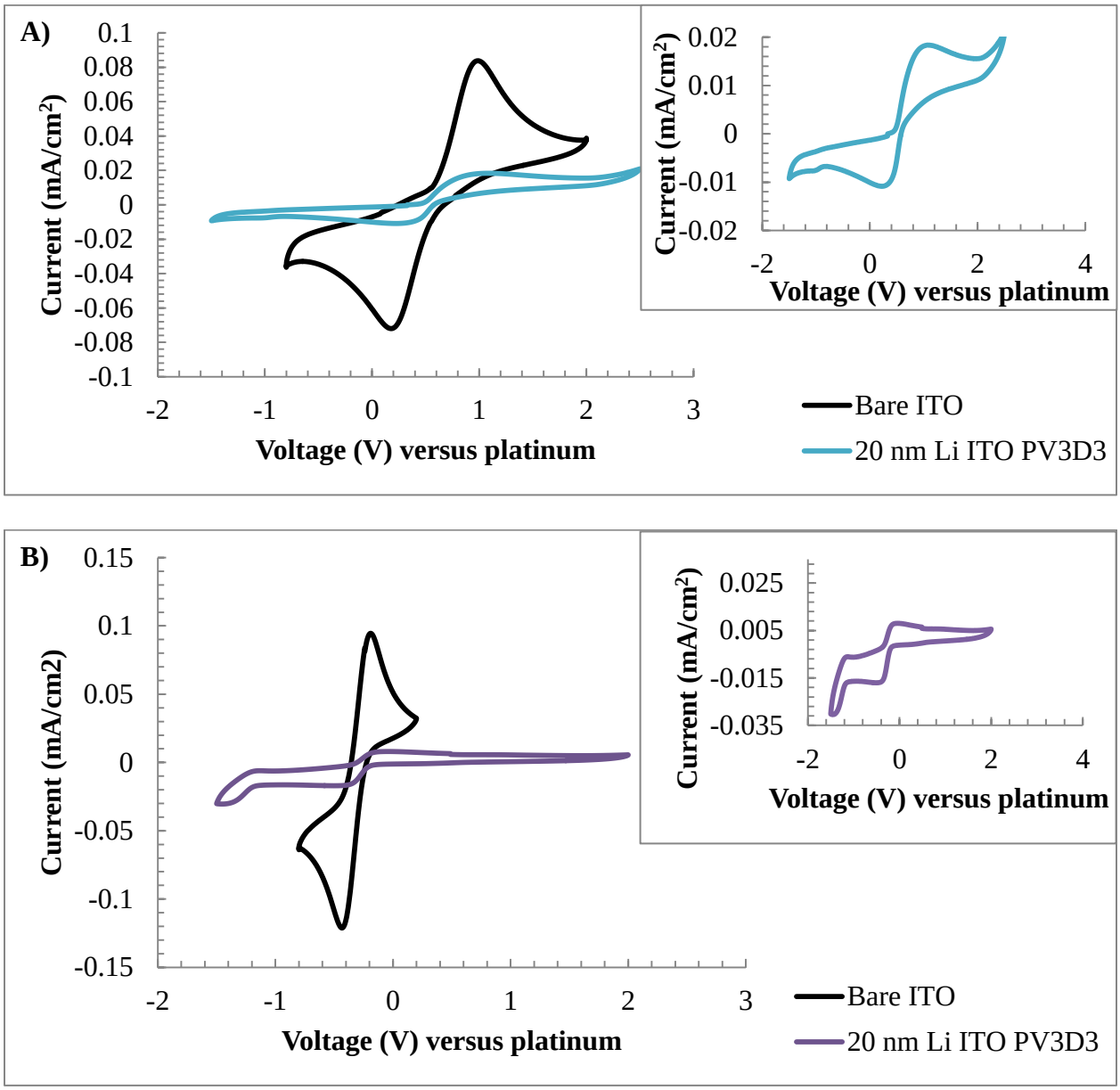

Figure 4.9 Pinhole testing of lithiated PV3D3 films on ITO at 200 mV/s in PC using A) Decamethyl Ferrocene and B) Cobaltocenium

A summary of the results with PV3D3 films with and without lithiation are tabulated in table 4.6. From table 4.6, the PV3D3 coating decreases the heterogeneous rate constant compared to bare ITO. More data is needed to determine if thicker films have lower rate constants since the 40 nm film has a lower rate constants than the 20 nm film but the trend does not hold for the 100 nm film. The addition of lithium further reduces the heterogeneous rate constant, which supports the hypothesis of the lithium impeding the redox molecule.

Table 4.6 Summary of pinhole testing in PC of ITO coated by PV3D3 with and without lithiation

Substrate	Redox	Coating	Pinhole Ox	Pinhole Red	K_s (cm/s)
ITO	Cobaltocenium	20 nm	1.059%	0.877%	2.16E-05
ITO	Decamethyl F.	20 nm	1.349%	0.415%	1.91E-05
ITO	Cobaltocenium	40 nm	0.242%	0.145%	8.85E-06
ITO	Decamethyl F.	40 nm	0.065%	0.144%	6.10E-06
ITO	Cobaltocenium	100 nm	0.014%	0.069%	1.47E-05
ITO	Decamethyl F.	100 nm	0.006%	0.002%	3.93E-06
ITO	Cobaltocenium	20 nm Li	0.083%	0.068%	7.62E-06
ITO	Decamethyl F.	20 nm Li	0.038%	0.373%	5.92E-07
ITO	Cobaltocenium	None			2.66E-4
ITO	Decamethyl F.	None			2.21E-4

Continuing with the testing on ITO, PV4D4 coated films were tested to determine the influence that the larger ring has on pinhole density. Comparing figure 4.10 to figure 4.9, there is an increase in measured current for the PV4D4 coated ITO suggesting that the redox molecules can more easily access the surface through the larger ring. The heterogeneous rate constants in

table 4.7 for the 20 nm thick PV4D4 are higher than their equivalent PV3D3 films in table 4.6, which supports that the larger ring is improving the redox molecule access to the surface. While this increase in pinhole density for the PV4D4 is unwanted, the precursors are cheaper for PV4D4 than PV3D3.

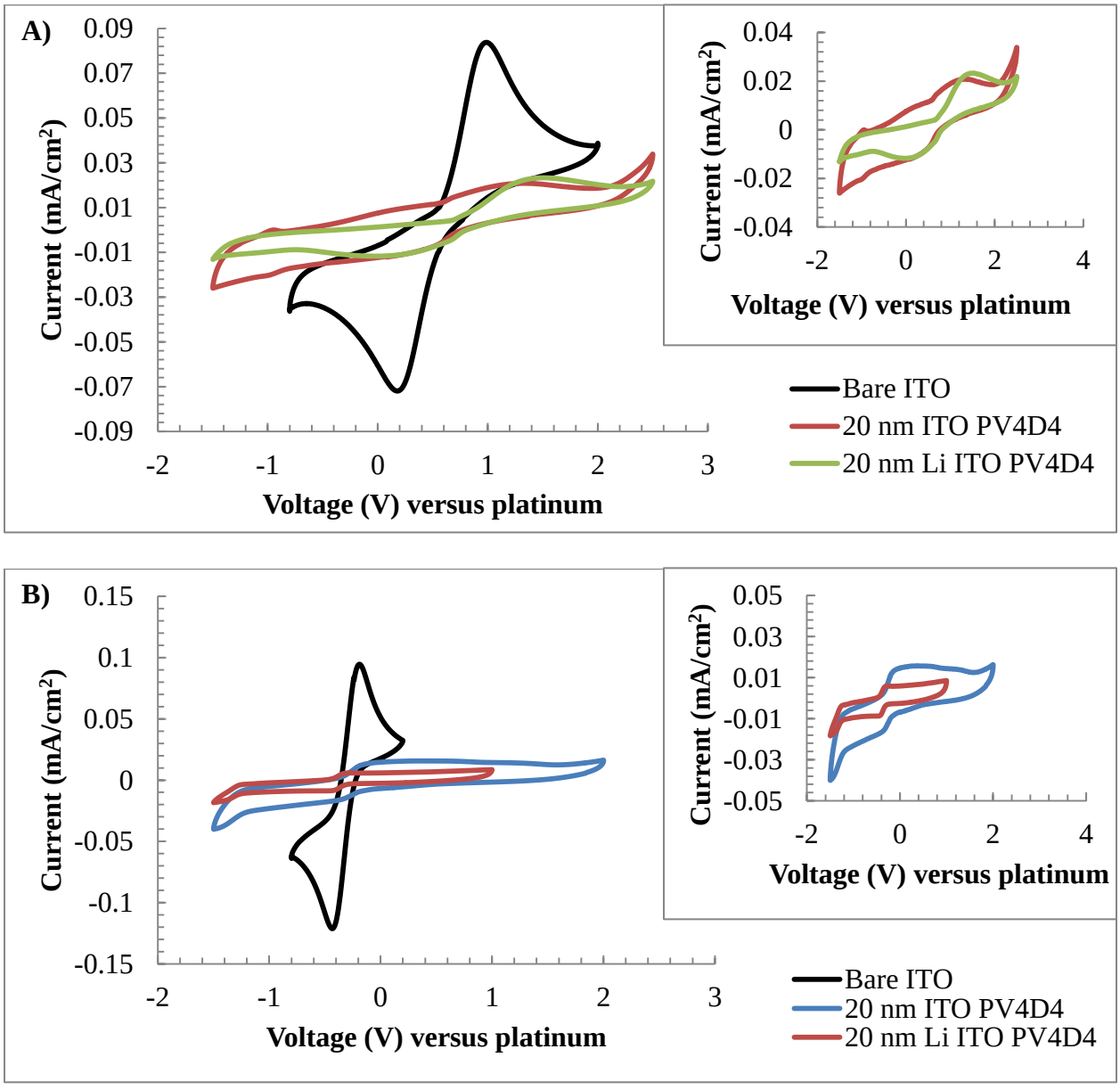

Figure 4.10 Pinhole testing of lithiated PV4D4 films on ITO at 200 mV/s in PC using A) Decamethyl Ferrocene and B) Cobaltocenium

Table 4.7 Summary of pinhole testing in PC of ITO coated by PV4D4 with and without lithiation

Substrate	Redox	Coating	Pinhole Ox	Pinhole Red	K_s (cm/s)
ITO	Cobaltocenium	20 nm	2.588%	4.151%	4.49E-05
ITO	Decamethyl F.	20 nm	3.509%	1.273%	3.00E-4
ITO	Cobaltocenium	20 nm Li	0.721%	0.714%	8.73E-05
ITO	Decamethyl F.	20 nm Li	1.020%	0.871%	2.14E-05
ITO	Cobaltocenium	None			2.66E-4
ITO	Decamethyl F.	None			2.21E-4

PV3D3 samples were deposited on carbon and the same trends observed with coated ITO were again observed with the coated carbon samples. Figure 4.11 shows the reduction of the current from the coated films and the same trend with additional decreases of current due to coating thickness and lithiation. The coatings were not as complete as on ITO, which is likely due to the rougher surface of the carbon electrodes. The rate constants for the carbon coated samples show the same trend of reducing with increasing thickness but the effect of lithiation on rate constant is not conclusive.

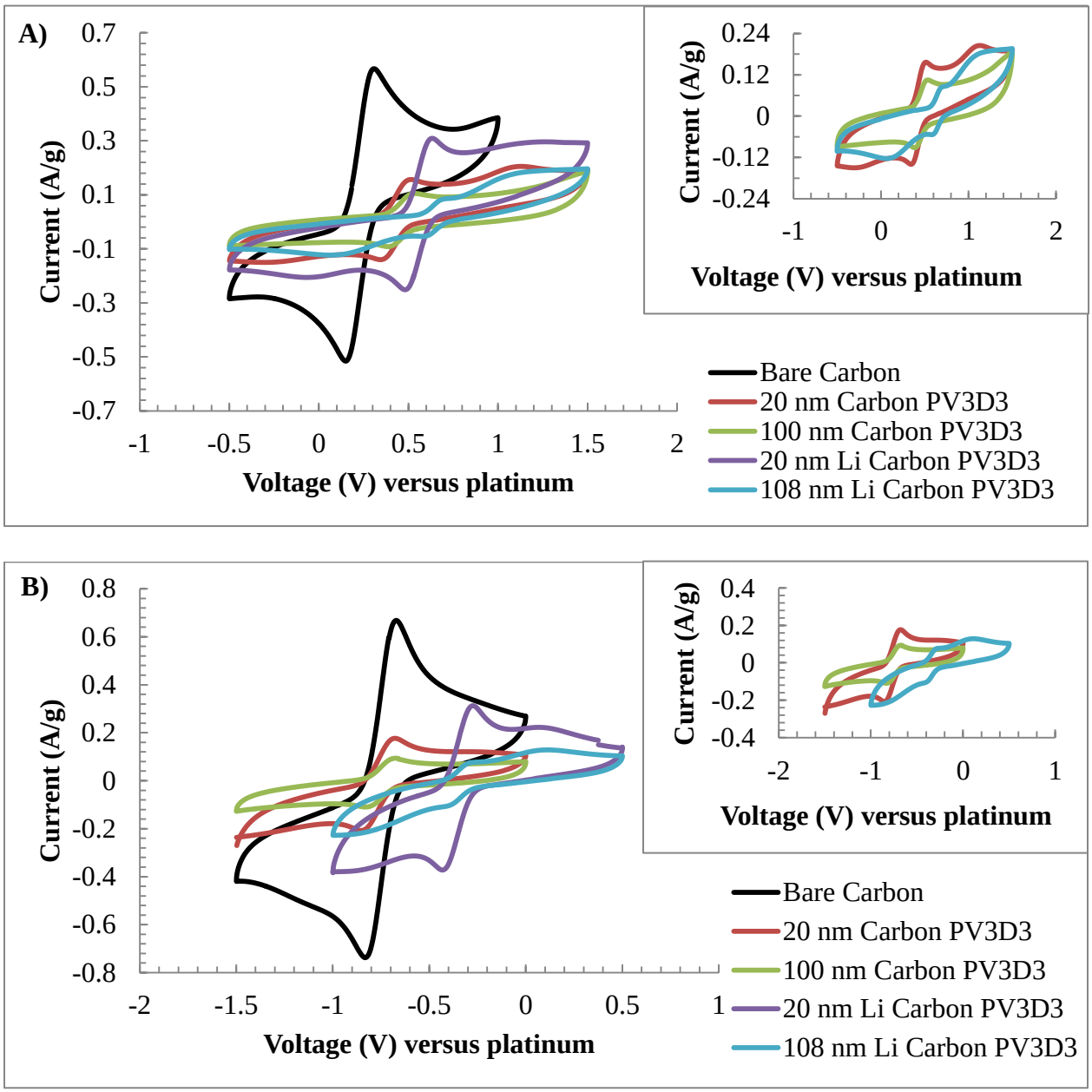

Figure 4.11 Pinhole testing of as deposited and lithiated PV3D3 films on carbon at 200 mV/s in PC using A) Decamethyl Ferrocene and B) Cobaltocenium

Table 4.8 Summary of pinhole testing in PC of PV3D3 coated carbon with and without lithiation

Substrate	Redox	Coating	Pinhole Ox	Pinhole Red	Ks (cm/s)
Carbon	Cobaltocenium	20 nm	0.878%	0.842%	1.48E-06
Carbon	Decamethyl F.	20 nm	1.636%	1.450%	1.49E-06
Carbon	Cobaltocenium	108 nm	0.329%	0.340%	1.23E-06
Carbon	Decamethyl F.	108 nm	0.785%	0.812%	1.27E-06
Carbon	Cobaltocenium	20 nm Li	0.566%	0.666%	1.67E-06
Carbon	Decamethyl F.	20 nm Li	1.089%	0.999%	1.64E-06
Carbon	Cobaltocenium	100 nm Li	0.062%	0.098%	1.28E-06
Carbon	Decamethyl F.	100 nm Li	0.166%	0.144%	1.07E-06
Carbon	Cobaltocenium	None			2.20E-05
Carbon	Decamethyl F.	None			1.55E-05

Chapter 4.3.4. Impedance testing of LASO coated ITO

Preliminary testing of the LASO films on ITO showed good transport of the lithium through the amorphous film. LASO films of varying nanometer film thickness were deposited on ITO and their impedance, displayed in figure 4.12, has the shape of a semicircle, indicative of charge transport through a film. The impedance data was modeled using the standard randles circuit and the resistance was used to calculate the conductivity of $5 * 10^{-9}$ S/cm from the average of the tested films.

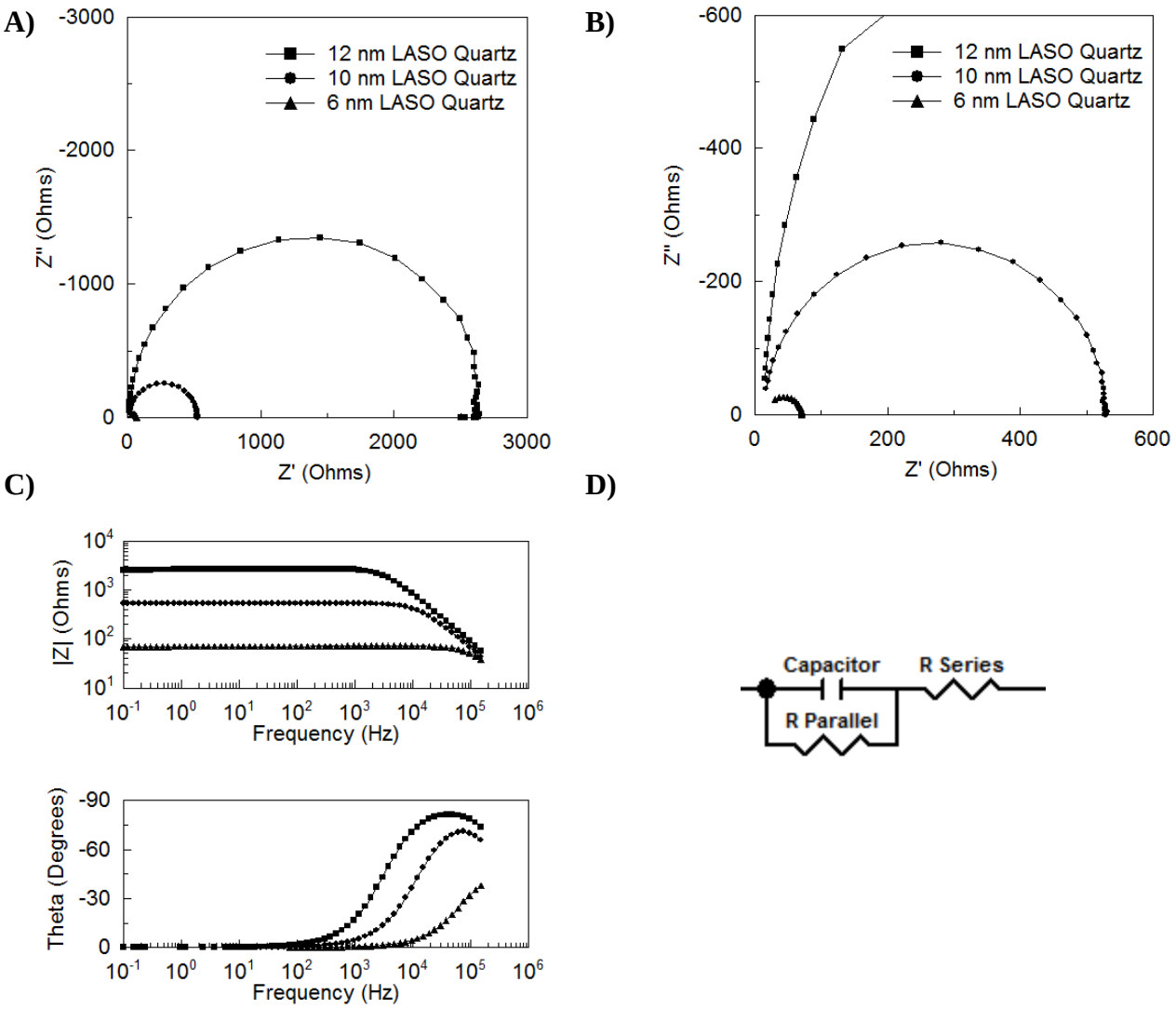

Figure 4.12 A) Nyquist B) Zoom in C) Bode plot D) Equivalent circuit for LASO films with thickness of 12, 10 and 6 nm

Since the RTA increases the pinhole density, it is of concern that it reduces the ionic conductivity. The impedance was measured for 10 nm thick LASO films on ITO with and without RTA is shown in figure 4.13. Figure 4.13 shows a large increase in impedance for the RTA film and a reduction in conductivity to $1 * 10^{-10}$ S/cm, which further support that the RTA cracks the film.

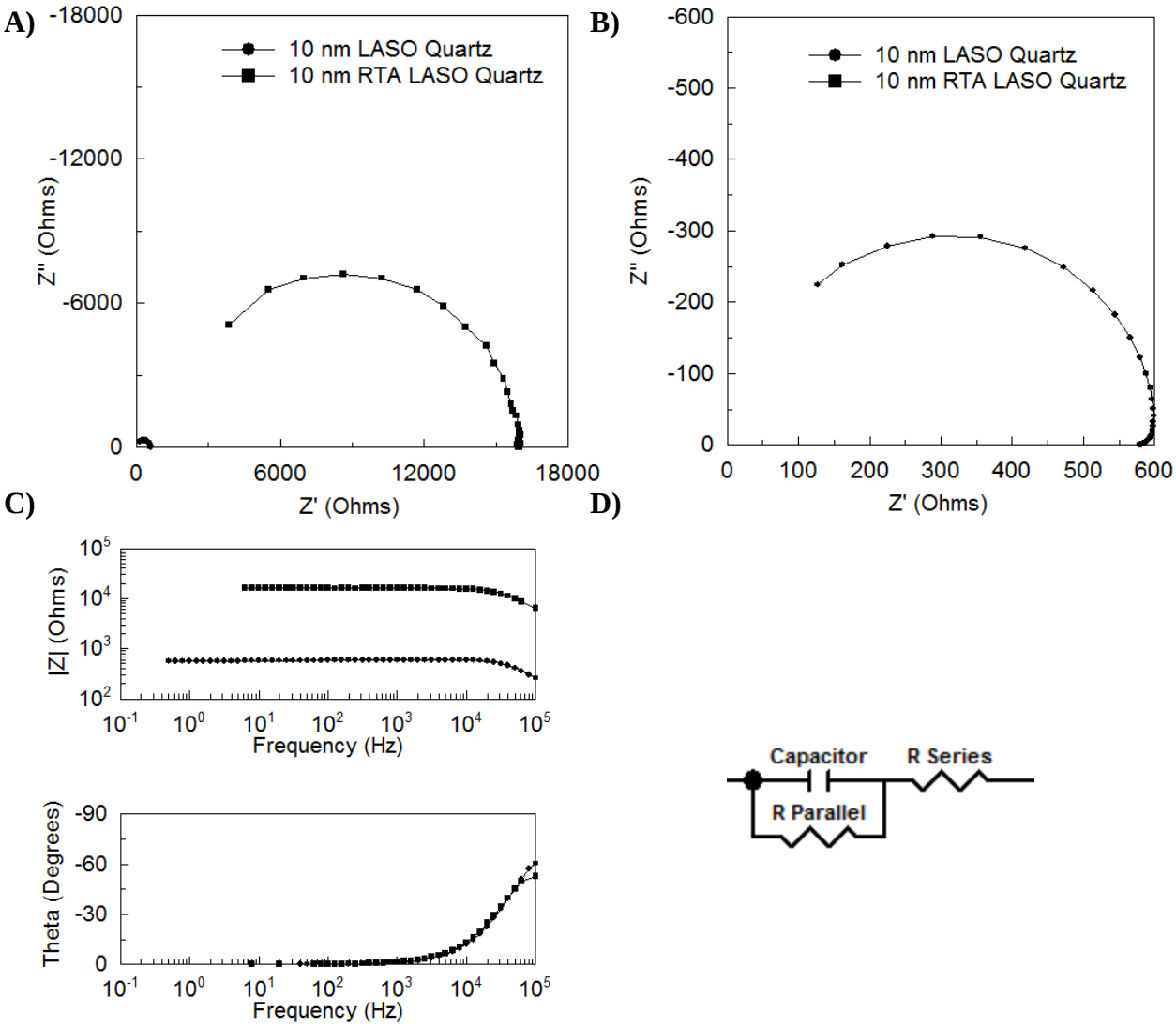

Figure 4.13 A) Nyquist B) Zoom in C) Bode plot D) Equivalent circuit for 10nm thick LASO films on quartz with and without RTA

Chapter 4.3.5. Impedance testing of PV3D3 and PV4D4 on ITO

The 20 nm PV3D3 samples with and without lithiation were tested by impedance spectroscopy. From figure 4.14 the as deposited PV3D3 is an insulator since there are no conducting ions. After the addition of lithium, the conductivity rises to 2.3 * 10^{-9} S/cm for the 20 nm thick film shown in figure 4.14 C and figure 4.14 D. The impedance results support the hypothesis that the lithiated films are ionic conductors due to their semicircle nyquist plots.

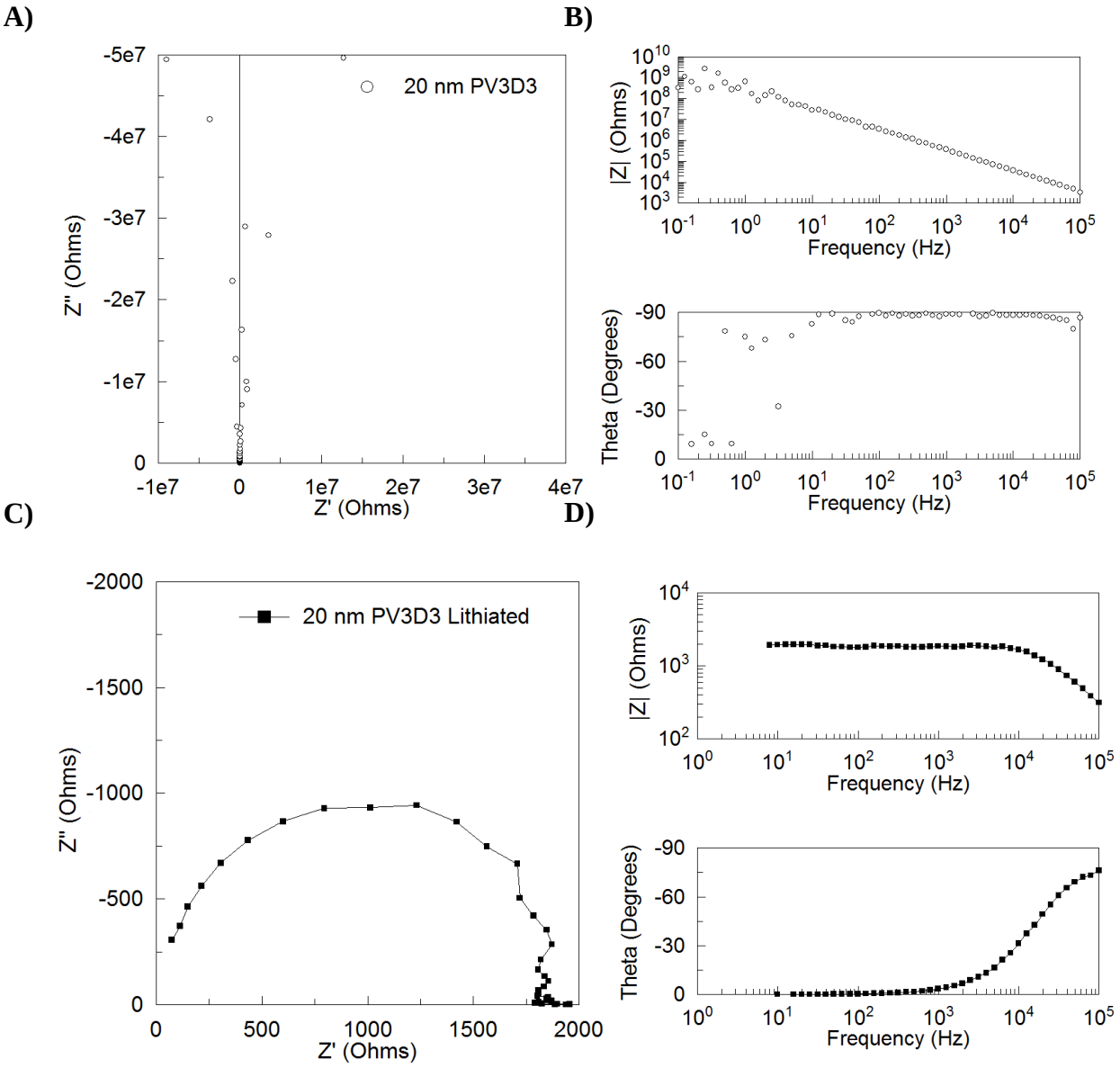

Figure 4.14 Impedance of 20 nm PV3D3 on ITO as prepared A) Nyquist plot B) Bode plot, and lithiated C) Nyquist plot and D) Bode plot

After testing the samples in the redox molecules, the 20 nm lithiated PV3D3 and PV4D4 films were tested by impedance to determine their conductivity. Comparing figure 4.15 to figure 4.14, the 20 nm lithiated PV3D3 film has an increased resistance. This increase in resistance could be due to redox molecule still in the film despite rinsing with electrolyte. The PV4D4 film

has a much lower impedance than the PV3D3 film and a conductivity of 5 * 10^{-8} S/cm. The wider ring structure may be improving the lithium transport through the film.

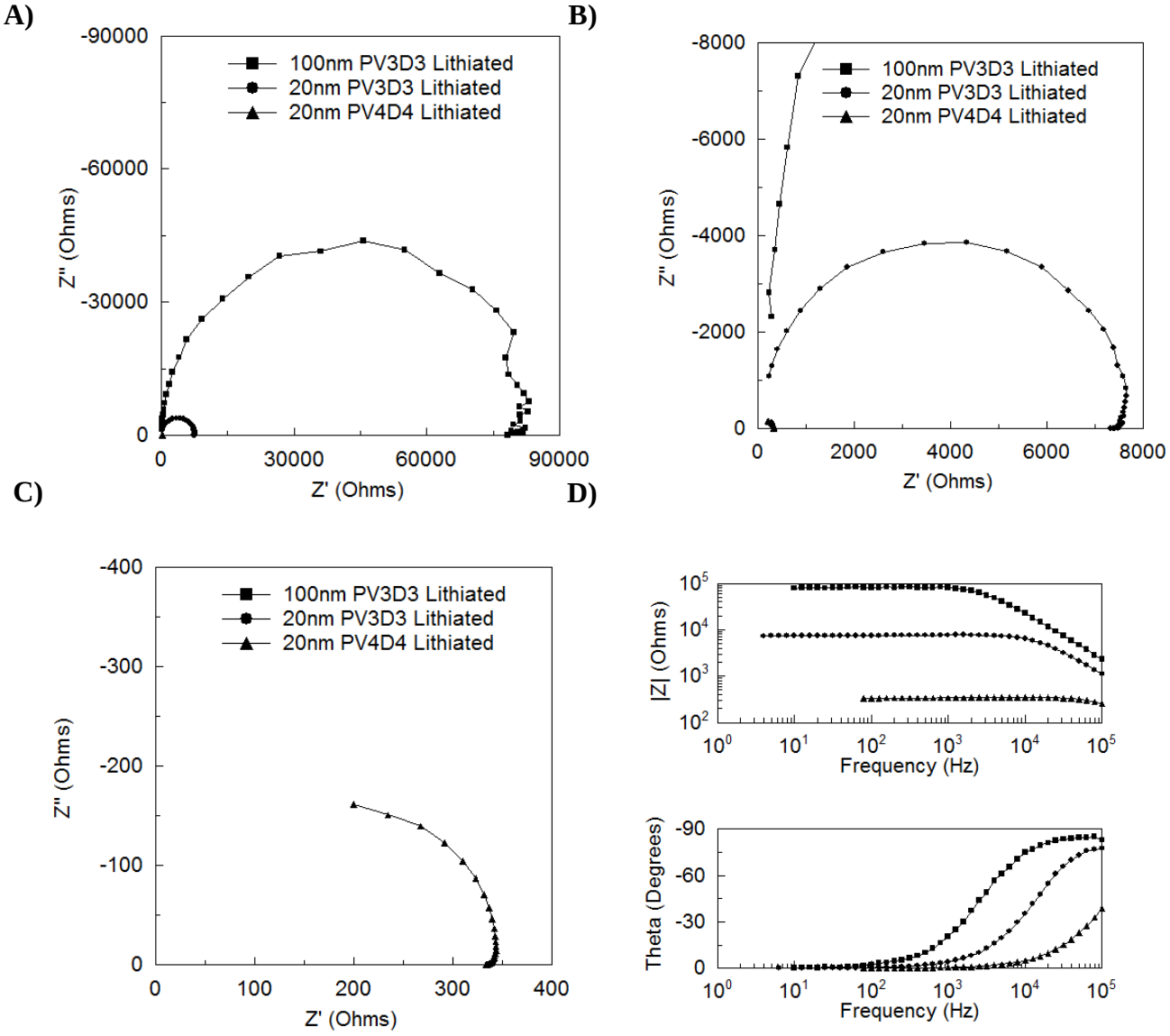

Figure 4.15 Impedance of Lithiated PV3D3 and PV4D4 post pinhole testing A) Nyquist plot and B) Zoom in C) Additional zoom D) Bode Plot

Chapter 4.3.6. Comparison of LASO, PV3D3 and PV4D4 as Solid Electrolytes

The summary from the pinhole testing on ITO and carbon is shown in figure 4.16. Since the pinhole densities were similar for both cobaltocenium and decamethyl ferrocene across all

the samples, it is likely that the pinhole diameters are greater than the diameter of both redox couples. The RTA LASO coated ITO has the highest pinhole density and is comparable to the as prepared PV4D4 films. For the coated carbon samples, the 10 nm LASO coatings are comparable to the 20 nm lithiated PV3D3.

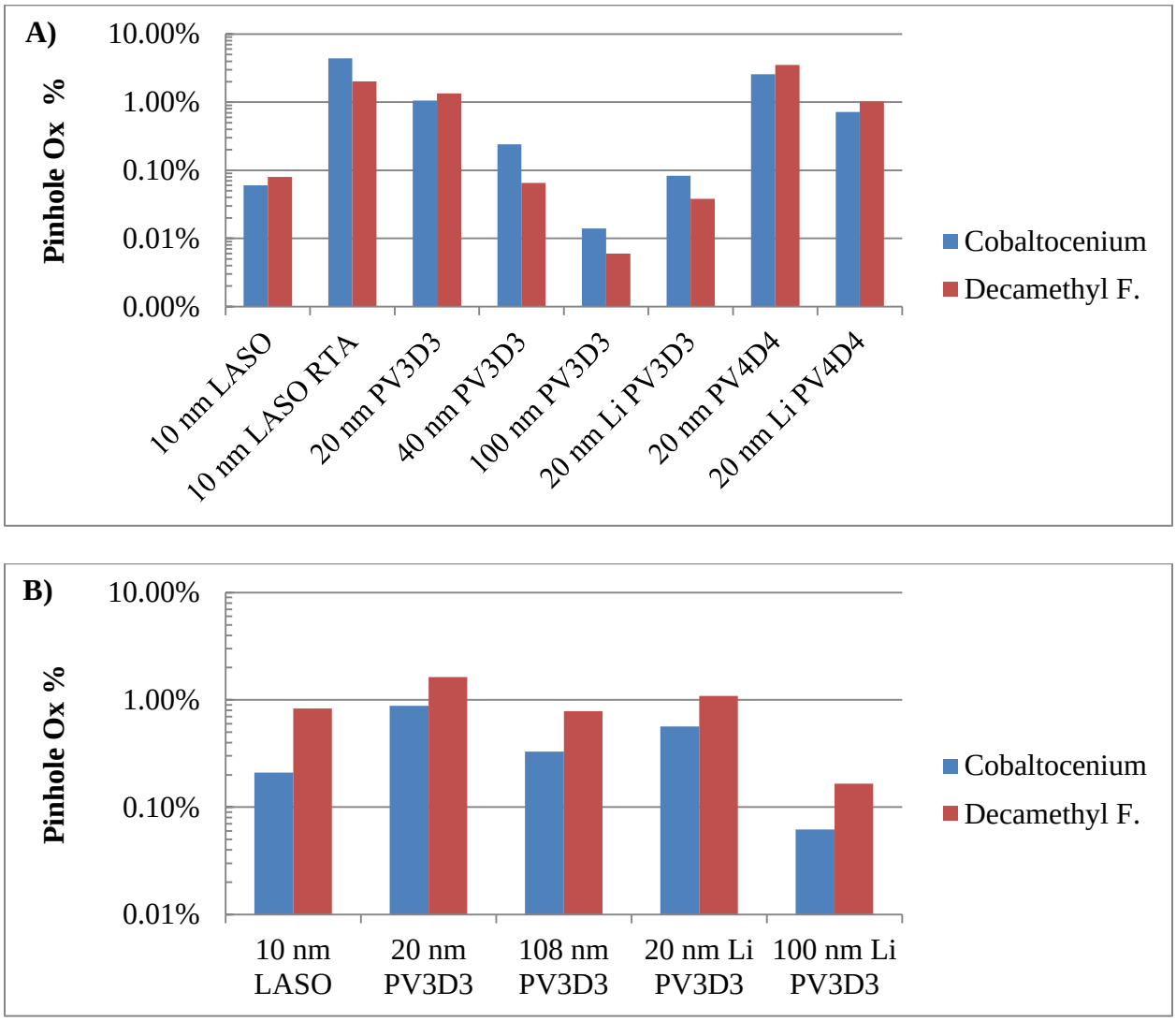

Figure 4.16 Pinhole density of coated A) ITO and B) Carbon substrates calculated from the oxidation diffusivity

Chapter 4.4. Conclusion

The non-aqueous technique of characterizing pinholes matches well with literature values for diffusivity and heterogeneous rate constant for the tested redox molecules. There is good agreement between the processing conditions and the results from pinhole testing such as thicker films having a more complete coverage and coated samples having lower heterogeneous rate constants that uncoated films. Due to the pinhole size in these samples being larger than the diameter of all the tested redox couples, it is not clear if this technique can quantify pinhole diameter. This technique works well with quantifying the pinhole density of the coated samples.

The conformal solid electrolytes deposited by ALD and iCVD have been characterized by electrochemical testing. Both these deposition techniques successfully coat the rough carbon surface as well as the smoother ITO substrates. RTA of the LASO films has been shown to greatly damage the film as well as reduce the ionic conductivity instead of improve it. Lithiation of the PV3D3 films reduces the pinhole density as well as increases the conductivity to levels similar to the LASO films. The PV4D4 has the highest conductivity and is a promising choice for a solid electrolyte for 3D microbatteries.

Chapter 5. Conclusions

The common theme of characterizing materials has been demonstrated for three separate systems. In the first system the quasi-solid ionogel made by sol-gel encapsulation demonstrated that improved packaging can be achieved without a loss in performance. This sol-gel approach can be generalized beyond double layer capacitor to improve any system that uses a gelled electrolyte.

In the second system the methodology for testing Nb_2O_5 yielded information about how the conductivity changes with lithiation and how phase changes could occur when the sample is heated in the presence of lithium. This work can serve as the beginning of mapping the phase changes of the Nb_2O_5 system and serves as an alternative to high temperature synthesis routes. This work could also be applied to other electrode systems to better understand their conductive properties.

In the third system the method of characterizing the presence of pinholes in solid electrolyte films was firmly established. The pinhole testing can be used on complex structures and serves as a complementary approach to standard literature techniques for measuring pinhole density. This approach could also be used to quantify damage to an electrode during cycling by being sensitive to changes in the electrode area. By understanding the fundamentals for these three systems, electrodes with better architecture can be fabricated and characterized.

Appendix 1

Silica Sol-Gel Chemistry: Creating Materials and Architectures for Energy Generation and Storage

Daniel Membreno • Leland Smith • Bruce Dunn

Department of Materials Science and Engineering

University of California, Los Angeles

Los Angeles, CA 90095

email: BDunn@ucla.edu

Abstract

There is widespread recognition that the use of energy in the 21st century must be sustainable. Because of its extraordinary flexibility, silica sol-gel chemistry offers the opportunity to create the novel materials and architectures which can lead to significant advances in renewable energy and energy storage technologies. In this paper, we review some of the significant contributions of silica sol-gel chemistry to these fields with particular emphasis on electrolytes and separators where sol-gel approaches to functionalization and encapsulation have been of central importance. Examples are presented in the areas of dye-sensitized solar cells, biofuel cells, proton exchange membrane fuel cells, redox flow batteries and electrochemical energy storage. Original work is also included for the sol-gel encapsulation of a room temperature ionic liquid to create a solid state electrolyte for electrochemical capacitors. In view of the critical importance of energy and

the versatility of the sol-gel process, we expect the sol-gel field to play an increasingly important role in the development of sustainable energy generation and storage technologies.

Keywords

Sol-gel • Encapsulation • Energy Storage • Ionic Liquids

1. Introduction

The projected doubling of global demand for electricity by 2050 has stimulated a worldwide effort at developing sustainable energy strategies. Environmental concerns regarding fossil fuel usage in combination with energy security issues have led to the extensive development of renewable energy sources, particularly solar and wind which are readily available across much of the globe [109, 110]. From 2011 to 2012 global renewable electricity generation grew by 8.2% and now exceeds the electricity consumption of China [111]. It is well recognized that the intermittent nature of solar and wind energy requires some form of energy storage, which represents a conversion process from one form of energy to another. Thus, while electrochemical energy storage is widely considered for a broad range of applications having to do with mobile power, the conversion of solar energy into fuels represents an attractive alternative [112].

Sol-gel chemistry offers an incredible breadth of opportunities for energy generation and storage. The sol-gel process goes well beyond the ability to simply synthesize compounds and non-crystalline solids. By controlling the chemistry of the process, a number of research groups in the sol-gel community have demonstrated the ability to create novel materials and architectures; from fully dense materials to high porosity, high surface area aerogels. The range of possible compositions is extraordinary; from insulating materials to electrochemically active

transition metal oxides to semiconducting sulfides and various forms of carbon. With each, there is the prospect of preparing the desired material in a variety of forms including powders, films, fibers and bulk monoliths. In this way, the sol-gel process possesses a technological versatility that is rarely matched by other synthesis routes.

In this paper, we briefly review some of the more significant contributions to the fields of energy generation and storage, which have been enabled by sol-gel chemistry. The synthesis approaches that serve as the basis for creating the materials and morphologies have been well reviewed in the literature over the years and thus we are able to focus on the scientific and technological advances [64, 113, 114]. For the most part, we do not cover the application of sol-gel methods for the synthesis of compounds, such as those that are commonly used in battery electrodes. Rather, we emphasize electrolytes and separators, where sol-gel approaches to functionalization and encapsulation offer unique features that lead to improvements in device performance. The majority of these works use alkoxysilanes as a starting material, yielding silica gels. The energy technologies we cover include dye sensitized solar cells, fuel cells, redox flow batteries and electrochemical energy storage. For the latter topic, which is clearly the most commercial, we believe that the sol-gel encapsulation of ionic liquids offers a unique direction for designing the properties of electrolytes that possess the mechanical integrity of an inorganic network but with ion transport properties comparable to those of liquid electrolytes. In the final section of this paper, we briefly present new results on the encapsulation of ionic liquids within a silica gel for capacitive energy storage.

In view of the critical importance of energy and the inherent flexibility of the sol-gel process, we expect sol-gel chemistry to play an increasingly important role in the development of energy generation and storage technologies.

2. Dye Sensitized Solar Cells

The generation of electricity from solar energy is of great interest due to the large amount of incident sunlight on the earth's surface. The key challenge has been to convert large amounts of this sunlight into electrical energy [115]. An impediment to solar cell adoption is the cost of producing the solar cell, which for inorganic cells includes high temperature processing and vacuum deposition. With recent gains in efficiency, dye sensitized solar cells (DSSC) have become a promising alternative to traditional inorganic solar cells, and sol-gel chemistry has made considerable contributions to those gains.

DSSCs use a dye molecule whose photo-electrochemical properties convert incident light into electricity. For solar cells to compete with fossil fuels in energy production, they need to have both high efficiency and low cost. For efficient energy conversion, the dye must be in direct contact with the electrode so a high surface area, porous TiO_2 layer, often made by sol-gel processes, is used as shown in Figure 1 [116]. TiO_2 is usually the material of choice because it is compatible with iodine electrolytes and its conduction band is slightly lower than the highest occupied molecular orbital (HOMO) for the organic dye molecules, commonly ruthenium based. The dye molecule is the active component of the device that converts light into electrons and holes. The electrons move into the TiO_2 while the holes are shuttled by the iodine to the current collector, typically platinum. As well as being an electron acceptor, TiO_2 helps to scatter the light back into the dye to improve the chances that the light will interact with the dye molecule. The iodine electrolytes are often gelled using a sol-gel process in order to provide mechanical stability to the device without degrading the ionic conductivity [117]. All of the processes in a DSSC can be assessed together by considering the power conversion efficiency (PCE): the harvested electrical energy divided by the amount of incident solar energy.

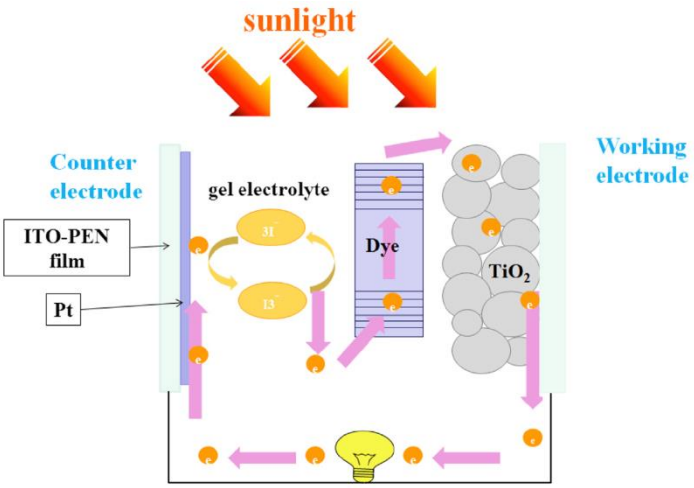

Fig. 1 Diagram of a basic dye sensitized solar cell. Light enters the transparent working electrode and then interacts with the ruthenium based dye adsorbed onto the mesoporous TiO_2. The dye produces an exciton, an electron and a hole, which then dissociates towards opposite electrodes. The electron moves through the TiO_2 into the working electrode and through the external circuit. The hole is transported by the iodine electrolyte to the counter electrode where it combines with the electron for conservation of charge. Diagram is adapted from [116]

An important motivation for DSSC development is the continued increase of PCE. Beginning with the seminal work by Grätzel [118], the DSSC field has made numerous advances leading to increasingly greater PCEs; recent reports indicate values above 10% [119]. The higher PCE is partly due to greater ionic conductivity from the use of more volatile acetonitrile (ACN) electrolytes rather than propylene carbonate (PC) electrolytes. The impetus for using sol-gel methods to encapsulate the electrolytes is the prospect of finding a chemistry that provides encapsulation without decreasing the ionic conductivity by tortuosity.

One challenge in developing sol-gel encapsulation for DSSC is the poor solubility of the iodine electrolytes in inorganic sol-gel precursors. Organic components have better solubility for iodine and thus one option is mixing poly(ethylene glycol) (PEG) and tetraethoxysilane (TEOS) to form a composite. However, when the PEG/TEOS gel was used in a DSSC, the efficiency was poor, ~ 1%, due to the electrolyte losing contact with the electrodes and agglomeration effects between the organic and inorganic components [120]. An improvement to the simple mixing of the precursors was to have an acetic acid catalyzed sol-gel reaction which crosslinked the TEOS and the PEG [120]. The resulting sol-gel based device had an increase in PCE to ~ 4%, which was influenced by the gelation time. If the sol-gel reaction occurs too quickly, such as with hydrochloric acid, the gel will entrap sol-gel reaction byproducts and the PCE will decrease.

The PCE can be increased further by optimizing the composition to produce gels with higher ionic conductivity. An important consideration here is that the mobility of the iodine ions largely controls the performance of the DSSC. Recent studies systematically examined the effect of iodine concentration on ionic conductivity [121]. Using a similar organic-inorganic system comprised of TEOS, acetic acid and a slightly heavier PEG, the conductivity was optimized by tailoring the sol-gel synthesis and an improved PCE of ~5% was achieved.

Ionic liquids are room temperature molten salts that represent an alternative to PEG and PC. Ionic liquids provide moderate ionic conductivity, low electronic conductivity and good solubility for the iodine electrolytes. Organic electrolytes have an order of magnitude higher ionic conductivity than ionic liquids, but their high vapor pressures limit the lifetime of these devices [122]. Ionic liquids are non-flammable solvents with very low vapor pressure and high thermal stability in excess of 200°C [20]. These properties will be beneficial in improving the lifetime of a DSSC, which is susceptible to being heated by the sun.

Beyond being a replacement for the organic solvent in the sol-gel process, an ionic liquid containing iodine anions can be used as the iodine source in the DSSC. Quasi-solid state electrolytes were fabricated with tetramethylorthosilicate (TMOS) and acetic acid for the sol-gel reaction, PC as the solvent, along with the ionic liquid, 1-Methyl-3-propylimidazoliumiodide (MPII), N-methylbenzimidazole and iodine precursors as the conducting salts [123]. By optimizing the concentration of the iodide salts in PC, the ionic conductivity was maximized as was the percolation of the redox dyes, resulting in a device with a PCE of 5.4%. It is likely that replacing the PC with an ionic liquid will lead to improved device lifetime with similar performance. Speaking to the issue of cost, ionic liquids are generally $1000/L, compared to $70/L for PC and $460/L of 0.5 M MPII. Ionic liquid would double the price of the chemicals used in the DSSC, which would increase the overall cost of the DSSC by 15% according to the cost breakdown model by Kalowekamo et al [124]. This increase in cost would likely be mitigated by the improved performance and lifetime of the DSSC.

3. Fuel Cells and Redox flow batteries

Fuel cells represent a class of energy conversion technologies that directly convert chemical fuel and an oxidant, typically oxygen, into electricity. While the overall chemical reaction is analogous to combustion, direct electrochemical conversion can exceed the thermodynamic limitations of the Carnot cycle while simultaneously avoiding environmental pollution [125].

Fuel cells are generally categorized according to their fuel and the mechanism by which direct electrochemical conversion is achieved. Biological fuel cells (BFC) use biological

molecules such as sugar or ethanol as a fuel source, and oxidize these fuels via biochemical processes [126]. Proton exchange membrane fuel cells (PEMFC) use hydrogen or methanol as fuel, platinum and/or ruthenium catalysts, and membranes that are both proton conducting and electrically insulating to separate the anode and cathode reactions [127]. Redox flow batteries (RFB) are also known as electrochemically regenerative fuel cells. They function similarly to PEMFC in that a membrane is used to selectively conduct ions between two electrolyte solutions that undergo reversible redox reactions on charge and discharge [128].

Sol-gel science is broadly applicable to fuel cell technologies. For BFC devices, sol-gel synthesis methods are used to immobilize microbes, enzymes, co-factors and mediators into biocompatible matrices that maintain enzymatic activity and facilitate electron transfer between the active biological materials and conductive supports. Whereas organic polymerization involves toxic monomers, reactive catalysts and high temperatures, sol-gel networks are formed at moderate temperatures from relatively benign sols and dilute acid/base catalysts. For PEMFC and RFB, sol-gel chemistry provides a versatile route to hybrid membranes that couple the flexibility and toughness of organic polymers with the chemical and thermal stability of inorganic networks [129]. Sol-gel synthesis is easily performed in both aqueous and non-aqueous solutions, which allows for creative processing techniques. The combined inorganic/organic chemistry enables researchers to tune the hydration, swelling and ion-exchange properties of these membranes.

3.1 Biological Fuel Cells

BFCs are often divided into two subgroups depending on the nature of the biocatalyst. If living cells are used, the system is referred to as a microbial fuel cell (MFC) while systems that

use isolated enzymes are called enzymatic fuel cells (EFC). A clear advantage of MFCs is that the organisms are able to regenerate the required enzymes as part of their normal functioning [130]. Moreover, because cells can contain a variety of enzymes, MFCs can generate current from different types of fuels simultaneously. In contrast, EFCs involve simpler chemical pathways and generally have faster response times [126]. Both systems require an effective pathway for electron transfer (ET) from the biocatalyst to the current collector. This can be accomplished either via direct electron transfer (DET) from contact with the current collector or via redox active mediators that diffuse between the biocatalyst and the current collector, mediated electron transfer (MET). Shown below in Figure 2 is a schematic of an EFC with MET at both electrodes, using glucose as a fuel [131]. The voltage obtained with BFCs is reduced by electron transfer kinetics, ohmic resistance and concentration gradients while current is limited by ion transport and low active material loading at the electrodes [132]. Low power is a principal shortcoming of BFCs.

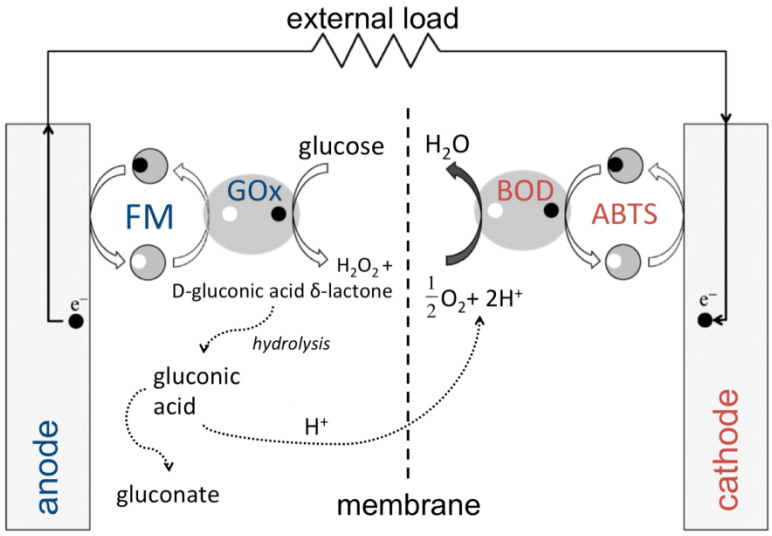

Fig. 2 An example of an EFC which uses MET at both electrodes. At the anode glucose oxidase (GOx) catalyzes the oxidation of glucose and ferrocene methanol (FM) acts as a redox shuttle. At

the cathode bilirubin oxidase (BOD) reduces protons and oxygen to form water with the help of the mediator 2,2'-azino-bis**(**3-ethylbenzothiazoline-6-sulfonic acid) diammonium salt **(**ABTS**)**. Adapted from [131] and [126]

The main benefit of sol-gel technology for BFCs is the ability to immobilize the biocatalyst on the current collector. Immobilization is less important for MFC because the microbes tend to grow as a biofilm that naturally adheres to the current collector [130]. However, EFCs benefit from immobilization both to maintain the enzyme's biological activity and to improve electron transfer [131]. As a result, sol-gel chemistry is more frequently applied to EFCs rather than MFCs. Because silica gels are inert and readily obtained from a variety of precursors and methods, the sol-gels applied to BFCs thus far are predominately silica-based.

Nearly all biochemical processes are catalyzed by enzymes. Oxidoreductases, which are responsible for electron-transfer reactions, are the enzymes most commonly used in EFCs [126]. Sol-gel encapsulation has advantages over other encapsulation methods because it allows for customization of network chemistry and pore size to improve biocompatibility. Enzymes can be immobilized within the porous gel network without covalent bonding that would otherwise interfere with enzyme activity [133]. Still, enzymes are affected by their chemical environment. Specifically, the negative charge on the silica matrix will repel negatively charged surface groups on the enzymes thereby interfering with enzymatic function. The negative charge can be neutralized through the incorporation of positively charged polyelectrolytes such as polyethylene glycol, polyethylenimine and poly(dimethyldiallylammonium chloride) [131, 133, 134]. Furthermore, biopolymers such as chitosan can be included in the sol to improve the

biocompatibility of the gel [135]. The porosity of the silica matrix can also be controlled by varying the amounts of solvent, the nature of the catalyst and the pH of the sol-gel reaction [126]. The pore size of the sol-gel network is important as large pores can cause the enzyme to leach out while small pores can limit the mass transport of mediator molecules [126].

Some recent reports of sol-gel encapsulation of biocatalysts for biological fuel cells are shown in Table 1. Strack et al. used vapor phase deposition of TMOS to encapsulate both a microbial anode and an enzymatic cathode into a hybrid BFC [136]. The open device design allowed for continuous operation for over a week using raw sea water as a fuel source. The device was able to achieve a volumetric power density of 340 mW/m^3 at 0.46 V. No mediators were used aside from the flavins that are naturally produced by shewanellan oneidensis at the anode. A number of groups have used mediators to improve BFC performance. For mediators to successfully transfer electrons, they must operate at a potential that is shifted from the potential of the enzyme, resulting in thermodynamic losses [126]. Addition of a mediator is only beneficial if current is increased to overcome such losses, which means that large mediator concentrations are often required. For this reason, mediator immobilization is used to avoid the problem of leaching and to maintain high mediator concentrations [133].

As noted by Lim et al. mediator diffusion can be slowed by the silica network if the mediators bear a negative charge. This effect can be minimized by the addition of some positively charged polyelectrolytes to the gel [131]. Carbon nanotubes were also added to impart the gel with electrical conductivity and thereby facilitate DET in addition to MET resulting in a device with an areal power density of 120 $\mu W/cm^2$ at 0.24 V using 100 mM glucose as fuel [131].

Table 1 Biofuel cells which incorporate sol-gel encapsulation of enzymes and other proteins

Source	Anode /Mediator	Cathode/ Mediator	Precursors	Solvent	Method
Lim 2007 [131]	GOx/ ferrocene methanol	BOD/ ABTS	TMOS	water	mold casting
Szot 2008 [137]		Laccase/ABTS	TMOS-MIM TFSI	methanol	layer-by-layer assembly
Deng 2010 [135]	alcohol dehydrogenase/ Meldola's blue	Laccase	(3-mercaptopropyl)-trimethoxysilane /chitosan	water	EAD
Niedziolka-Jonsson 2011 [138]		BOD	TMOS-MIM TFSI/ TMOS	nitrobenzene water	EAD at the aqueous/organic interface
Wang 2011 [134]	d-sorbitol dehydrogenase /ferrocene		TEOS	water	EAD
Strack 2013 [136]	Shewanella oneidensis DSP-10	BOD	TMOS		chemical vapor deposition
Urbanová 2013 [133]	glucose dehydrogenase /menadione		TEOS / (3-glycidoxypropyl) trimethoxysilane	water	drop casting and EAD

The addition of electronically conducting particles is frequently used to improve BFC performance. In addition to CNTs, carbon nanoparticles and gold nanoparticles have also been added into gels [135, 137]. Concentration polarization can be decreased, and operational voltages

increased by decreasing mediator diffusion lengths [131]. Therefore, it is necessary to keep the enzymes, mediators, conductive particles and current collector all in close proximity. Electrochemically-assisted deposition (EAD) is an intriguing technique whereby electric fields are used to generate protons near a conductive surface. These protons catalyze gelation from dilute precursor solutions resulting in gels with controllable thickness [133–135, 138]. Deng et al. deposited a composite gel containing chitosan biopolymer and gold nanoparticles via EAD in order to fabricate a full EFC device that produced a power density of 1.56 mW/cm^2 at 0.55 V using ethanol as the fuel and ethanol dehydrogenase as the anodic enzyme [135].

Another interesting trend is the increasing use of 1-methyl-3-(3-trimethoxysilylpropyl)imidazolium bis(trifluoromethyl-sulfonyl)imide (TMOS-MIM TFSI, Figure 3a) an ionic liquid with its cation functionalized by a trimethoxysilane group. Niedziolka-Jonsson et al. incorporated TMOS-MIM TFSI into an interesting electrodeposition approach wherein the ionic liquid was dispersed in an organic phase beneath a separate TMOS-containing aqueous phase (Figure 3b). Electrodeposition occurred at the substrate/aqueous/organic interface as the substrate was slowly withdrawn through the interface, generating composite films with thickness of 4 to 15 nm. The TFSI anions in the deposited layer were exchanged with hexacyanoferrate to give the functional layer redox activity. The density of MIM functional groups was estimated to be about 1.2 molecules per nm^2 [138]. Szot et al. used TMOS-MIM TFSI and TEOS sol in a layer-by-layer assembly method (Figure 3c) [137]. The imide anion was exchanged for sulfonated carbon particles that were themselves a substrate for the immobilization of a mediator, ABTS.

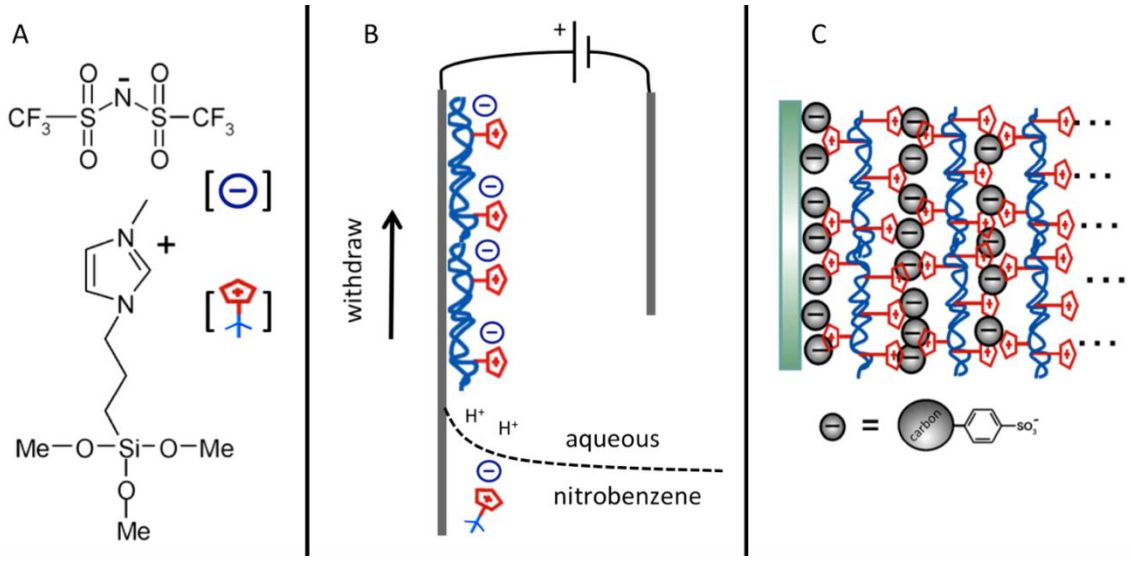

Fig. 3 Development of TMOS-MIM TFSI materials; (A) Skeletal formula of TMOS-MIM TFSI (B) Nanoscale films of imidazolium-functionalized sol-gel films prepared by electrochemically assisted deposition of TMOS-MIM TFSI at the interface between an aqueous and an organic phase [138] (C) Layer by layer assembly of TMOS-MIM TFSI with the bis(trifluoromethyl-sulfonyl)imide anions exchanged for functionalized carbon nanoparticles [137]

3.2 Proton Exchange Membrane Fuel Cells

Both hydrogen and methanol fuel cell technologies rely on a proton exchange membrane (PEM) to separate fuel and oxidant. Currently Nafion®, a family of sulfonated fluoropolymers, is the leading material for PEM applications. One of the principal disadvantages for Nafion in hydrogen fuel cell applications is that the membrane dehydrates and thereby loses its proton conductivity at temperatures above 90°C. In methanol fuel cell applications, Nafion has high methanol permeability, which leads to poor efficiency and catalyst poisoning. Sol-gel methods are employed to fabricate organic/inorganic hybrid membranes both from the bottom-up and by modifying commercial membranes. In general, sol-gel synthesis can be used to fabricate

hydrogen fuel cell (HFC) membranes with improved high temperature hydration properties, and direct methanol fuel cell (DMFC) membranes with improved proton selectivity [129]. Proton selectivity is defined as the ratio of the proton conductivity divided by methanol permeability [139].

In 1989, Mauritz et al. demonstrated that Nafion membranes have polar clusters, which are micropores that can be modified with silica via reaction with TEOS sol [140]. By filling these pores with properly-sized sol-gel structures, the movement of larger methanol molecules can be restricted with only minor decreases in proton conductivity. Numerous groups have taken this approach for modifying Nafion membranes. The membranes are typically treated with hydrogen peroxide and sulfuric acid in preparation for functionalization by sol-gel chemistry. Recently, Ladewig et al. tested a variety of mercaptopropyl and methyl modified ethoxysilanes for the modification of Nafion membranes for methanol fuel cells. They found that the membrane modified by (3-mercaptopropyl) methyldimethoxysilane in particular had methanol permeability about an order of magnitude lower than untreated Nafion, with only a modest decrease in proton conductivity. The result was a membrane with a proton selectivity that was three times higher than as-received Nafion [139].

The sol-gel process offers broader applications than simply modifying commercially available membranes. There is growing interest in making composite membranes that couple the flexibility of organic polymers with the mechanical and thermal stability of inorganics. Di Vona et al. prepared membranes of sulfonated poly(ether ether ketone) (s-PEEK) mixed with a titanium butoxide non-hydrolytic sol prepared in either pyridine or 2,4-pentanedione [141]. The polymer/sol mixture was cast to form membranes with 5 wt% TiO_2 and activated by treatment in sulfuric acid. Compared to a pure SPEEK membrane, the composite membranes showed

improved thermal stability and hydration properties. While pure SPEEK dissolves in water after one hour, the two composite membranes were water stable and reached hydration limits of 9 and 26 water molecules per sulfonic group, respectively. In a similar approach, Tsai et al. prepared sulfonated poly(arylene ether sulfone) and combined it with a silica sol to obtain composite membranes. At 80°C the hybrid membranes yielded single cell power densities between 11 and 13 mW/cm^2 in a DMFC, exceeding the power density of Nafion 117 [142].

Organic/inorganic composite membranes were also prepared with boron phosphate (BPO) as the inorganic component [143, 144]. PEEK and poly(ether sulfone) were used as the organic components, sulfonated and combined with a BPO solution prepared from tripropylborate and phosphoric acid. Deng et al. observed an improvement in thermal and oxidative stability with increasing BPO content in the BPO/s-PEEK membranes, but also observed some decrease in tensile strength. In addition, at 140°C the proton conductivity of the 40% BPO membrane exceeded that of Nafion 112.

Phosphoric acid is an interesting dopant because it is amphoteric, having both proton-donating and proton-accepting groups, which allows for dynamic hydrogen bonding. Furthermore, this acid has good thermal stability and low vapor pressure [145]. As early as the 1960s, researchers were able to operate fuel cells with phosphoric acid electrolytes at temperatures up to 150°C [146]. More recently, Mader et al. and Xiao et al. were able to introduce phosphoric acid (PA) doping into sulfonated polybenzimidazoles (s-PBI) via a solution-to-gel transition brought about via phase separation. In this method, PBI is dissolved into polyphosphoric acid (PPA), which absorbs ambient water and hydrolyzes to form PA. PBI is insoluble in phosphoric acid and thereby phase separates, forming a PBI phase with trapped PA [147, 148]. Whereas Nafion is reliant on gas stream humidification and is therefore not effective

in HFC applications above 90°C [127] the PBI method was used to fabricate an HFC membrane that operated (Figure 4) for over 1000 h at 160°C without any feed-gas humidification, yielding an areal power density of 240 mW/cm^2 [147].

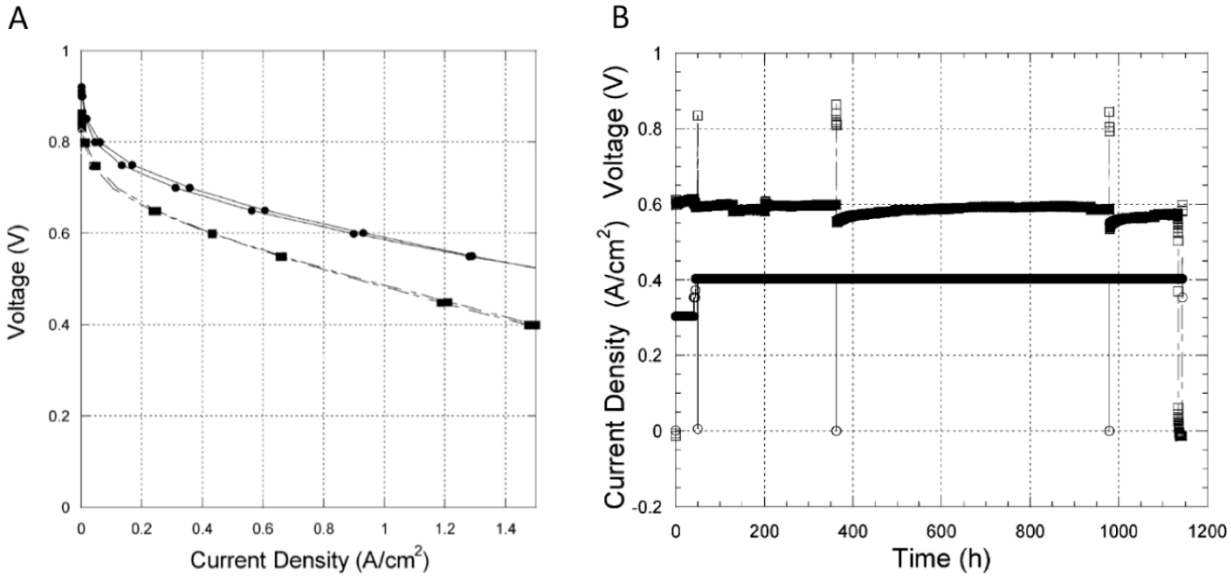

Fig. 4 Experimental data for a fuel cell with a PBI membrane doped by PA at a molar ratio of 32 mol PA per mole of PBI. Both electrodes used platinum catalysts with a loading of 1.0 mg/cm^2. (A) Current vs. voltage curves for the cell using both H_2/air (squares) and H_2/O_2 (circles) operating at 160°C without any feed gas humidification. (B) Long-term performance of cell voltage (top curve) and current (lower curve) over >1000 hours. Reprinted with permission from [147]. Copyright 2005 American Chemical Society

3.3 Redox Flow Batteries

In a redox flow battery (RFB), an ion-exchange membrane separates two tanks containing redox-active solute in electrolyte, which are referred to as catholyte and anolyte. The all-vanadium RFB is widely investigated and has seen some commercial development [128]. The chemistry of the all-vanadium RFB is shown in Figure 5. The anolyte is a mixture of soluble

vanadium cations, V(II)/V(III) and the catholyte is a mixture of V(IV)/V(V). The vanadium cations form a variety of complexes with anions such as SO_4^{2-} and HSO_4^-, with the exact composition dependent on the concentration of sulfuric acid [149].

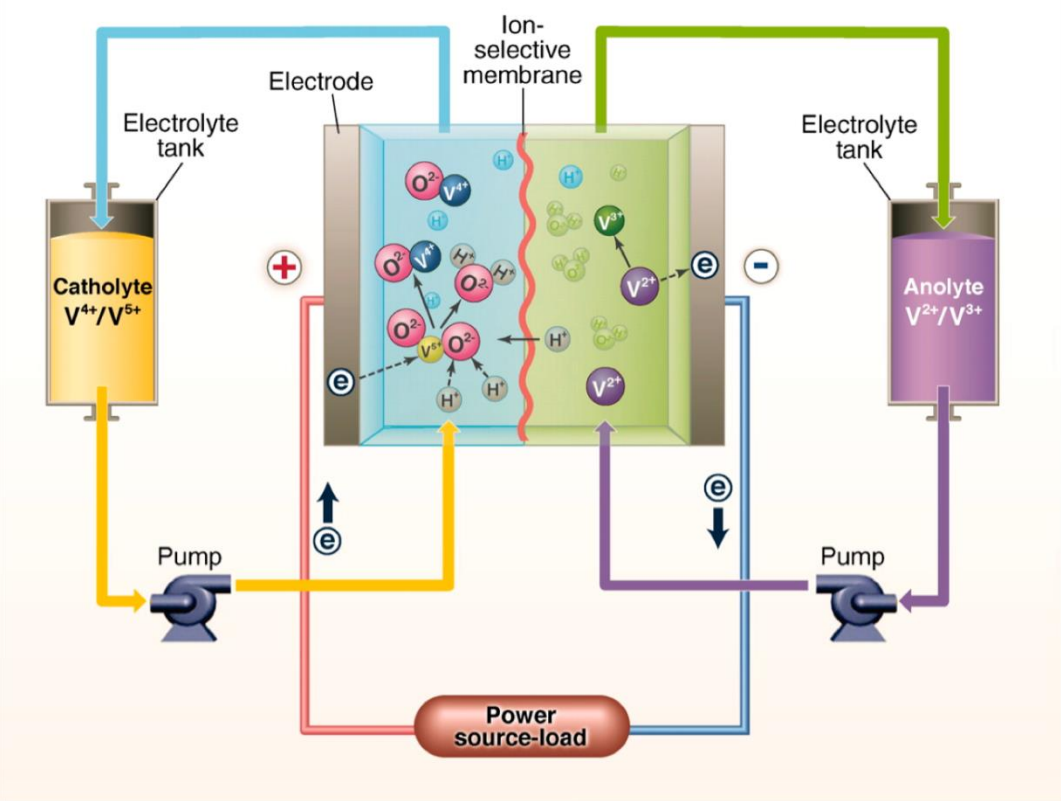

Fig. 5 Schematic of an all-vanadium redox-flow battery undergoing discharge. Two tanks containing soluble vanadium species in sulfuric acid electrolyte are separated by an ion-selective membrane. As the system discharges, electrons move through the external circuit and protons cross the membrane to maintain charge balance. Pumps are used to keep the electrolyte solutions well-mixed. Adapted from [109]

During RFB operation, oxidation/reduction reactions occur in both electrolytes. A membrane is needed to allow proton diffusion between the electrolytes in order to maintain charge neutrality. For the all-vanadium system, cross-over of vanadium ions results in self-discharge and low columbic efficiency. Other types of RFB, such as the vanadium/bromide battery, have different redox species in each electrolyte. In this case cross-over of active species is even more deleterious because as the ions mix, the charge storage ability of both electrolytes is permanently degraded. Therefore ion selectivity is of primary importance for RFB membranes [128]. In addition, the membranes must have chemical resistance to the acidic electrolyte solutions employed in RFB.

Not surprisingly, Nafion is widely used in RFB applications and a number of studies have shown that the performance of Nafion membranes in RFB can be improved via sol-gel functionalization. Xi et al. showed that sol-gel functionalization of Nafion's polar clusters restricts the movement of vanadium ions through the membrane. The permeability of Nafion 117 membranes to vandadium ions of several valences was decreased by a factor of four via functionalization in a silica sol. This was accompanied by only a 4% decrease in proton conductivity [150]. Similarily, Teng et al. achieved an 8-fold decrease in VO^{2+} permeability with only a 9% decrease in proton conductivity for Nafion 117 modified using a sol of dimethylsiloxane and tetrabutyl titanate [151]. Schulte used a TEOS/diethoxydimethylsilane sol to modify Nafion membranes, and found that addition of ammonia to the sol improved the resistance to vanadium permeation [152]. The improvement could be explained by the preference for base-catalyzed sol-gels to form particles that are more spherical rather than branched. In more recent work by Teng et al., all-vanadium test cells were constructed in which sulfonated diphenyldimethoxysilane was used to functionalize Nafion. During galvanostatic charge and

discharge at 70 mA/cm^2, the cells with the functionalized membranes had nearly twice the capacity compared to the cells with as-received Nafion. The functionalized membranes also gave significantly higher capacities at lower current densities, and lower self-discharge [153].

4. **Sol-gel encapsulation for battery and capacitor electrolytes**

The increased demand for mobile energy has stimulated a significant amount of research directed at improving energy storage technologies. Electrochemical energy storage is the most widely used means of storing energy with applications ranging from portable electronics to hybrid vehicles. Batteries are, without question, the most pervasive form of electrochemical energy storage, although electrochemical capacitors are finding an increasing number of applications because of higher power capabilities and faster kinetics. Electrochemical capacitors and batteries have similar device configurations in that two electrodes are immersed in an electrolyte, however, they use different energy storage mechanisms. Electrochemical capacitors store charge on the surface of their electrodes immersed in electrolyte in what is known as the electric double layer [7]. In contrast, batteries use chemical reactions between their cathodes and anodes to store energy [154]. It is well recognized that advances in these two technologies are strongly dependent on improvements in materials. For this reason, sol-gel chemistry has been widely used in the field because of its benefits in materials synthesis, both for bulk materials and thin films, as well as for large-scale manufacturing.

The sol-gel process is widely used for the synthesis of battery electrode materials. The application of sol-gel synthesis to the most common electrode materials for lithium-ion batteries was reviewed in the literature [155, 156]. The ability to fabricate high voltage oxides is particularly important for increased energy densities. Moreover, the ability of the sol-gel process to control phase and particle size is of substantial benefit for electrode fabrication.

The present paper considers another unique feature of the sol-gel process, the ability to encapsulate electrolytes. The advantage with sol-gel encapsulation is that the development of an interconnected porous network effectively holds the electrolyte by capillary forces. The resulting

‘quasi-solid’ electrolyte offers mechanical stability without compromising the conductivity of the electrolyte. Confining the liquid phase within the continuous mesoscale porosity of the sol-gel derived matrix enables the material to become solid-like in its appearance and develop mechanical integrity. While solid electrolytes provide the same mechanical integrity, an encapsulated electrolyte made with interconnected porosity can achieve far higher ionic conductivities [33, 157]. The challenge in synthesizing encapsulated electrolytes is to synthesize the material without reducing its ionic conductivity or voltage window.

The electrochemical voltage window is fundamental to maintaining the energy density of energy storage devices. For both batteries and capacitors, energy storage is dependent on voltage. Organic electrolytes are used in lithium ion batteries and electrochemical capacitors because of their 3 to 4V electrochemical window. High water content in the electrolyte will reduce the voltage window because of the electrolysis of water [29]. Minimizing water content is one reason why non-hydrolytic sol-gel routes are promising for encapsulating electrolytes.

Organic electrolytes can be encapsulated by sol-gel methods, however, it is evident that the encapsulation of ionic liquids will become far more significant because these liquids possess properties that make them more desirable as an encapsulated electrolyte. Ionic liquids are solvent free room temperature molten salts with moderate ionic conductivity and very low electronic conductivities. Ionic liquids are nonflammable alternatives to organic electrolytes that can deliver larger voltage windows and improved thermal properties. Moreover, when ionic liquids are encapsulated in an interconnected sol-gel network, these “ionogels” maintain the majority of their ionic conductivity [158]. Ionogels have a low vapor pressure and high thermal stability which allows them to be used as high temperature electrolytes in applications where an organic electrolyte would require additional cooling to prevent solvent evaporation [159]. Ionogels are

also appealing for lithium ion battery applications, because they can dissolve lithium salts [160] and some types of ionic liquids are stable against metallic lithium which makes them useful for lithium metal battery electrolytes [161].

Sol-gel morphology and ionic conductivity are interrelated. Higher ionic liquid content will increase the pore volume and ionic conductivity of the ionogels [35]. There are also reports that the average pore diameter becomes larger with increasing ionic liquid content [162]. For smaller pore sizes, non-silica sol precursors such as tin chloride can be used to make ionogels with nanometer pore sizes [163]. It is of interest to have nanometer pores since the ionic liquids can have improved conductivity as the pore size approaches the dimension of the ionic liquid ions [164].

5. Encapsulation of ionic liquids for solid state electrolytes

We have been investigating the use of ionogels as solid electrolytes for electrochemical capacitors following the reports of ionogels being used in both electrochemical capacitors [137] and lithium ion batteries [165]. The advantage here is that energy storage in the capacitor depends on the formation of a double layer. Thus, there must be mobile ions but, in contrast to a battery, the specific ions are not significant although their size and mobility are certainly important [166]. For this reason we used the ionic liquid 1-butyl-3-methylimidazolium tetrafluoroborate (BMIM BF_4) which is conductive and reasonable stable in ambient conditions [29]. In this way, it is possible to consider the prospect of developing an air-stable electrolyte. In carrying out this work, we have been concerned with the fact that ionic liquids can catalyze the hydrolysis or condensation of the sol-gel reaction depending on the type of ionic liquid and its concentration relative to the amount of the silica precursor [167]. In the paragraphs below, we

briefly review our synthesis efforts towards developing a stable, conductive ionogel as a solid-state electrolyte for capacitive energy storage. In addition to investigating various compositions, we also considered the hydrolysis temperature and hydrolysis time when performing test on the sol with and without the ionic liquid.

5.1 Experimental

All the chemicals were purchased from Sigma-Aldrich and used as received. The hygroscopic ionic liquid 1-butyl-3-methylimidazolium tetrafluoroborate was stored in an argon-filled glovebox to minimize exposure to moisture. Sol-gel reactions were magnetically stirred and performed in a fume hood using borosilicate glassware heated in a silicon oil bath. In the heated glassware, combinations of the silica precursors TMOS, TEOS, vinyltrimethoxysilane (VTMOS) and vinyltriethoxysilane (VTEOS) were mixed together prior to the fast addition by pipet of 98% formic acid (FA) to form the sol. Hydrolysis continued for 20 to 80 minutes decreasing with increasing hydrolysis temperature. Hydrolysis temperature of 22, 39 and 60 °C were tested with the gelation temperature of 22 °C. The sol was then pipetted into a glass vial at room temperature. The as-pipetted gels were transparent and their physical structure was assessed in the vial after a night in the fume hood to finish the condensation step. For later tests, ionic liquid was immediately added after pipetting the sol into the glass vial at room temperature. Ionic liquid concentration in the ionogel was constant at 42% of the total precursor volume.

To characterize the morphology of the silica network of the ionogel, we removed the ionic liquid component of the ionogel and then analyzed the resulting silicate network. To do this, the ionogel was pipetted into polyethylene vials that were left overnight in the fume hood. The next day the vial was cut away from the ionogel by blade. The removal of ionic liquid was

accomplished by immersing the ionogel in excess acetone to perform a solvent exchange The acetone-filled gel was then solvent exchanged with liquid CO_2, which in turn, was removed by supercritical drying leaving behind the silicate network. The morphology of the resulting silicate structure was characterized by gas adsorption (Micromeritics ASAP 2010).

Ionogel conductivity was determined using an HP 4284A LCR impedance analyzer at ambient conditions. The frequency range was 20 Hz to 1 MHz with an rms peak voltage of 13 mV. The ionogel was formed between 1 cm^2 electrodes of 304 stainless steel by drop casting 40 µm of ionogel on one electrode, allowing it to finish condensing overnight, then adding additional ionogel and the top electrode. The thickness of these cells was measured by caliper. For one ionogel sample, 120 µm of teflon tape was used as a spacer to fix the ionogel thickness between the stainless steel electrodes. Nickel wires were added to the stainless steel by pressing the wire with tape. Prior to impedance testing, the devices were heated for 30 minutes at 90 °C, followed by 60 additional minutes at the same temperature under vacuum.

5.2 Results and discussion

The sol-gel system we selected uses TMOS and VTEOS as silica precursors and formic acid (FA) for hydrolysis. This selection was motivated from work in the literature using non hydrolytic sol-gel routes of TMOS:FA [34] and methyltrimethoxysilane, TEOS and FA [35]. The initial TMOS gels were prone to cracking so VTEOS was added since the vinyl groups provide additional flexibility in organically modified gels [168]. These initial tests focused on the silica gels in preparation for making ionogels. Binary combinations of TMOS/TEOS combined with VTEOS/VTMOS were tested based on their physical appearance. Gel compositions ranging from

2:2:4 to 2:2:8 (by volume) for TMOS:VTEOS:FA were found to form crack free gels depending on the hydrolysis time and temperature.

Our synthesis experiments were directed at finding a suitable sol-gel chemistry for making transparent crack free gels with BMIM BF_4. Equal volumes of TMOS and VTEOS consistently formed transparent gels so they were systematically investigated while varying the hydrolysis time and the hydrolysis temperature before the addition of ionic liquid. These two parameters were selected because catalytic activity of the ionic liquid using BMIM BF_4 promotes condensation, so the gel needs to be fully hydrolyzed but not yet condensed when the ionic liquid is added. Hydrolysis temperature was varied in an attempt to make interconnected structures with larger pore volume and larger average pore size. Such morphology would have less tortuosity and higher ionic conductivity. We found that for specific hydrolysis times, crack free gels could be prepared at each of the hydrolysis temperatures. These crack free sols were then used as a basis for the ionogel study.

The study of the ionogel formation focused on the gels with low FA volume ratios. The BMIM BF_4 is very efficient at promoting condensation so slowing down the rate of condensation, by using less FA, proved useful. A ratio of 2:2:4 was first tested and transparent crack free gels were obtained at hydrolysis time ranges of 75 to 90 minutes, 35 to 50 minutes, 15 to 25 minutes for 22 °C, 39 °C and 60 °C respectively. There was a consistent observation of final ionogel morphology that correlates with the degree of hydrolysis. At the shortest hydrolysis times, semi-transparent precipitates were observed in the ionogel. At later hydrolysis times, the structure progressed from a dense white opaque ionogel, to a transparent ionogel with cracks, then to a transparent ionogel without cracks and finally to fully cleaved transparent ionogel. The

transparent ionogels without cracks were then characterized by gas adsorption analysis and impedance measurements.

The data in Table 2 show the effect of processing conditions on morphology for ionogels whose silicate network is comprised of TMOS:VTEOS:FA ratio of 2:2:4.When prepared at room temperature, the surface area, pore size and pore volume are reduced with longer ionic liquid addition times. This behavior is consistent with reports that the TMOS:FA system (without ionic liquid) produces dense gels [34]. Increasing the synthesis temperature tends to decrease the average pore volume. A fine tuning of the FA was performed which led to the 2:2:5 volume ratio ionogel that has the largest average pore diameter and total pore volume of the tested ionogels. These large pores and additional volume allow the 2:2:5 gels to be heated to over 100 °C without cracking unlike the 2:2:4 gels, that crack under the same conditions.

Table 2 Nitrogen gas adsorption results to characterize the morphology of the super critically dried silica aerogels network within ionogels prepared under different processing conditions

Volume Ratios			Hydrolysis	Hydrolysis	BET	Total	Average
TMOS:	VTEOS:	FA	Temperature (°C)	Time (m)	Surface Area (m^2/g)	Pore Volume (cm^3/g)	Pore Diameter (nm)
2	2	4	21	85	769 ± 14	2.39	12.4 ± 0.2
2	2	4	21	95	715 ± 13	1.98	11.1 ± 0.2
2	2	4	39	25	676 ± 10	2.29	13.6 ± 0.2
2	2	4	60	20	735 ± 4	1.63	8.9 ± 0.1
2	2	5	39	20	560 ± 9	2.57	18.4 ± 0.3

Figure 6 shows the impedance results for ionogel materials prepared using some of the processing conditions indicated in Table 2. In general, the impedance spectra are exactly as expected for an ionically conducting sample with blocking electrodes, as the phase angle approaches 90°. Fitting of these results to a Randles circuit yields the bulk resistances used to calculate the conductivities. For the most part, the conductivities are comparable with each other. For the 2:2:4 volume ratio cells, the conductivities range from about 0.11-0.44 mS/cm. The 2:2:5 ionogel has a measured conductivity of 0.66 mS/cm that is consistent with the literature value of 1.4 mS/cm measured for the neat ionic liquid [20]. While there is some decrease in conductivity, it is evident that the ionogel approach preserves the majority of the conductivity. Ionogels with higher loadings of ionic liquid may have further improved conductivity.

In the work shown here, we find that increasing the hydrolysis temperature and optimizing the FA volume ratio to the silica precursors increases the ionic conductivity of the ionogel. The hydrolysis time greatly controls the morphology of the gel and the duration has a large effect on the pore volume and ionic conductivity.

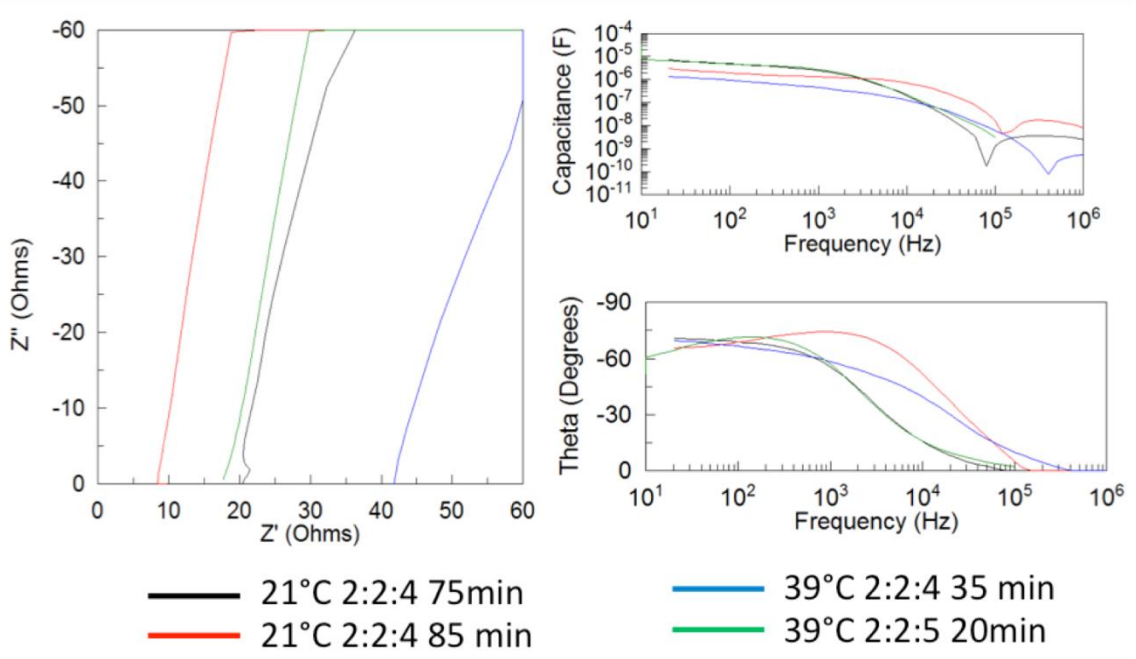

Fig. 6 Impedance of ionogel monoliths of various compositions; A) Complex plane representation; B) Double layer capacitance for an ionogel sandwiched between two stainless steel electrodes; C) Phase angle dependence on frequency.

Conclusions

In this paper we have reviewed a number of technological applications related to energy generation and storage where sol-gel chemistry has had a significant role. Our focus has been on identifying sol-gel approaches for electrolytes and separators where functionalization and encapsulation have resulted in creating new materials and architectures. Though silica gels are widely applied, each technology has required different routes to achieve improved properties. For example, in the case of DSSCs, organic/inorganic systems were developed to improve the solubility of the iodine component in order to increase the conductivity of the electrolyte. With

PEM fuel cells, the goal of improved proton selectivity was accomplished by functionalizing commercial membranes to achieve appropriate surface chemistry. The use of organic/inorganic strategies was also utilized with PEM fuel cells, although in this case the objective was to achieve higher temperature operation, which was accomplished through careful design of the inorganic component. In the case of secondary batteries, we emphasized the development of sol-gel encapsulated electrolytes. The encapsulation of ionic liquids is clearly emerging as an important direction because many of the outstanding properties of ionic liquids, especially in terms of electrochemical and thermal stability, are retained in the encapsulated electrolyte. The resulting ionogel materials are 'quasi-solid' electrolytes in that they offer the mechanical integrity of an inorganic solid electrolyte but with the ion transport properties of a liquid electrolyte. This unique combination of properties is enabled by tailoring the sol-gel process to achieve the appropriate microstructure. These examples underscore the importance of sol-gel chemistry in the design of materials and architectures for a wide variety of applications related to energy generation and storage. With its inherent flexibility, we expect that the sol-gel field will continue to make important contributions to these areas in the foreseeable future.

Acknowledgements

The authors acknowledge the support of the FENA Focus Center, one of six research centers funded under the Focus Center Research Program (FCRP), a Semiconductor Research Corporation entity. The authors also acknowledge the support from the following NSF IGERT Programs: Materials Creation Training Program; DGE-0654431 (DM) and NSF Clean Green IGERT; DGE-0903720 (LS). The authors greatly appreciate the support of this research by the Office of Naval Research.

Appendix 2

Appendix 2 lists tables with the cyclic voltammetry peak positions and magnitudes for the redox molecules in their two solvents on two different substrates described in chapter 4. The tables have the scan rate υ, The oxidation voltage V_{ox}, the reduction voltage V_{red}, the difference between the oxidation and reduction voltage ΔV, the oxidation current I_{ox}, the reduction current I_{red} and the ratio of the oxidation current to the reduction current I_{ox} / I_{red}. The voltages are all relative to platinum foil electrodes.

υ(mV/s)	V_{ox} (V)	V_{red} (V)	ΔV (mV)	I_{ox} (A)	I_{red} (A)	I_{ox} / I_{red}
Cobaltocene in ACN on Platinum						
200	0.15	0.05	101	1.12E-03	9.86E-04	1.14
250	0.15	0.04	112	1.22E-03	1.12E-03	1.09
300	0.16	0.04	123	1.33E-03	1.23E-03	1.08
350	0.15	0.03	121	1.44E-03	1.31E-03	1.10
400	0.16	0.03	129	1.52E-03	1.41E-03	1.07
450	0.16	0.02	134	1.62E-03	1.47E-03	1.10
500	0.16	0.02	135	1.67E-03	1.57E-03	1.07
550	0.16	0.02	137	1.77E-03	1.62E-03	1.09
600	0.16	0.02	144	1.84E-03	1.68E-03	1.10
650	0.16	0.02	144	1.92E-03	1.74E-03	1.10
700	0.16	0.02	143	1.98E-03	1.80E-03	1.10
Cobaltocene in ACN on ITO						
200	0.34	-0.08	421	2.79E-04	3.08E-04	0.91
250	0.35	-0.10	448	2.99E-04	3.45E-04	0.87
300	0.36	-0.10	460	3.20E-04	3.76E-04	0.85
350	0.37	-0.11	480	3.50E-04	3.91E-04	0.90
400	0.38	-0.11	492	3.65E-04	4.17E-04	0.88
450	0.39	-0.12	514	3.94E-04	4.27E-04	0.92
500	0.40	-0.13	526	4.02E-04	4.54E-04	0.89
550	0.41	-0.13	538	4.28E-04	4.60E-04	0.93
600	0.42	-0.14	557	4.46E-04	4.74E-04	0.94
650	0.42	-0.14	565	4.63E-04	4.88E-04	0.95
700	1.04	0.04	991	1.43E-04	1.36E-04	1.05

υ(mV/s)	V_{ox} (V)	V_{red} (V)	ΔV (mV)	I_{ox} (A)	I_{red} (A)	I_{ox} / I_{red}
Cobaltocenium in ACN on Platinum						
200	-0.22	-0.35	128	1.19E-03	1.40E-03	0.85
250	-0.21	-0.35	134	1.37E-03	1.51E-03	0.91
300	-0.21	-0.35	139	1.52E-03	1.62E-03	0.94
350	-0.20	-0.35	147	1.56E-03	1.77E-03	0.88
400	-0.20	-0.35	151	1.72E-03	1.83E-03	0.94
450	-0.19	-0.34	153	1.76E-03	1.96E-03	0.90
500	-0.19	-0.35	158	1.92E-03	2.00E-03	0.96
550	-0.18	-0.34	160	1.93E-03	2.12E-03	0.91
600	-0.16	-0.33	162	2.01E-03	2.19E-03	0.92
650	-0.15	-0.31	160	2.10E-03	2.25E-03	0.94
700	-0.14	-0.30	167	2.18E-03	2.30E-03	0.95
Cobaltocenium in ACN on ITO						
200	-0.15	-0.34	190	3.59E-04	4.34E-04	0.83
250	-0.14	-0.34	195	4.00E-04	4.57E-04	0.88
300	-0.14	-0.35	204	4.34E-04	4.84E-04	0.90
350	-0.13	-0.35	217	4.41E-04	5.30E-04	0.83
400	-0.13	-0.35	224	4.83E-04	5.36E-04	0.90
450	-0.09	-0.33	239	4.93E-04	5.61E-04	0.88
500	-0.07	-0.32	241	5.35E-04	5.66E-04	0.95
550	-0.06	-0.32	256	5.35E-04	6.30E-04	0.85
600	-0.04	-0.30	266	5.57E-04	6.43E-04	0.87
650	-0.02	-0.29	274	5.76E-04	6.57E-04	0.88
700	-0.01	-0.29	285	5.94E-04	6.71E-04	0.88

υ(mV/s)	V_{ox} (V)	V_{red} (V)	ΔV (mV)	I_{ox} (A)	I_{red} (A)	I_{ox} / I_{red}
Decamethyl Ferrocene in ACN on Platinum						
200	0.29	0.19	101	1.02E-03	9.28E-04	1.10
250	0.29	0.18	114	1.13E-03	1.04E-03	1.08
300	0.28	0.16	124	1.21E-03	1.15E-03	1.05
350	0.25	0.14	112	1.30E-03	1.23E-03	1.06
400	0.25	0.14	115	1.36E-03	1.32E-03	1.03
450	0.24	0.12	116	1.40E-03	1.34E-03	1.04
500	0.23	0.11	120	1.42E-03	1.44E-03	0.99
550	0.21	0.09	120	1.55E-03	1.54E-03	1.00
600	0.23	0.10	126	1.65E-03	1.60E-03	1.03
650	0.21	0.09	125	1.73E-03	1.66E-03	1.04
700	0.21	0.08	132	1.79E-03	1.72E-03	1.04
Decamethyl Ferrocene in ACN on ITO						
200	0.32	0.04	283	3.39E-04	2.95E-04	1.15
250	0.33	0.03	303	3.63E-04	3.34E-04	1.09
300	0.33	0.02	311	3.88E-04	3.66E-04	1.06
350	0.34	0.00	331	4.21E-04	3.86E-04	1.09
400	0.33	-0.01	338	4.39E-04	4.15E-04	1.06
450	0.30	-0.05	349	4.64E-04	4.35E-04	1.07
500	0.30	-0.06	357	4.74E-04	4.65E-04	1.02
550	0.31	-0.06	370	5.03E-04	4.75E-04	1.06
600	0.32	-0.06	377	5.26E-04	4.89E-04	1.08
650	0.33	-0.05	384	5.48E-04	5.02E-04	1.09
700	0.35	-0.05	398	5.70E-04	5.12E-04	1.11

υ(mV/s)	V_{ox} (V)	V_{red} (V)	ΔV (mV)	I_{ox} (A)	I_{red} (A)	I_{ox} / I_{red}
Ferrocene in ACN on Platinum						
100	0.68	0.56	128	9.49E-04	8.41E-04	1.13
150	0.53	0.39	136	1.12E-03	1.04E-03	1.08
200	0.47	0.43	39	1.25E-03	1.20E-03	1.04
250	0.75	0.67	74	1.43E-03	1.33E-03	1.07
300	0.79	0.66	130	1.59E-03	1.44E-03	1.11
350	0.55	0.42	127	1.64E-03	1.55E-03	1.06
400	0.57	0.46	108	1.70E-03	1.67E-03	1.02
450	0.74	0.61	128	1.89E-03	1.75E-03	1.08
500	0.79	0.66	124	2.00E-03	1.83E-03	1.09
Ferrocene in ACN on ITO						
1	0.12	0.01	109	2.75E-05	1.38E-05	1.99
5	0.10	0.02	79	5.49E-05	4.62E-05	1.19
10	0.10	0.01	91	8.09E-05	7.20E-05	1.12
20	0.11	0.01	100	1.16E-04	1.07E-04	1.09
50	0.12	0.00	113	1.79E-04	1.71E-04	1.05
100	0.12	-0.01	127	2.43E-04	2.36E-04	1.03
200	0.13	-0.01	143	3.26E-04	3.23E-04	1.01
500	0.14	-0.01	148	4.68E-04	4.59E-04	1.02
1000	0.15	-0.03	180	6.11E-04	6.24E-04	0.98

υ(mV/s)	V_{ox} (V)	V_{red} (V)	ΔV (mV)	I_{ox} (A)	I_{red} (A)	I_{ox} / I_{red}
Ferrocenium in ACN on Platinum						
200	-0.01	-0.11	103	1.05E-03	1.18E-03	0.89
250	-0.01	-0.11	106	1.18E-03	1.28E-03	0.92
300	0.00	-0.11	110	1.29E-03	1.39E-03	0.93
350	0.00	-0.11	116	1.38E-03	1.51E-03	0.92
400	0.00	-0.11	112	1.48E-03	1.58E-03	0.94
450	0.00	-0.12	118	1.54E-03	1.69E-03	0.91
500	0.01	-0.12	127	1.64E-03	1.75E-03	0.94
550	0.01	-0.12	127	1.70E-03	1.86E-03	0.91
600	0.01	-0.12	131	1.77E-03	1.93E-03	0.91
650	0.01	-0.12	129	1.84E-03	2.01E-03	0.92
700	0.02	-0.12	133	1.90E-03	2.07E-03	0.92
Ferrocenium in ACN on ITO						
200	0.07	-0.15	226	2.98E-04	4.26E-04	0.70
250	0.07	-0.15	229	3.35E-04	4.65E-04	0.72
300	0.08	-0.16	242	3.66E-04	5.03E-04	0.73
350	0.08	-0.16	244	3.89E-04	5.48E-04	0.71
400	0.09	-0.16	254	4.18E-04	5.77E-04	0.73
450	0.09	-0.17	256	4.37E-04	6.17E-04	0.71
500	0.10	-0.17	267	4.64E-04	6.40E-04	0.72
550	0.09	-0.17	264	4.78E-04	6.77E-04	0.71
600	0.10	-0.17	270	4.98E-04	7.07E-04	0.70
650	0.10	-0.17	274	5.16E-04	7.34E-04	0.70
700	0.10	-0.17	275	5.34E-04	7.60E-04	0.70

υ(mV/s)	V_{ox} (V)	V_{red} (V)	ΔV (mV)	I_{ox} (A)	I_{red} (A)	I_{ox} / I_{red}
Cobaltocene in PC on Platinum						
200	0.17	0.04	136	4.29E-04	3.81E-04	1.13
250	0.18	0.04	137	4.65E-04	4.31E-04	1.08
300	0.18	0.03	151	4.99E-04	4.72E-04	1.06
350	0.18	0.03	153	5.41E-04	4.95E-04	1.09
400	0.19	0.03	156	5.68E-04	5.31E-04	1.07
450	0.19	0.02	165	6.01E-04	5.53E-04	1.09
500	0.19	0.02	167	6.22E-04	5.87E-04	1.06
550	0.19	0.02	172	6.54E-04	6.05E-04	1.08
600	0.19	0.02	178	6.80E-04	6.27E-04	1.08
650	0.19	0.01	179	7.05E-04	6.50E-04	1.08
700	0.20	0.01	186	7.27E-04	6.71E-04	1.08
Cobaltocene in PC on ITO						
200	0.32	-0.11	426	1.12E-04	1.06E-04	1.06
250	0.33	-0.12	447	1.21E-04	1.16E-04	1.04
300	0.34	-0.13	471	1.30E-04	1.26E-04	1.03
350	0.35	-0.14	491	1.41E-04	1.31E-04	1.08
400	0.36	-0.15	511	1.47E-04	1.41E-04	1.04
450	0.37	-0.16	528	1.58E-04	1.45E-04	1.09
500	0.38	-0.16	539	1.62E-04	1.55E-04	1.05
550	0.38	-0.17	553	1.72E-04	1.58E-04	1.09
600	0.39	-0.18	565	1.79E-04	1.63E-04	1.10
650	0.39	-0.18	577	1.86E-04	1.68E-04	1.11
700	0.40	-0.18	580	1.92E-04	1.73E-04	1.11

υ(mV/s)	V_{ox} (V)	V_{red} (V)	ΔV (mV)	I_{ox} (A)	I_{red} (A)	I_{ox} / I_{red}
Cobaltocenium in PC on Platinum						
200	-0.23	-0.36	132	3.65E-04	4.06E-04	0.90
250	-0.23	-0.36	135	4.14E-04	4.42E-04	0.94
300	-0.22	-0.36	143	4.56E-04	4.77E-04	0.95
350	-0.21	-0.36	148	4.82E-04	5.13E-04	0.94
400	-0.20	-0.36	152	5.21E-04	5.38E-04	0.97
450	-0.20	-0.35	154	5.43E-04	5.70E-04	0.95
500	-0.19	-0.35	160	5.79E-04	5.92E-04	0.98
550	-0.19	-0.36	163	5.94E-04	6.23E-04	0.95
600	-0.19	-0.36	171	6.16E-04	6.48E-04	0.95
650	-0.18	-0.36	171	6.39E-04	6.72E-04	0.95
700	-0.18	-0.35	175	6.61E-04	6.92E-04	0.95
Cobaltocenium in PC on ITO						
200	-0.18	-0.43	245	9.87E-05	1.18E-04	0.84
250	-0.18	-0.44	264	1.11E-04	1.25E-04	0.89
300	-0.17	-0.45	273	1.20E-04	1.32E-04	0.91
350	-0.16	-0.45	288	1.25E-04	1.43E-04	0.88
400	-0.16	-0.45	292	1.35E-04	1.47E-04	0.92
450	-0.16	-0.46	303	1.39E-04	1.57E-04	0.88
500	-0.15	-0.46	311	1.47E-04	1.60E-04	0.92
550	-0.15	-0.47	319	1.50E-04	1.70E-04	0.88
600	-0.13	-0.46	325	1.56E-04	1.76E-04	0.89
650	-0.11	-0.44	331	1.64E-04	1.80E-04	0.91
700	-0.07	-0.41	338	1.71E-04	1.83E-04	0.94

υ(mV/s)	V_{ox} (V)	V_{red} (V)	ΔV (mV)	I_{ox} (A)	I_{red} (A)	I_{ox} / I_{red}
Decamethyl Ferrocene in PC on Platinum						
200	0.70	0.56	140	3.85E-04	3.57E-04	1.08
250	0.70	0.55	151	4.19E-04	3.99E-04	1.05
300	0.70	0.55	158	4.52E-04	4.36E-04	1.04
350	0.71	0.55	164	4.86E-04	4.60E-04	1.06
400	0.71	0.55	165	5.10E-04	4.92E-04	1.04
450	0.72	0.55	175	5.41E-04	5.12E-04	1.06
500	0.73	0.55	180	5.60E-04	5.40E-04	1.04
550	0.73	0.55	181	5.87E-04	5.57E-04	1.05
600	0.73	0.55	185	6.09E-04	5.75E-04	1.06
650	0.73	0.54	187	6.29E-04	5.95E-04	1.06
700	0.73	0.54	195	6.48E-04	6.13E-04	1.06
Decamethyl Ferrocene in PC on ITO						
200	0.98	0.18	799	8.31E-05	7.33E-05	1.13
250	0.99	0.17	818	9.12E-05	8.37E-05	1.09
300	0.99	0.16	832	9.88E-05	9.25E-05	1.07
350	1.01	0.15	865	1.07E-04	9.83E-05	1.08
400	1.02	0.14	885	1.12E-04	1.05E-04	1.06
450	1.03	0.12	908	1.19E-04	1.11E-04	1.07
500	1.03	0.11	918	1.23E-04	1.18E-04	1.04
550	1.04	0.09	947	1.29E-04	1.22E-04	1.06
600	1.03	0.07	961	1.34E-04	1.27E-04	1.06
650	1.03	0.05	979	1.39E-04	1.32E-04	1.05
700	1.04	0.04	991	1.43E-04	1.36E-04	1.05

υ(mV/s)	V_{ox} (V)	V_{red} (V)	ΔV (mV)	I_{ox} (A)	I_{red} (A)	I_{ox} / I_{red}
Ferrocene in PC on Platinum						
1	0.13	0.04	88	4.09E-05	2.61E-05	1.57
5	0.11	0.03	84	8.56E-05	7.22E-05	1.19
10	0.12	0.04	85	1.14E-04	1.02E-04	1.12
20	0.12	0.03	92	1.54E-04	1.43E-04	1.07
50	0.13	0.03	103	2.27E-04	2.19E-04	1.04
100	0.13	0.02	114	3.05E-04	3.00E-04	1.02
200	0.14	0.01	127	4.09E-04	4.07E-04	1.00
500	0.15	0.00	152	5.97E-04	6.01E-04	0.99
1000	0.17	0.00	164	7.89E-04	7.92E-04	1.00
Ferrocene in PC on ITO						
1	0.19	0.04	145	1.33E-05	8.51E-06	1.57
5	0.22	0.00	227	2.50E-05	2.02E-05	1.24
10	0.25	-0.03	280	3.22E-05	2.75E-05	1.17
20	0.27	-0.06	332	4.18E-05	3.72E-05	1.12
50	0.31	-0.10	416	5.91E-05	5.61E-05	1.05
100	0.35	-0.14	482	7.77E-05	7.64E-05	1.02
200	0.38	-0.18	559	1.02E-04	1.04E-04	0.99
500	0.44	-0.23	668	1.49E-04	1.56E-04	0.96
1000	0.49	-0.18	663	1.97E-04	1.80E-04	1.09

υ(mV/s)	V_{ox} (V)	V_{red} (V)	ΔV (mV)	I_{ox} (A)	I_{red} (A)	I_{ox} / I_{red}
Ferrocenium in PC on Platinum						
200	0.00	-0.10	101	4.06E-04	4.35E-04	0.93
250	0.00	-0.10	99	4.55E-04	4.76E-04	0.95
300	0.00	-0.11	111	4.98E-04	5.18E-04	0.96
350	0.01	-0.11	113	5.33E-04	5.59E-04	0.95
400	0.01	-0.11	115	5.71E-04	5.90E-04	0.97
450	0.01	-0.11	120	5.99E-04	6.27E-04	0.96
500	0.01	-0.11	120	6.32E-04	6.53E-04	0.97
550	0.01	-0.12	128	6.56E-04	6.87E-04	0.95
600	0.01	-0.12	133	6.82E-04	7.17E-04	0.95
650	0.01	-0.12	133	7.08E-04	7.45E-04	0.95
700	0.02	-0.12	135	7.32E-04	7.71E-04	0.95
Ferrocenium in PC on ITO						
200	0.16	-0.22	382	8.37E-05	1.28E-04	200
250	0.18	-0.23	408	9.64E-05	1.38E-04	250
300	0.19	-0.23	418	1.06E-04	1.48E-04	300
350	0.19	-0.23	426	1.12E-04	1.61E-04	350
400	0.19	-0.24	432	1.22E-04	1.69E-04	400
450	0.20	-0.24	443	1.27E-04	1.80E-04	450
500	0.21	-0.24	451	1.35E-04	1.86E-04	500
550	0.21	-0.24	451	1.39E-04	1.97E-04	550
600	0.21	-0.25	459	1.45E-04	2.05E-04	600
650	0.21	-0.25	467	1.50E-04	2.14E-04	650
700	0.22	-0.25	475	1.55E-04	2.21E-04	700

References

1. Simon P, Gogotsi Y (2008) Materials for electrochemical capacitors. Nat Mater 845–854.
2. Miller JR (2012) Valuing reversible energy storage. Science 335:1312–3. doi: 10.1126/science.1219134
3. Naoi K, Simon P (2008) New materials and new configurations for advanced electrochemical capacitors. J Electrochem Soc Interface 17:34–37.
4. Izadi-Najafabadi A, Yasuda S, Kobashi K, et al. (2010) Extracting the full potential of single-walled carbon nanotubes as durable supercapacitor electrodes operable at 4 V with high power and energy density. Adv Mater 22:E235–41. doi: 10.1002/adma.200904349
5. Pech D, Brunet M, Durou H, et al. (2010) Ultrahigh-power micrometre-sized supercapacitors based on onion-like carbon. Nat Nanotechnol 5:651–4. doi: 10.1038/nnano.2010.162
6. El-Kady MF, Strong V, Dubin S, Kaner RB (2012) Laser scribing of high-performance and flexible graphene-based electrochemical capacitors. Science 335:1326–30. doi: 10.1126/science.1216744
7. Kotz R, Carlen M (2000) Principles and applications of electrochemical capacitors. Electrochim Acta 45:2483–2498.
8. Conway BE, Pell WG (2003) Double-layer and pseudocapacitance types of electrochemical capacitors and their applications to the development of hybrid devices. J Solid State Electrochem 7:637–644. doi: 10.1007/s10008-003-0395-7
9. Pech D, Brunet M, Taberna P-L, et al. (2010) Elaboration of a microstructured inkjet-printed carbon electrochemical capacitor. J Power Sources 195:1266–1269. doi: 10.1016/j.jpowsour.2009.08.085
10. Tassel J Van, Randall C (2004) Potential for integration of electrophoretic deposition into electronic device manufacture; demonstrations using silver/palladium. J Mater Sci 9:867–879.
11. Modi S, Wei M, Mead JL, Barry CMF (2011) Effect of Processing Parameters on the Electrophoretic Deposition of Carbon Black Nanoparticles in Moderately Viscous Systems. Langmuir 3166–3173. doi: 10.1021/la1043359
12. Simon P, Burke A (2008) Nanostructured carbons: double-layer capacitance and more. Electrochem Soc Interface 17:38–43.
13. Frackowiak E, Béguin F (2001) Carbon materials for the electrochemical storage of energy in capacitors. Carbon N Y 39:937–950. doi: 10.1016/S0008-6223(00)00183-4
14. Burke A (2000) Ultracapacitors: why, how, and where is the technology. J Power Sources 91:37–50. doi: 10.1016/S0378-7753(00)00485-7
15. Stoller M, Park S, Zhu Y, et al. (2008) Graphene-based ultracapacitors. Nano Lett 8:3498–3502.
16. Cho J, Konopka K, Rożniatowski K, et al. (2009) Characterisation of carbon nanotube films deposited by electrophoretic deposition. Carbon N Y 47:58–67. doi: 10.1016/j.carbon.2008.08.028
17. Du C, Pan N (2006) High power density supercapacitor electrodes of carbon nanotube films by electrophoretic deposition. Nanotechnology 17:5314–5318. doi: 10.1088/0957-4484/17/21/005
18. Qu D, Shi H (1998) Studies of activated carbons used in double-layer capacitors. J Power Sources 74:99–107. doi: 10.1016/S0378-7753(98)00038-X

19. Bard AJ, Faulkner LR (2001) Electrochemical Methods fundamentals and applications, 2nd ed. john Wiley and sons
20. Galinski M, Lewandowski A, Stepniak I (2006) Ionic liquids as electrolytes. Electrochim Acta 51:5567–5580. doi: 10.1016/j.electacta.2006.03.016
21. Signorelli R, Ku DC, Kassakian JG, Schindall JE (2009) Electrochemical Double-Layer Capacitors Using Carbon Nanotube Electrode Structures. Proc IEEE 97:1837–1847. doi: 10.1109/JPROC.2009.2030240
22. Kurig H, Jänes A, Lust E (2010) Electrochemical Characteristics of Carbide-Derived Carbon| 1-Ethyl-3-methylimidazolium Tetrafluoroborate Supercapacitor Cells. J Electrochem Soc 157:A272. doi: 10.1149/1.3274208
23. Gupta AK, Singh MP, Singh RK, Chandra S (2012) Low density ionogels obtained by rapid gellification of tetraethyl orthosilane assisted by ionic liquids. Dalton Trans 41:6263–71. doi: 10.1039/c2dt30318c
24. Gogotsi Y, Simon P (2011) Materials science. True performance metrics in electrochemical energy storage. Science 334:917–8. doi: 10.1126/science.1213003
25. Song J, Wang Y, Wan C (1999) Review of gel-type polymer electrolytes for lithium-ion batteries. J Power Sources 77:183–97.
26. Pandey GP, Hashmi S a. (2013) Ionic liquid 1-ethyl-3-methylimidazolium tetracyanoborate-based gel polymer electrolyte for electrochemical capacitors. J Mater Chem A 1:3372. doi: 10.1039/c2ta01347a
27. Pandey GP, Hashmi S a. (2013) Performance of solid-state supercapacitors with ionic liquid 1-ethyl-3-methylimidazolium tris(pentafluoroethyl) trifluorophosphate based gel polymer electrolyte and modified MWCNT electrodes. Electrochim Acta 105:333–341. doi: 10.1016/j.electacta.2013.05.018
28. Ignat'ev N, Welz-Biermann U (2005) New ionic liquids with tris (perfluoroalkyl) trifluorophosphate (FAP) anions. J Fluor Chem 126:1150–1159. doi: 10.1016/j.jfluchem.2005.04.017
29. O'Mahony A, Silvester D (2008) Effect of water on the electrochemical window and potential limits of room-temperature ionic liquids. J Chem Eng Data 53:2884–2891.
30. Jarosik A, Krajewski S (2006) Conductivity of ionic liquids in mixtures. J Mol Liq 123:43 – 50. doi: 10.1016/j.molliq.2005.06.001
31. Kang YJ, Chung H, Han C-H, Kim W (2012) All-solid-state flexible supercapacitors based on papers coated with carbon nanotubes and ionic-liquid-based gel electrolytes. Nanotechnology 23:289501. doi: 10.1088/0957-4484/23/28/289501
32. El-Kady MF, Kaner RB (2013) Scalable fabrication of high-power graphene micro-supercapacitors for flexible and on-chip energy storage. Nat Commun 4:1475. doi: 10.1038/ncomms2446
33. Morita M, Qiao J-L, Yoshimoto N, Ishikawa M (2004) Application of proton conducting polymeric electrolytes to electrochemical capacitors. Electrochim Acta 50:837–841. doi: 10.1016/j.electacta.2004.02.053
34. Sharp K (1994) A two-component, non-aqueous route to silica gel. J Sol-Gel Sci Technol 41:35–41.
35. Néouze M, Bideau J, Gaveau P, et al. (2006) Ionogels, new materials arising from the confinement of ionic liquids within silica-derived networks. Chem Mater 18:3931–3936.

36. Boccaccini a. R, Cho J, Subhani T, et al. (2010) Electrophoretic deposition of carbon nanotube–ceramic nanocomposites. J Eur Ceram Soc 30:1115–1129. doi: 10.1016/j.jeurceramsoc.2009.03.016
37. Chung J, Lee K-H, Lee J, Ruoff RS (2004) Toward large-scale integration of carbon nanotubes. Langmuir 20:3011–7.
38. Naieni a K, Nojeh a (2012) Effect of solution conductivity and electrode shape on the deposition of carbon nanotubes from solution using dielectrophoresis. Nanotechnology 23:495606. doi: 10.1088/0957-4484/23/49/495606
39. Chávez-Valdez A, Boccaccini AR (2012) Innovations in electrophoretic deposition: Alternating current and pulsed direct current methods. Electrochim Acta 65:70–89. doi: 10.1016/j.electacta.2012.01.015
40. Lee S, Yabuuchi N, Gallant B (2010) High-power lithium batteries from functionalized carbon-nanotube electrodes. Nat Nanotechnol 5:531–537. doi: 10.1038/nnano.2010.116
41. Stoller MD, Ruoff RS (2010) Best practice methods for determining an electrode material's performance for ultracapacitors. Energy Environ Sci 3:1294. doi: 10.1039/c0ee00074d
42. Kundu S, Wang Y, Xia W, Muhler M (2008) Thermal Stability and Reducibility of Oxygen-Containing Functional Groups on Multiwalled Carbon Nanotube Surfaces: A Quantitative High-Resolution XPS and TPD/TPR Study. J Phys Chem C 112:16869–16878. doi: 10.1021/jp804413a
43. Verdejo R, Lamoriniere S, Cottam B, et al. (2007) Removal of oxidation debris from multi-walled carbon nanotubes. Chem Commun (Camb) 513–5. doi: 10.1039/b611930a
44. An KH, Kim WS, Park YS, et al. (2001) Electrochemical properties of high-power supercapacitors using single-walled carbon nanotube electrodes. Adv Funct Mater 387–392.
45. Halper M, Ellenbogen J (2006) Supercapacitors: A brief overview. MITRE Nanosyst. Gr.
46. Lockett V, Horne M, Sedev R, et al. (2010) Differential capacitance of the double layer at the electrode/ionic liquids interface. Phys Chem Chem Phys 12:12499–512. doi: 10.1039/c0cp00170h
47. Drüschler M, Huber B, Passerini S, Roling B (2010) Hysteresis Effects in the Potential-Dependent Double Layer Capacitance of Room Temperature Ionic Liquids at a Polycrystalline Platinum Interface. J Phys Chem C 114:3614–3617. doi: 10.1021/jp911513k
48. Shen C, Wang X, Zhang W, Kang F (2011) A high-performance three-dimensional micro supercapacitor based on self-supporting composite materials. J Power Sources 196:10465–10471. doi: 10.1016/j.jpowsour.2011.08.007
49. Jiang YQ, Zhou Q, Lin L (2009) Planar MEMS Supercapacitor using Carbon Nanotube Forests. 2009 IEEE 22nd Int Conf Micro Electro Mech Syst 587–590. doi: 10.1109/MEMSYS.2009.4805450
50. Gujar TP, Shinde VR, Lokhande CD, Han S-H (2006) Electrosynthesis of Bi2O3 thin films and their use in electrochemical supercapacitors. J Power Sources 161:1479–1485. doi: 10.1016/j.jpowsour.2006.05.036
51. Lokhande CD, Dubal DP, Joo O-S (2011) Metal oxide thin film based supercapacitors. Curr Appl Phys 11:255–270. doi: 10.1016/j.cap.2010.12.001
52. Chen Z, Augustyn V, Jia X, et al. (2012) High-Performance Sodium-Ion Pseudocapacitors Based on Hierarchically Porous Nanowire Composites. ACS Nano 6:4319–4327.
53. Lee SW, Kim J, Chen S, et al. (2010) Carbon nanotube/manganese oxide ultrathin film electrodes for electrochemical capacitors. ACS Nano 4:3889–96. doi: 10.1021/nn100681d

54. Brezesinski T, Wang J, Tolbert SH, Dunn B (2010) Ordered mesoporous alpha-MoO3 with iso-oriented nanocrystalline walls for thin-film pseudocapacitors. Nat Mater 9:146–51. doi: 10.1038/nmat2612
55. Cheyns D, Kam B, Vasseur K, et al. (2013) Structure induced conductivity enhancement in metal-doped molybdenum oxide thin films. J Appl Phys 113:043109. doi: 10.1063/1.4789352
56. Kim JW, Augustyn V, Dunn B (2012) The Effect of Crystallinity on the Rapid Pseudocapacitive Response of Nb2O5. Adv Energy Mater 2:141–148. doi: 10.1002/aenm.201100494
57. Macek M, Orel B, Krašovec U (1997) The Effect of Lithiation on the Electrochromism of Sol- • Gel Derived Niobium Oxide Films. J Electrochem Soc 144:3002–3010.
58. Domingo J (1996) Vanadium: a review of the reproductive and developmental toxicity. Reprod Toxicol 10:175–182.
59. Augustyn V, Come J, Lowe M a., et al. (2013) High-rate electrochemical energy storage through Li+ intercalation pseudocapacitance. Nat Mater 12:1–5. doi: 10.1038/nmat3601
60. Romero R, Ramos-Barrado JR, Martin F, Leinen D (2004) Nb2O5 thin films obtained by chemical spray pyrolysis. Surf Interface Anal 36:888–891. doi: 10.1002/sia.1793
61. Cava R, Batlogg B, Krajewski J (1991) Electrical and magnetic properties of Nb_ {2} O_ {5-δ} crystallographic shear structures. Phys Rev B 44:6973–6981.
62. Mai LQ, Hu B, Chen W, et al. (2007) Lithiated MoO3 Nanobelts with Greatly Improved Performance for Lithium Batteries. Adv Mater 19:3712–3716. doi: 10.1002/adma.200700883
63. Pollak E, Salitra G, Baranchugov V, Aurbach D (2007) In Situ Conductivity, Impedance Spectroscopy, and Ex Situ Raman Spectra of Amorphous Silicon during the Insertion/Extraction of Lithium. J Phys Chem C 111:11437–11444. doi: 10.1021/jp0729563
64. Brinker CJ, Scherer GW (1990) Sol-Gel Science: The Physics and Chemistry of Sol-Gel Processing. Academic press
65. Brinker CJ (1988) Hydrolysis and condensation of silicates: effects on structure. J Non Cryst Solids 100:31–50.
66. Robert Lee G, Crayston JA (1994) Sol–gel processing of niobium chloroalkoxides. J Mater Chem 4:1093–1100.
67. Robert Lee G, Crayston JA (1991) Electrochromic Nb2O5 and Nb2O5/silicone composite thin films prepared by sol–gel processing. J Mater Chem 1:381–386.
68. Özer N, Chen D-G, Lampert CM (1996) Preparation and properties of spin-coated Nb2O5 films by the sol-gel process for electrochromic applications. Thin Solid Films 277:162–168. doi: 10.1016/0040-6090(95)08011-2
69. Avellaneda C, Schmitt M, Heusing S (2009) Electrochromic properties of Nb2O5 sol-gel coatings. Sol Energy Mater Sol Cells 54:9–17.
70. Aegerter M a., Schmitt M, Guo Y (2002) Sol-gel niobium pentoxide coatings: Applications to photovoltaic energy conversion and electrochromism. Int J Photoenergy 4:1–10. doi: 10.1155/S1110662X02000016
71. Aegerter M a. (2001) Sol–gel niobium pentoxide: A promising material for electrochromic coatings, batteries, nanocrystalline solar cells and catalysis. Sol Energy Mater Sol Cells 68:401–422. doi: 10.1016/S0927-0248(00)00372-X
72. Greener E, Whitmore D, Fine M (1961) Electrical Conductivity of Near- Stoichiometric α-NbO. J Chem Phys 25:2039–2041.

73. Klein N, Hollenstein E, Damjanovic D, et al. (2007) A study of the phase diagram of (K,Na,Li)NbO[sub 3] determined by dielectric and piezoelectric measurements, and Raman spectroscopy. J Appl Phys 102:014112. doi: 10.1063/1.2752799
74. Jasinski P, Petrovsky V, Dogan F (2010) Impedance spectroscopy of BaTiO[sub 3] cubes suspended in lossy liquids as a physical model of two-phase system. J Appl Phys 108:074111. doi: 10.1063/1.3486461
75. Wang C, Hong J (2007) Ionic/Electronic Conducting Characteristics of LiFePO[sub 4] Cathode Materials. Electrochem Solid-State Lett 10:A65–A69. doi: 10.1149/1.2409768
76. Clima S, Pourtois G, Hardy A, et al. (2010) Dielectric Response of Ta[sub 2]O[sub 5], Nb[sub 2]O[sub 5], and NbTaO[sub 5] from First-Principles Investigations. J Electrochem Soc 157:G20. doi: 10.1149/1.3253583
77. Dunn B, Long J, Rollison D (2008) Rethinking multifunction in three dimensions for miniaturizing electrical energy storage. Electrochem Soc Interface 49–53.
78. Pikul JH, Gang Zhang H, Cho J, et al. (2013) High-power lithium ion microbatteries from interdigitated three-dimensional bicontinuous nanoporous electrodes. Nat Commun 4:1732. doi: 10.1038/ncomms2747
79. Baggetto L, Niessen R a. H, Roozeboom F, Notten PHL (2008) High Energy Density All-Solid-State Batteries: A Challenging Concept Towards 3D Integration. Adv Funct Mater 18:1057–1066. doi: 10.1002/adfm.200701245
80. Wang C, Taherabadi L, Jia G, et al. (2004) C-MEMS for the Manufacture of 3D Microbatteries. Electrochem Solid-State Lett 7:A435. doi: 10.1149/1.1798151
81. Dudney N (2000) Addition of a thin-film inorganic solid electrolyte (Lipon) as a protective film in lithium batteries with a liquid electrolyte. J Power Sources 176–179.
82. Shin-ichi F, Satoshi S, Kaduhiro S, Hitoshi T (2004) Preparation and ionic conductivity of β-LiAlSiO4 thin film. Solid State Ionics 167:325–329. doi: 10.1016/j.ssi.2003.12.023
83. Baxamusa SH, Im SG, Gleason KK (2009) Initiated and oxidative chemical vapor deposition: a scalable method for conformal and functional polymer films on real substrates. Phys Chem Chem Phys 11:5227–40. doi: 10.1039/b900455f
84. Heil SBS, Langereis E, Kemmeren A, et al. (2005) Plasma-assisted atomic layer deposition of TiN monitored by in situ spectroscopic ellipsometry. J Vac Sci Technol A Vacuum, Surfaces, Film 23:L5–L8. doi: 10.1116/1.1938981
85. Leskelä M, Ritala M (2002) Atomic layer deposition (ALD): from precursors to thin film structures. Thin Solid Films 409:138–146. doi: 10.1016/S0040-6090(02)00117-7
86. Schulz H, Tscherry V (1972) Structural relations between the low- and high-temperature forms of β-eucryptite (LiAlSiO4) and low and high quartz. I. Low-temperature form of β-eucryptite and low quartz. Acta Crystallogr Sect B Struct Crystallogr Cryst Chem 28:2168–2173. doi: 10.1107/S0567740872005734
87. Thangadurai V, Weppner W (2002) Solid state lithium ion conductors: Design considerations by thermodynamic approach. Ionics (Kiel) 8:281–292. doi: 10.1007/BF02376081
88. Pryce Lewis HG, Bansal NP, White AJ, Handy ES (2009) HWCVD of polymers: Commercialization and scale-up. Thin Solid Films 517:3551–3554. doi: 10.1016/j.tsf.2009.01.114
89. Johansson A, Lauenstein A, Tegenfeldt J (1995) Effect of Water on Diffusion and Ionic Conductivity in PEG and LiCF3S03PEG10. J Phys Chem 99:6163–6166.

90. Bourgeois a., Brunet Bruneau A, Fisson S, et al. (2004) Determination of pore size distribution in thin organized mesoporous silica films by spectroscopic ellipsometry in the visible and infrared range. Thin Solid Films 447-448:46–50. doi: 10.1016/j.tsf.2003.09.020
91. Baklanov MR, Mogilnikov KP, Polovinkin VG, Dultsev FN (2000) Determination of pore size distribution in thin films by ellipsometric porosimetry. J Vac Sci Technol B Microelectron Nanom Struct 18:1385. doi: 10.1116/1.591390
92. Dull TL, Frieze WE, Gidley DW, et al. (2001) Determination of Pore Size in Mesoporous Thin Films from the Annihilation Lifetime of Positronium. J Phys Chem B 105:4657–4662. doi: 10.1021/jp004182v
93. Chailapakul O, Crooks RM (1995) Interactions between Organized, Surface-Confined Monolayers and Liquid-Phase Probe Molecules. 4. Synthesis and Characterization of Nanoporous Molecular Assemblies: Mechanism of Probe Penetration. Langmuir 11:1329–1340. doi: 10.1021/la00004a046
94. Bond A, McLennan E (1987) Assessment of conditions under which the oxidation of ferrocene can be used as a standard voltammetric reference process in aqueous media. Anal Chem 2860:2853–2860.
95. Wang Y, Rogers EI, Compton RG (2010) The measurement of the diffusion coefficients of ferrocene and ferrocenium and their temperature dependence in acetonitrile using double potential step microdisk electrode chronoamperometry. J Electroanal Chem 648:15–19. doi: 10.1016/j.jelechem.2010.07.006
96. McManis GE, Golovin MN, Weaver MJ (1986) Role of solvent reorganization dynamics in electron-transfer processes. Anomalous kinetic behavior in alcohol solvents. J Phys Chem 90:6563–6570. doi: 10.1021/j100282a029
97. Limon-Petersen JG, Dickinson EJF, Belding SR, et al. (2010) Cyclic voltammetry in weakly supported media: The reduction of the cobaltocenium cation in acetonitrile – Comparison between theory and experiment. J Electroanal Chem 650:135–142. doi: 10.1016/j.jelechem.2010.08.011
98. Cabrera CR, Bard AJ (1989) Electrochemistry in near-critical and supercritical fluids Part 8 . Methyl viologen , decamethylferrocene , Os (bpy) z ’ and ferrocene in acetonitrile and the effect of pressure on diffusion coefficients under supercritical conditions. J Electroanal Chem 273:147–160.
99. Forster R (1994) Microelectrodes: new dimensions in electrochemistry. Chem Soc Rev 23:289–297.
100. Nicholson R (1965) Theory and Application of Cyclic Voltammetry for Measurement of Electrode Reaction Kinetics. Anal Chem 37:1351–1355.
101. Tsierkezos NG, Ritter U (2009) Electrochemical impedance spectroscopy and cyclic voltammetry of ferrocene in acetonitrile/acetone system. J Appl Electrochem 40:409–417. doi: 10.1007/s10800-009-0011-3
102. Banica F (2000) A Simple Hanging Mercury Drop Electrode. J Chem Educ 77:98–100.
103. Ridgway P, Zheng H, Liu G, et al. (2008) Performance of Lithium Ion Cell Anode Graphites Under Various Cycling Conditions. ECS Trans 13:1–12.
104. Daschbach J, Blackwood D, Pons JW, Pons S (1987) EVIDENCE FOR IRREVERSIBLE KINETIC BEHAVIOR DUE TO PASSIVE FILM FORMATION. J Electroanal Chem 231:269–273.
105. Pyati R, Murray R (1996) Solvent dynamics effects on heterogeneous electron transfer rate constants of cobalt tris (bipyridine). J Am Chem Soc 1743–1749.

106. Janisch J, Ruff A, Speiser B, et al. (2011) Consistent diffusion coefficients of ferrocene in some non-aqueous solvents: electrochemical simultaneous determination together with electrode sizes and comparison to pulse-gradient spin-echo NMR results. J Solid State Electrochem 15:2083–2094. doi: 10.1007/s10008-011-1399-3
107. Lewandowski A, Waligora L, Galinski M (2013) Electrochemical Behavior of Cobaltocene in Ionic Liquids. J Solution Chem 42:251–262. doi: 10.1007/s10953-013-9957-1
108. Kojima H, Bard A (1975) Determination of rate constants for the electroreduction of aromatic compounds and their correlation with homogeneous electron transfer rates. J Am Chem Soc 97:6317–6324.
109. Dunn B, Kamath H, Tarascon J (2011) for the Grid : A Battery of Choices. Science (80-) 334:928–935.
110. Chu S, Majumdar A (2012) Opportunities and challenges for a sustainable energy future. Nature 488:294–303. doi: 10.1038/nature11475
111. (2013) International Energy Association. Renewable Energy Medium-Term Market Report.
112. Lewis NS, Nocera DG (2006) Powering the planet: chemical challenges in solar energy utilization. Proc Natl Acad Sci U S A 103:15729–35. doi: 10.1073/pnas.0603395103
113. Livage J, Henry M, Sanchez C (1988) Sol-gel chemistry of transition metal oxides. Prog Solid State Chem 18:259–341.
114. Hench LL, West JK (1990) The sol-gel process. Chem Rev 90:33–72. doi: 10.1021/cr00099a003
115. Miller OD, Yablonovitch E, Kurtz SR (2012) Strong Internal and External Luminescence as Solar Cells Approach the Shockley–Queisser Limit. IEEE J Photovoltaics 2:303–311. doi: 10.1109/JPHOTOV.2012.2198434
116. Cho T-Y, Ko K-W, Yoon S-G, et al. (2013) Efficiency enhancement of flexible dye-sensitized solar cell with sol–gel formed Nb2O5 blocking layer. Curr Appl Phys 2–7. doi: 10.1016/j.cap.2013.04.012
117. Aparicio M, Jitianu A, Klein LC (2012) Advances in Sol-Gel Derived Materials and Technologies. Springer
118. O'Regan B, Grätzel M (1991) A low-cost, high-efficiency solar cell based on dye-sensitized colloidal TiO2 films. Nature 353:737–740. doi: 10.1038/353737a0
119. Sauvage F, Chen D, Comte P, et al. (2010) Dye-sensitized solar cells employing a single film of mesoporous TiO2 beads achieve power conversion efficiencies over 10%. ACS Nano 4:4420–4425.
120. Stathatos E, Lianos P, Lavrencic-Stangar U, Orel B (2002) A High-Performance Solid-State Dye-Sensitized Photoelectrochemical Cell Employing a Nanocomposite Gel Electrolyte Made by the Sol–Gel Route. Adv Mater 14:354. doi: 10.1002/1521-4095(20020304)14:5<354::AID-ADMA354>3.0.CO;2-1
121. Li P, Wu J, Hao S, et al. (2010) Quasi-solid state dye sensitized solar cells based on the cross-linked poly (ethylene glycol) electrolyte with tetraethoxysilane. J Appl Polym Sci 1752–1757. doi: 10.1002/app
122. Wang P, Zakeeruddin SM, Comte P, et al. (2003) Gelation of ionic liquid-based electrolytes with silica nanoparticles for quasi-solid-state dye-sensitized solar cells. J Am Chem Soc 125:1166–7. doi: 10.1021/ja029294+
123. Stathatos E, Lianos P (2003) A quasi-solid-state dye-sensitized solar cell based on a sol-gel nanocomposite electrolyte containing ionic liquid. Chem Mater 102:1825–1829.

124. Kalowekamo J, Baker E (2009) Estimating the manufacturing cost of purely organic solar cells. Sol Energy 83:1224–1231. doi: 10.1016/j.solener.2009.02.003
125. Carrette L, Friedrich K a, Stimming U (2000) Fuel cells: principles, types, fuels, and applications. Chemphyschem 1:162–93. doi: 10.1002/1439-7641(20001215)1:4<162::AID-CPHC162>3.0.CO;2-Z
126. Osman MH, Shah a a, Walsh FC (2011) Recent progress and continuing challenges in bio-fuel cells. Part I: enzymatic cells. Biosens Bioelectron 26:3087–102. doi: 10.1016/j.bios.2011.01.004
127. Kreuer KD (2001) On the development of proton conducting polymer membranes for hydrogen and methanol fuel cells. J Memb Sci 185:29–39. doi: 10.1016/S0376-7388(00)00632-3
128. Skyllas-Kazacos M, Chakrabarti MH, Hajimolana S a., et al. (2011) Progress in Flow Battery Research and Development. J Electrochem Soc 158:R55–R79. doi: 10.1149/1.3599565
129. Tripathi BP, Shahi VK (2011) Organic–inorganic nanocomposite polymer electrolyte membranes for fuel cell applications. Prog Polym Sci 36:945–979. doi: 10.1016/j.progpolymsci.2010.12.005
130. Osman MH, Shah a a, Walsh FC (2010) Recent progress and continuing challenges in bio-fuel cells. Part II: Microbial. Biosens Bioelectron 26:953–63. doi: 10.1016/j.bios.2010.08.057
131. Lim J, Malati P, Bonet F, Dunn B (2007) Nanostructured Sol-Gel Electrodes for Biofuel Cells. J Electrochem Soc 154:A140–A145. doi: 10.1149/1.2404904
132. Willner I, Katz E (2000) Integration of layered redox proteins and conductive supports for bioelectronic applications. Angew Chemie Int Ed 39:1180–1218.
133. Urbanová V, Etienne M, Walcarius A (2013) One Step Deposition of Sol-Gel Carbon Nanotubes Biocomposite for Reagentless Electrochemical Devices. Electroanalysis 25:85–93. doi: 10.1002/elan.201200407
134. Wang Z, Etienne M, Kohring G-W, et al. (2011) Electrochemically assisted deposition of sol–gel bio-composite with co-immobilized dehydrogenase and diaphorase. Electrochim Acta 56:9032–9040. doi: 10.1016/j.electacta.2011.05.130
135. Deng L, Shang L, Wen D, et al. (2010) A membraneless biofuel cell powered by ethanol and alcoholic beverage. Biosens Bioelectron 26:70–3. doi: 10.1016/j.bios.2010.05.007
136. Strack G, Luckarift HR, Sizemore SR, et al. (2013) Power generation from a hybrid biological fuel cell in seawater. Bioresour Technol 128:222–8. doi: 10.1016/j.biortech.2012.10.104
137. Szot K, Lesniewski A, Niedziolka J, et al. (2008) Sol–gel processed ionic liquid – hydrophilic carbon nanoparticles multilayer film electrode prepared by layer-by-layer method. J Electroanal Chem 623:170–176. doi: 10.1016/j.jelechem.2008.07.023
138. Niedziolka-Jonsson J, Jonsson-Niedziolka M, Nogala W, Palys B (2011) Electrosynthesis of thin sol–gel films at a three-phase junction. Electrochim Acta 56:3311–3316. doi: 10.1016/j.electacta.2011.01.024
139. Ladewig BP, Knott RB, Hill AJ, et al. (2007) Physical and Electrochemical Characterization of Nanocomposite Membranes of Nafion and Functionalized Silicon Oxide. Chem Mater 19:2372–2381. doi: 10.1021/cm0628698

140. Mauritz K, Warren R (1989) Microstructural evolution of a silicon oxide phase in a perfluorosulfonic acid ionomer by an in situ sol-gel reaction. 1. Infrared spectroscopic studies. Macromolecules 1734:1730–1734.
141. Di Vona M, Ahmed Z, Bellitto S, et al. (2007) SPEEK-TiO2 nanocomposite hybrid proton conductive membranes via in situ mixed sol–gel process. J Memb Sci 296:156–161. doi: 10.1016/j.memsci.2007.03.037
142. Tsai J-C, Kuo J-F, Chen C-Y (2007) Synthesis and properties of novel HMS-based sulfonated poly(arylene ether sulfone)/silica nano-composite membranes for DMFC applications. J Power Sources 174:103–113. doi: 10.1016/j.jpowsour.2007.08.086
143. Krishnan P, Park J-S, Kim C-S (2006) Preparation of proton-conducting sulfonated poly(ether ether ketone)/boron phosphate composite membranes by an in situ sol–gel process. J Memb Sci 279:220–229. doi: 10.1016/j.memsci.2005.12.010
144. Wen S, Gong C, Tsen W-C, et al. (2009) Sulfonated poly(ether sulfone) (SPES)/boron phosphate (BPO4) composite membranes for high-temperature proton-exchange membrane fuel cells. Int J Hydrogen Energy 34:8982–8991. doi: 10.1016/j.ijhydene.2009.08.074
145. Li Q, Jensen JO, Savinell RF, Bjerrum NJ (2009) High temperature proton exchange membranes based on polybenzimidazoles for fuel cells. Prog Polym Sci 34:449–477. doi: 10.1016/j.progpolymsci.2008.12.003
146. Bagotsky VS (2012) Phosphoric acid fuel cells 5.1. Fuel Cells Probl. Solut. pp 99–106
147. Xiao L, Zhang H, Scanlon E (2005) High-temperature polybenzimidazole fuel cell membranes via a sol-gel process. Chem Mater 16:5328–5333.
148. Mader J a., Benicewicz BC (2010) Sulfonated Polybenzimidazoles for High Temperature PEM Fuel Cells. Macromolecules 43:6706–6715. doi: 10.1021/ma1009098
149. Oriji G, Katayama Y, Miura T (2004) Investigation on V(IV)/V(V) species in a vanadium redox flow battery. Electrochim Acta 49:3091–3095. doi: 10.1016/j.electacta.2004.02.020
150. Xi J, Wu Z, Qiu X, Chen L (2007) Nafion/SiO2 hybrid membrane for vanadium redox flow battery. J Power Sources 166:531–536. doi: 10.1016/j.jpowsour.2007.01.069
151. Teng X, Zhao Y, Xi J, et al. (2009) Nafion/organic silica modified TiO2 composite membrane for vanadium redox flow battery via in situ sol–gel reactions. J Memb Sci 341:149–154. doi: 10.1016/j.memsci.2009.05.051
152. Schulte D, Drillkens J, Schulte B, Sauer DU (2010) Nafion Hybrid Membranes for Use in Redox Flow Batteries. J Electrochem Soc 157:A989–A992. doi: 10.1149/1.3456625
153. Teng X, Lei J, Gu X, et al. (2012) Nafion-sulfonated organosilica composite membrane for all vanadium redox flow battery. Ionics (Kiel) 18:513–521. doi: 10.1007/s11581-012-0694-z
154. Goodenough JB, Kim Y (2010) Challenges for Rechargeable Li Batteries. Chem Mater 22:587–603. doi: 10.1021/cm901452z
155. Liu H, Wu YP, Rahm E, et al. (2004) Cathode materials for lithium ion batteries prepared by sol-gel methods. J Solid State Electrochem 8:450–466. doi: 10.1007/s10008-004-0521-1
156. Fu L, Liu H, Li C, et al. (2005) Electrode materials for lithium secondary batteries prepared by sol–gel methods. Prog Mater Sci 50:881–928. doi: 10.1016/j.pmatsci.2005.04.002
157. Vioux A, Viau L, Volland S, Le Bideau J (2010) Use of ionic liquids in sol-gel; ionogels and applications. Comptes Rendus Chim 13:242–255. doi: 10.1016/j.crci.2009.07.002
158. Le Bideau J, Viau L, Vioux A (2011) Ionogels, ionic liquid based hybrid materials. Chem Soc Rev 40:907–25. doi: 10.1039/c0cs00059k

159. Kurig H, Romann T, Jänes A, Lust E (2010) Electrochemical characteristics of titanium carbide derived carbon| 1-ethyl-3-methylimidazolium tetrafluoroborate electrical double layer capacitors. ECS Trans 25:15–23.
160. Echelmeyer T, Meyer H, Wüllen L van (2009) Novel ternary composite electrolytes: Li ion conducting ionic liquids in silica glass. Chem Mater 2280–2285.
161. Lewandowski A, Świderska-Mocek A (2009) Ionic liquids as electrolytes for Li-ion batteries—an overview of electrochemical studies. J Power Sources 194:601–609. doi: 10.1016/j.jpowsour.2009.06.089
162. Zhang J, Ma Y, Shi F, et al. (2009) Microporous and Mesoporous Materials Room temperature ionic liquids as templates in the synthesis of mesoporous silica via a sol – gel method. Microporous Mesoporous Mater 119:97–103. doi: 10.1016/j.micromeso.2008.10.003
163. Bellayer S, Viau L, Tebby Z, et al. (2009) Immobilization of ionic liquids in translucent tin dioxide monoliths by sol–gel processing. Dalt Trans 1307. doi: 10.1039/b814978j
164. Davenport M, Rodriguez A, Shea K, Siwy Z (2009) Squeezing ionic liquids through nanopores. Nano Lett 9:2125–2128.
165. Le Bideau J, Ducros J-B, Soudan P, Guyomard D (2011) Solid-State Electrode Materials with Ionic-Liquid Properties for Energy Storage: the Lithium Solid-State Ionic-Liquid Concept. Adv Funct Mater 21:4073–4078. doi: 10.1002/adfm.201100774
166. Lin R, Huang P, Ségalini J, et al. (2009) Solvent effect on the ion adsorption from ionic liquid electrolyte into sub-nanometer carbon pores. Electrochim Acta 54:7025–7032. doi: 10.1016/j.electacta.2009.07.015
167. Karout a, Pierre a (2009) Silica gelation catalysis by ionic liquids. Catal Commun 10:359–361. doi: 10.1016/j.catcom.2008.07.046
168. Soleimani Dorcheh a., Abbasi MH (2008) Silica aerogel; synthesis, properties and characterization. J Mater Process Technol 199:10–26. doi: 10.1016/j.jmatprotec.2007.10.060